PIEZOELECTRIC ACOUSTIC SENSORS AND ULTRASONIC TRANSDUCERS BASED ON TEXTURED PZT THIN FILMS

THÈSE N° 2699 (2002)

PRÉSENTÉE À LA FACULTÉ DES SCIENCES ET TECHNIQUES DE L'INGÉNIEUR

SECTION DES MATÉRIAUX

ÉCOLE POLYTECHNIQUE FÉDÉRALE DE LAUSANNE

POUR L'OBTENTION DU GRADE DE DOCTEUR ÈS SCIENCES TECHNIQUES

PAR

Nicolas G. LEDERMANN

ingénieur en science des matériaux diplômé EPF
de nationalité suisse et originaire de Lauperswil (BE)

acceptée sur proposition du jury:

Prof. N. Setter, directrice de thèse
Prof. H. Bleuler, rapporteur
Prof. P. Gaucher, rapporteur
Dr F. Gueissaz, rapporteur
Dr P. Muralt, rapporteur

Lausanne, EPFL
2003

CHAPTER 1

INTRODUCTION

1.1 THE FASCINATING WORLD OF MICROSYSTEMS

Micro-electro-mechanical systems (MEMS), or microsystems constitute a fascinating world of miniaturized devices that are just beginning to affect many areas of our life [1], [2]. The idea behind MEMS is not new. MEMS were foreseen by the legendary physicist Richard Feynman, who theorized in 1959 during a talk to the American physical society titled "There is plenty of room at the bottom", the emergence of micromachines now being developed [3]. But it took more than 30 years - and the development of silicon micromachining - for MEMS physics to catch up Feynman's thinking.

While the original notion of MEMS emphasizes that mechanical elements are added to microelectronics - as needed for motion sensors for instance - the actual field has a much broader content today and includes also optical, thermal, magnetic, and fluidic (chemical and biological) interactions and phenomena leading to numerous applications in the automotive industry, aeronautics, cellular communication, bio-chemistry, genetics, acoustics, display technologies as well as other photonics systems [4], [5].

In mainstream MEMS technology, silicon is used as supporting and structural material for the devices. Silicon is cheap, has excellent elastic properties, a low thermal expansion coefficient, and does not creep and age because it is a pure, monocrystalline material. In addition, silicon dry etching processes are available for accurate anisotropic microstructuration. To a certain extent, one can fabricate devices by means of an "all-silicon" technology based on electrostatic interaction between doped silicon elements [6], [7]. In general, however, many more materials properties are needed than silicon can offer. Silicon is a bad electrical and a very good thermal conductor, for instance. Hence, one has to add metal films for improving electrical conduction or films such as SiO_2 or Si_3N_4 for improving thermal insulation. Such films are today easily available thanks to the large-scale semiconductor fabrication.

MEMS can make use of a lot of other characteristics displayed by thin films to fulfill different sensing or actuating functions. For that reason, new functional materials play a key role in MEMS technology. They provide a direct transformation between driving signal or read-out signal on the one hand, and sensor or actuator parameters on the other hand. While the driving or the read-out signal is either electrical, magnetic, or optical, the sensor parameter can be a mechanical deformation, a temperature change or a chemical reaction, etc. Actuation can mean a linear displacement, the emission of an ultrasonic wave, the phase shift of a laser light beam for instance. In that perspective, piezoelectrics are an important family of functional materials in MEMS technology. They provide directly the electro-mechanical coupling as stipulated in the original sense of MEMS notion. The use of piezoelectrics is in competition with electrostatic, thermal and magnetic actuation principles. The main advantages of piezoelectricity principle lie in immediate response (sensor and actuator), large available forces (100 MPa), low noise, wide frequency range of operation (mHz to GHz) and simplicity of the transduction mechanism which is planar [8].

1.2 THE PIEZOELECTRICITY

1.2.1 Fundamentals

Pierre Curie and his brother Jacques discovered in 1880 that an external force applied on certain crystal generates an electrical charge which was found to be proportional to the applied mechanical stress. The original description was as follow: *"Quelle que soit la cause déterminante, toutes les fois qu'un cristal hémièdre à faces inclinées, non conducteur, se contracte, il y a formation de pôles électriques dans un certain sens; toutes les fois que ce cristal se dilate, le dégagement d'électricité a lieu en sens contraire"*. This phenomenon was called "direct" piezoelectricity [9]. One year later, they found the converse piezoelectric effect, meaning that an applied voltage generated a deformation of the crystal [10].

As shown by the Curie's brothers, the piezoelectricity is an electromechanical coupling that finds its origin in the non-centrosymmetry of the crystal structure [11]. In these crystals, an applied stress or an applied electric field gives rise to an asymmetrical ionic displacement (change of the dipole moment) which cause electrical charges or lattice deformation respectively. Every crystal belonging to non-centrosymmetric point groups (20 groups of 32) is thus piezoelectric with the exception of the cubic group 432 where particular symmetry characteristics prevent it.

Of these 20 groups, 10 are said polar and exhibit an internal polarization. Its temperature dependence is called pyroelectricity and can be exploited for thermal sensors. If the internal polarization can be reversed by mean of an external electrical field, the material is defined as a ferroelectric. In such materials, polarization forms spontaneously below a certain critical temperature, called the Curie temperature. In bulk ceramics, this internal polarization is randomly oriented. In bulk ceramics like PZT or in as-deposited thin films, this internal polarization is randomly or slightly oriented respectively. To exhibit a net piezoelectric activity, the domains have to be aligned close to one direction by applying an electrical field on the material. This process is called poling. In non-ferroelectric materials like AlN or ZnO, the orientation of the internal polarization has to be obtained by the deposition process itself as no re-orientation is possble. Ferroelectric materials is thus always piezoelectric and pyroelectric but the reciprocal relation is not always true.

The direct piezoelectric effect is defined as the linear relation between the mechanical stress σ_l (N/m^2) applied on a piezoelectric material and the resulting density of charge D_i. On the opposite, the inverse piezoelectric effect express the linear relation between the elastic deformation S_k generated by an applied electric field E_i. Both direct and inverse effect may be represented by the following relations:

$$D_i = d_{ik}\sigma_k + \varepsilon_0\varepsilon_{ij}^{T}E_j \tag{1.1}$$

$$S_k = s_{kl}^{E}\sigma_l + d_{ik}E_i \tag{1.2}$$

where the matrix indexation is used: kl = 1..6 and ij = 1..3. d_{ik} can be expressed either in (C/N) or (m/V) and represents the piezoelectric coefficient. s_{kl}^{E} (m^2/N) is the elastic compliance of the material and ε_{ij}^{T} the dielectric permittivity tensor.

The complex dielectric permittivity tensor is given by equation 1.3:

$$\varepsilon = \varepsilon' - i\varepsilon'' \qquad \tan\delta = \frac{\varepsilon''}{\varepsilon'} \tag{1.3}$$

where tan δ is the dielectric loss factor, which represents power dissipation in ac applications:

$$P = \omega C \cdot \tan\delta \cdot U_{eff}^{2} \tag{1.4}$$

were C is the device capacitance, ω the excitation frequency and U_{eff} the driving voltage.

The piezoelectric materials are thus very useful since they can be used for actuation or/and for sensing. For example, the combination of the two effects is the heart of all ultrasonic transducers for medical imaging. Piezoelectric actuation or sensing offers key advantages in devices requiring large output forces and power, low noise or high frequency operation (in the GHz range).

1.2.2 Effective piezoelectric and dielectric properties in thin films

The most important properties to investigate in piezoelectric materials are the longitudinal d_{33} and transverse e_{31} piezoelectric coefficients. d_{33} describes the change of material thickness or strain S_3 which develops along the vertical 3-axis due to the application of an electric field E_3 in the same direction. d_{33} is very useful to describe most of the devices fabricated from bulk piezoelectric ceramics such as medical ultrasonic transducers or piezoelectric thin film resonators and RF filters. However, the coefficient d_{33} is not very often used in piezoelectric MEMS as they are usually based on deflecting structures such as cantilevers or membranes (see Figure 1.1). The relevant piezoelectric constant is thus the transverse coefficients e_{31} or d_{31} that describe the bending of the structure (generated by a piezoelectric stress) along the 1-axis as a function of a transverse electrical field E_3 or the transverse charges (along 3-axis) generated by the bending of the piezoelectric material (elastic strain along the 1-axis).

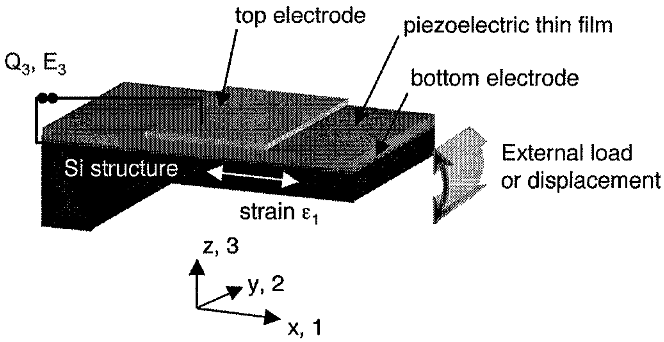

Figure 1.1: Transverse piezoelectric effect on a piezoelectric / silicon heteromorph deflecting structure.

However, the piezoelectric properties in piezoelectric thin films cannot be directly compared with the ones (d_{33}, e_{31}) of corresponding bulk materials. As the film is clamped on the substrate, it cannot move in the in-plane directions (x, y) but is free to expand in the off-plane direction (z). The piezoelectric properties exhibited in piezoelectric thin films are thus modified by these boundary conditions and new effective coefficients have to be introduced. Those coefficients are the longitudinal $d_{33,f}$ and transverse $e_{31,f}$ where the f subscript denotes effective values of a thin film.

For a perfect clamping, S_1 and S_2 are equal to zero and S_3 is different of zero. For the same reason, the in-plane stress σ_1 and σ_2 are equal and σ_3 is zero. Starting from the constitutive equations and introducing the particular boundary conditions of perfect clamping, effective values $d_{33,f}$ and $e_{31,f}$ can be calculated [12], [13]:

$$e_{31,f} = \frac{d_{31,f}}{s_{11}^{E} + s_{12}^{E}} = e_{31} - \frac{c_{13}^{E}}{c_{33}^{E}} \cdot e_{33} \qquad |e_{31,f}| > |e_{31}| \tag{1.5}$$

$$d_{33,f} = d_{33} - \frac{2s_{13}^{E}}{s_{11}^{E} + s_{12}^{E}} d_{31} = d_{33} - 2s_{13}^{E} \cdot e_{31,f} \qquad < d_{33} \tag{1.6}$$

$$\varepsilon_{33,f} = \varepsilon_{33}^{T} - \frac{2 \cdot d_{31}^{2}}{\left(s_{11}^{E} + s_{12}^{E}\right) \cdot \varepsilon_0} \tag{1.7}$$

The effect of the clamping is thus to reduce the bulk d_{33} and ε_{33} coefficients and to increase the magnitude of the e_{31} transverse effect.

1.3 PIEZOELECTRIC MATERIALS FOR MICROSYSTEMS APPLICATIONS

Piezoelectric monocrystals and bulk ceramics have been widely used for decades in many macroscopic applications. For example, quartz crystals and $LiNbO_3$ monocrystal substrates are used in time and frequency control devices (resonators, surface acoustic wave (SAW) devices, RF filters). Apart quartz, $Pb(Zr, Ti)O_3$ bulk ceramic can be considered as the most popular piezoelectric material and has been successfully applied in many devices such as underwater sonar or ultrasonic probes for medical imaging (PZT rods dispersed in a polymer matrix).

In microsystems (MEMS), piezoelectric materials have to be deposited in the form of thin (< 5 µm) films. Beside integration issues, a particular attention should be paid to select the right material with respect to the targeted application. For instance, AlN films have been often used in RF filters, ZnO films in acoustic sensors and accelerometers and PZT films for ultrasonic transducers and AFM tips. To help in this choice, the appendix A and the following sections summarize the mechanical and functional properties as well as the figures of merit (FOM) corresponding to different applications (sensors, actuators or transducers).

1.3.1 Aluminium nitride, AlN

Aluminium nitride (AlN) is a non-ferroelectric piezoelectric material that crystallizes into the wurtzite structure (see Figure 1.2). The unit cell (a = 3.1117 Å, c = 4.9792 Å) consists of two interpenetrating hexagonal close-packed lattices: one is occupied by aluminium and the second by nitrogen atoms. Each atom has a coordination number of 4 and is equidistant to his neighbors placed in a tetrahedron.

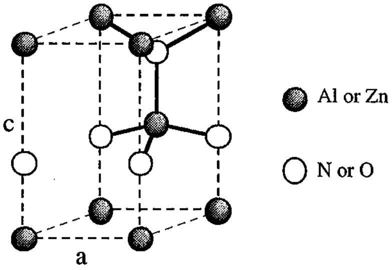

Figure 1.2: AlN or ZnO unit cell (wurtzize)

As the aluminium nitride is non-ferroelectric, its internal polarization (along the c-axis) cannot be reoriented by any external force. AlN material with randomly grain structure like in bulk ceramics is not piezoelectric or pyroelectric as no net polarization direction appear and no polarization process is possible. The piezoelectric effect can be found only in single crystals or in textured thin films.

One of the most interesting feature of piezoelectric AlN thin films lies in the fact that its properties are very stable with respect to the frequency and the applied electrical field. Its low dielectric constant ($\varepsilon_{33} = 10$) and loss ($\tan \delta < 0.002$) are very interesting for low power consumption ultrasonic applications. AlN is also one of the stiffer materials in nature. It enables large elastic wave velocity, which is a decisive advantage for high frequency acoustic wave devices.

The piezoelectric coefficients of AlN are rather weak, about 10 times lower compared to PZT thin films of comparable thickness. But its low dielectric permittivity compensates the low piezoelectric constants to give high signal-to-noise (S/N) ratio. AlN can be an excellent piezoelectric material for sensor applications in voltage detection mode. As the emitted power is proportional to the square of the piezoelectric coefficient, the output power is however too weak for certain applications that require high power and high forces such as ultrasonic transducers for medical imaging.

Finally, due to its chemical inertness up to 2500°C, AlN is a promising material when integration issues are considered and is fully compatible with the silicon technology encountered in IC fabs.

1.3.2 Zinc oxide, ZnO

Zinc oxide (ZnO) is a well-known extrinsic n-type semiconductor (3.3 eV band gap) with the same wurtzite crystalline structure than AlN (see Figure 1.2). Like AlN, it consists in two interpenetrating hexagonal close-packed lattices of Zn and O atoms where each atom lies inside a tetrahedron formed by 4 atoms of the other species. The dimensions of the unit cell are a = 3.2498 Å and c = 5.2066 Å and the polar axis is the c-axis. Like AlN, it is only polar and not ferroelectric. The alignment of the polar axis cannot be effectuated by an external field and must be provided by the process growth. As a semiconductor, the conductivity and the dielectric properties of ZnO are very much dependant of the doping level and can cover up to 17 orders of magnitude (10^{-4} to 10^{12} Ωcm) [14]. Moreover, due to its band gap of 3.3 eV, ZnO is UV photoconductive. In its bulk ceramics form, ZnO is widely used in varistors for surge protection against voltage transients and power overloads in electronics.

In the field of microsystems (MEMS) and thin films, the main applications of piezoelectric ZnO thin films are in surface acoustic wave (SAW) devices where its high stiffness is of decisive importance. It has been also applied in many electro-mechanical devices, including accelerometers and acoustic sensors. But its properties are very sensitive to the deposition method as doping by unintended (intrinsic) defects such as interstitial sites may lead to leakage problems. For that reason, it is also difficult to find in the literature reliable and representative data on piezoelectric properties of ZnO thin films.

In sensors, the low piezoelectric constant can be partially compensated through voltage detection thanks to a low dielectric permittivity. But in transducers where force is required, ZnO tends to be replaced by $Pb(Zr, Ti)O_3$ (PZT) thin films as its transverse piezoelectric coefficient is about 10 times lower.

Finally, ZnO is also fully compatible with the standard CMOS technology.

1.3.3 Lead zirconate titanate solid solution, PZT

One of the most widely used piezoelectric material, at least in its bulk ceramic form, is the ferroelectric $Pb(Zr_xTi_{1-x})O_3$ solid solution (PZT). PZT crystallizes into the perovskite structure. Lead and oxygen make up a face-centered cubic array where Pb^{2+} cations are located on the corners. Ti^{4+} or Zr^{4+} ions are located at the center of the unit cell on a octahedral site. Above the Curie temperature, the structure is cubic and paraelectric. Below, it is either rhombohedral or tetragonal for Zr-rich or Ti-rich composition respectively. These two phases are separated by the so-called morphotropic phase boundary (MPB) which, at room temperature, is situated at Zr/Ti = 53/47. Figure 1.3 shows the phase diagram of $Pb(Zr_xTi_{1-x})O_3$ solid solution as well as the corresponding perovskite unit cells [15].

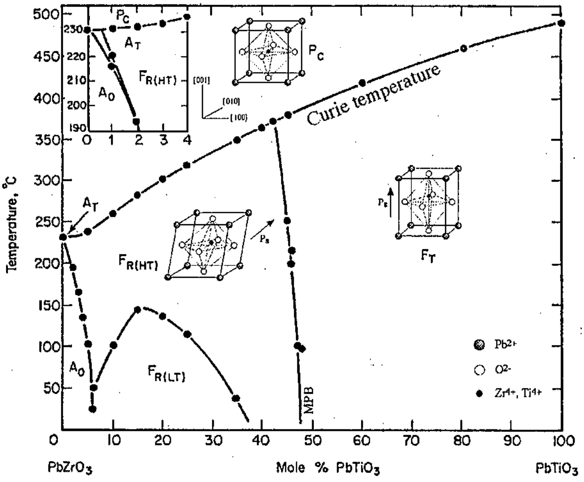

Figure 1.3: $PbTiO_3$ - $PbZrO_3$ phase diagram [15]

For tetragonal compositions (Ti-rich), the distortion and the internal polarization occur along the (001) c-axis (there are 6 equivalent directions of polarization). In rhombohedral compositions (Zr-rich), the distortion and the polarization develop along the (111) axis and they are 8 equivalent directions of polarization. The best composition in term of polarization orientation and thus in piezoelectric properties lies around the MPB. At 53% Zr, both tetragonal and rhombohedral phases coexist since they have an equal probability to form. The number of polarization directions is thus 6 + 8 = 14, leading to a peak in the dielectric and piezoelectric properties.

Upon cooling through the paraelectric-ferroelectric phase transition, a spontaneous polarization as well as an internal strain are created in the material. To minimize both elastic and electrostatic energies, the material split into regions where the direction of polarization is unique. These regions are called ferroelectric domains. In tetragonal phase (Ti-rich), the possible angle between the polarization orientations of two adjacent domains can be 90° or 180° and for the rhombohedral one (Zr-rich), 71°, 109° and 180°. At the MPB, all these domains can exist and no net polarization appears. To exhibit a global piezoelectric response, PZT materials need to be poled. During this process, the polar axis of the domains are oriented nearest the direction of the poling field giving rise to a net polarization and thus non-zero piezoelectric effect.

1.3.4 Comparison of piezoelectric properties and Figures of Merit

To compare efficiently the properties of piezoelectric materials with respect to potential applications, Figures of Merit (FOM) have been calculated. The FOM definitions and the fundamental properties of piezoelectric thin films used for the calculations are presented in Appendix A. Table 1.1 summarizes the FOM for PZT, AlN, ZnO thin films, ZnO single crystal, AlN epitaxial film and PZT bulk ceramics.

Table 1.1: Figures of merits (FOM) of piezoelectric thin films, ceramics and single crystals.

Figures of Merits transverse effect	**(111) PZT 45/55 film, 1 µm [16]**	AlN film [16]	ZnO film [17]	bulk PZT Motorola 3203HD [18]	bulk undoped PZT52/48 [19]	AlN epitaxial film [20]	s.c. ZnO [21]
Force and curent resp. (C/m^2), = $-e_{31,f}$	**-8.28**	**-1.02**	**-0.83**	**-25.9**	**-9.6**	**-1.05**	**-1.23**
Voltage resp. (GV/m)	**-0.85**	**-10.9**	**-8.3**	**-1.82**	**-2.06**	**-12.96**	**-12.5**
Signal to Noise (10^5 Pa$^{0.5}$)	**4.8**	**23.7**	**2.5 - 8**	**3.86**	**8.04**		
Coupling coeff. k^2 (-)	**0.08**	**0.12**	**0.023**	**0.52**	**0.22**	**0.15**	**0.17**
Power efficiency (-)	**2.61**	**62**	**0.23 - 2.3**	**18.7**	**81.25**		

It shows that the piezoelectric constant of PZT thin films are more than 10 times higher than in aluminium nitride or zinc oxide. In sensors, this enables higher signals if the charges are directly measured (Force and current response FOM). In actuators, it enables more force (stress up to 100 MPa, strains of up to 0.1 %, [22]) and much more output power (proportional to the square of the piezoelectric coefficient). PZT is thus the material of choice for sensors if the charges are detected and for actuators that requires high output power like ultrasonic transducers for medical applications. Compared to AlN films, the power efficiency of PZT is about 11.5 times lower and is thus, not the best material for low consumption and high frequency devices in the GHz range.

1.4 DEPOSITION AND INTEGRATION OF PZT THIN FILMS ON SILICON

The growing interest in the field of microsystems for "smart" or functional materials with outstanding actuation and/or sensing capabilities has driven the integration of new piezoelectric materials on silicon. It has been demonstrated previously that PZT was one of the most promising material for microsystems applications as its high piezoelectric coefficients yield high sensor sensitivity (current detection mode) and more available forces in actuators or transducers applications.

The integration of PZT thin films on silicon is, unfortunately, not a trivial task. Due to crystallization temperatures ranging from 500 to 700 °C in oxygen, it is well known that the diffusion and the evaporation of the lead atoms has to be compensated by incorporating a lead excess in the deposition process. Then, the deposition and the stability of the bottom electrode (including its adhesion layer and a diffusion barrier) are also important issues. Finally, the choice of the seeding layer and the kinetics of growth are critical to obtain the desired crystallization orientation. Once these integration questions have been solved, PZT thin films offer interesting potentials in the microfabrication of high performance piezoelectric microsystems.

1.4.1 Depositions methods of PZT thin films

The first methods used to growth PZT films were physical and based on electron beam evaporation [23], ion-beam deposition [24], or radio-frequency sputtering [25]. In the latter method, the process use simultaneously metallic sources of zirconium, titanium and lead in an oxidizing atmosphere. The erosion of the targets is performed in dc mode for Zr, Ti and in RF mode for Pb. Tuning the source flux controls the composition, which can be modified during the deposition. Due to the plasma discharge, the sputtering process lowers the deposition temperature and may favor the in-situ polarization of the film [26], [27]. Pulsed laser deposition (PLD) techniques [28] have been also explored for fundamental studies but no perspectives in industrial process have been though as the deposited area is very limited.

Whereas before 1990 mostly physical deposition techniques were applied, the chemical methods are now becoming more and more important. These methods involve chemical reactions of precursors (liquid or in a vapor phase) at elevated temperature. The crystallization occurring directly on the substrate. Metal-organic chemical vapor deposition (MOCVD) [29], [30], [31], [32] is a very versatile method as it allows an excellent film uniformity and conformality (step coverage), an accurate compositional control, a high deposition rate as well as large wafer-size up-scaling capability. The precursors are sprayed in gaseous phase in an oxygen atmosphere and the reaction products crystallize in-situ on the substrate [33]. However, this method still suffers from the difficulty to find high purity precursors and from the heavy equipment infrastructure and cost.

Today, the chemical solution deposition (CSD) of PZT thin films seems to meet the integration requirements of the standard silicon wafer technology encountered in microsystems fabs. Chemical solution deposition (CSD) is based on multiple spin-coating of the wafer with a liquid precursor. After removing the solvent through a pyrolysis process at about 350°C, the film is crystallized during a final rapid thermal annealing (RTA) in oxygen, usually at 650°C. The major advantages of this method over vacuum deposition processes lie in a better control of the material composition in multicomponent systems, the ability to produce uniform large area coating and the relative low level of investments required for the equipments.

1.4.2 The sol-gel process

The different solution methods to prepare multi components metal oxides [34] such as Pb(Zr, Ti)O_3 thin films are based on metal-organic precursors. The sol-gel process [35], [36] use alkoxides ($M(OR)_n$), where M represents the metallic cation and R is an alkyl group. This process can be broadly defined as the chemical elaboration of ceramic materials by the synthesis of a precursor solution, the spin-coating and the gelation of the sol, the drying and pyrolysis of the gel and a final crystallization at high temperature.

The reaction starts through the hydrolysis of the alkoxy group (OR).

Hydrolysis: M-OR + H_2O -> M-OH + ROH

When the hydroxy groups (M-OH) are formed, poly condensation reactions take place. Two reactions are competing: a) oxolation, formation of M-O-M and b) olation, formation of M-OH-M

a) oxolation: M-OH + M-OH -> M-O-M + H_2O
M-OH + M-OR -> M-O-M + ROH
b) olation: M-OH + M-OH -> M-OH-M + H_2O
M-OH + M-OR -> M-OH-M + ROH

The first reports of sol-gel deposition of $PbTiO_3$ and $Pb(Zr, Ti)O_3$ thin films were due to Gurkovich (1984) [37] and Budd (1985) [38] respectively. For PZT films, Budd used lead trihydrate, titanium isopropoxide, zirconium n-propoxide and 2-methoxyethanol as solvent. Driven by the potential applications of PZT thin films in devices, subsequent reports on the optimization of the solution precursors have been published, mainly by Schwartz at Sandia National Laboratories, USA [39], [40], [41], [42].

The preparation of reproducible high quality PZT films with best electromechanical properties using the sol-gel technique requires a controlled conversion of the as-deposited amorphous structure into the perovskite crystalline phase. Three distinctive steps have to be taken into account: the spin-coating of the solution precursor, the drying / pyrolysis of the gel and the crystallization kinetics of the film.

The spin-coating speed (and the viscosity of the precursor) mainly governs the thickness of the deposited layer. Typical values are in the range of 50-70 nm for a solution precursor of 0.4 M [43]. About 16 individual layers are thus required to form 1 µm PZT film.

During the drying and pyrolysis process, the solvent is removed from the gel to give an amorphous and porous inorganic metal oxide layer. The film thickness and the heating rate have a critical influence on the shrinkage i.e. on the cracking resistance of the film [44], [43]. Brooks demonstrated also in 1994 that the pyrolysis temperature has a strong influence on the film texture and microstructure [45]. After several individual layer deposition and pyrolysis, the film crystallization is achieved by a thermal annealing at 500°C - 700°C. In the range of 350°C to 500 °C, the amorphous phase transforms into an oxygen deficient pyrochlore structure $Pb_2(Zr, Ti)_2O_{7-x}$. Above 700°C or after a long heat treatment, a new lead deficient phase $Pb(Zr, Ti)_3O_7$ forms at the surface of the film due to the volatilization of PbO [46], [47], [48], [43].

The crystallization of pure perovskite PZT phase depends strongly on many parameters such as the pyrolysis conditions, the lead excess introduced in the PZT precursors, the solution chemistry, the annealing atmosphere and the substrate-electrode structure. The integration of PZT on platinized silicon substrates imposes a low thermal budget for all steps involved in the crystallization of the films. This requirement can be achieved by rapid thermal treatment with increased temperatures. Rapid thermal annealing (RTA) technique allows very fast heating rates (up to several thousands °C/s) and the minimization of the crystallization of undesirable metastable pyrochlore phase, as well as the reduction of the bottom electrode degradation.

1.4.3 Growth issues: bottom electrodes and seeding layers

In sensors and actuators, PZT piezoelectric thin films are grown on a conductive electrode. The choice of this bottom electrode is of primary importance as it drives the crystalline texture, the quality and the properties of the piezoelectric films. Obviously, due to the high temperature necessary to crystallize the material into the perovskite phase, this electrode should be stable and neither oxidize or become insulating. Three families of electrodes can be considered. The first includes metal oxides such as RuO_2 [49], [50], [51] or Ir / IrO_2 [52], [53]. The later is now widely used in ferroelectric memories applications for its ability to solve fatigue problems. The second family is based on perovskite metal oxides such as $SrRuO_3$ or (La, Sr)CoO_3 (LSCO) [54]. But, the most often reported material is platinum as demonstrated by Al-Shareef [49] and Maeder [55]. 100 nm thick Pt {111}-textured thin films grown on 10 nm thick TiO_2/Ti adhesion layers on thermally oxidized silicon substrates have been used in this thesis. The function of the TiO_2 layer is to passivate partially the adhesion layer [55] in order to prevent the interdiffusion of the Ti on top of the platinum electrode potentially modifying there the nucleation conditions [56]. A homogeneous {111} texture of the platinum is important to obtain a homogeneous nucleation of the perovskite.

The growth of PZT thin films is nucleation controlled [57]. It means that heterogeneous nucleation is preferred over homogeneous nucleation. This is very important for chemical solution deposition (CSD) process as it allows obtaining a columnar film microstructure nucleated at the bottom electrode.

One of the first method used to control the film texture was to influence the nucleation kinetics by means of the heating rates as demonstrated by Aoki [58] and Brooks [45] in 1994. They introduced an intermediate heating treatment at 480°C and 650°C to obtain {100} and {111} film texture respectively. In both cases, the films were then crystallized at 650°C during 10 min in air.

But nucleation controlled growth allows also to choose the texture of the film by using suitable combination of seeding layer / electrode. In 1998, the controlled growth of {111}-textured PZT thin films has been demonstrated by Muralt using few nm thick titania (TiO_2) seed layer on platinized electrode [59]. In 1999, Hiboux reported that {100}-textured thin films can be obtained using 10 nm sputter deposited {100}-oriented $PbTiO_3$ (PT) seeding layers [60], [61], [27]. On RF magnetron sputtered PZT films, Cattan reported in 1996 a dramatic change of texture as the thickness of $PbTiO_3$ seed layer was changing from 2 to 40 nm [62]. In this study, the {100}-texture was obtained with 5 nm (beginning of the junction between the PT islands) and with 7.5-15 nm (swinging of the cell). Above 20 nm, it gives {111}-textured PZT films.

Similar results were obtained by Ishikawa in 1998. 30 nm $PbTiO_3$ deposited by pulsed laser deposition (PLD) was used to seed {100}-textured sol-gel PZT films [63].

1.5 STATE-OF-THE-ART OF PZT THIN FILMS PIEZOELECTRIC PROPERTIES

Since PZT thin films have been synthesized in the 70's [64], there was always the question how well the exceptional properties of bulk ceramics may be reproduced in thin films as there are evident differences in microstructures, deposition temperature and operations conditions. In ceramics, grains are randomly oriented but in thin films, they tend to have a specific texture, mostly related to the substrate nature. The texture as well as processing issues and the mechanics of the interface between the film and the substrate have a strong influence on the properties. In particular, the latter issue, known as the clamping effect, transforms the piezoelectric properties of the bulk ceramics into thin films effective values [12], [13], [65] as shown previously in section 1.2.2.

For bulk PZT ceramics, it is known that the piezoelectric activity is peaking at the morphotropic phase boundary (MPB), with Zr = 0.53. The question is still open for thin films as residual stress, substrate clamping, domain contribution and the film texture may influence this maximum.

1.5.1 *Longitudinal piezoelectric coefficient* $d_{33,f}$

The measurement of the effective $d_{33,f}$ piezoelectric coefficient of thin films is not trivial since in many experiments one cannot separate the longitudinal d_{33} effect from d_{31} or e_{31} transverse contributions due to substrate bending. The only reliable technique proved to be the double side interferometry (double beam) measuring exclusively the thickness change of the film (see chapter 2). The earliest reliable data were given by Kholkin in 1995 [66] and by Taylor in 1996 [67]. Permittivity of 1000 - 1100 and remanent $d_{33,f}$ values of 65 pm/V (0.3 µm film) to 90 pm/V (1.8 µm film) have been obtained on {111}-textured PZT films deposited by sol-gel.

Beforeas 1995, longitudinal $d_{33,f}$ values given by Udayakumar in 1990 (220 pC/N) for 0.45 µm 52/48 PZT films [68], [69] or by Chen in 1995 (200 - 340 pC/N) [70] certainly suffer from incorrect measurement techniques that includes transverse effect contributions due to the substrate bending. The reported values were also measured under DC bias and no remanent coefficients were given. Many other examples of unreliable $d_{33,f}$ measuring techniques can be found in the literature. Chu reported in 1998 $d_{33,f}$ coefficients up to 180 pC/N for {100} and

{111}-texture films (0.25 - 2.5 μm thick) using a static uniaxial stress setup [71]. And in 2002, surprising $d_{33,f}$ values up to 800 pC/N on PZT films using the same technique have been measured by Fu [72]. Using standard mechanics, it has been demonstrated by Damjanovic, Muralt and Barzegar that the static uniaxial stress setup yields strong transverse contributions due to the substrate bending, which enhance the measured $d_{33,f}$ coefficient [73].

1.5.2 *Transverse piezoelectric coefficient* d_{31} *or* $e_{31,f}$

Very few reports exist on the measurement of the transverse piezoelectric coefficient d_{31} or $e_{31,f}$. These coefficients are, however, the relevant values in all microsystems based on deflecting structures such as cantilevers or vibrating membranes. As shown in section 1.2.2, the measurement of the d_{31} coefficient is subject to important assumptions concerning the elastic properties (s_{11}, s_{12}) of the PZT thin films which are unknown. In most cases, bulk values were taken. The direct measurement of the $e_{31,f}$ coefficient is thus more suitable as it is not necessary to know the elasticity of the film (see equation 1.5).

The determination of the transverse piezoelectric coefficient often relies on the measurement of a transverse deflection of a beam as a function of an applied voltage under quasi-static (off resonance) conditions. Value of -88 pC/N for 0.45 μm 52/47 PZT film has been reported by Udayakumar in 1990 [68] that corresponds to an $e_{31,f}$ of -9 C/m^2 using elastic properties of bulk PZT. In 1996, Luginbuhl measured -32 pC/N ($e_{31,f}$ = -3,3 C/m^2) on PZT {111}-textured deposited on microbeams [74]. More recently, Dubois reported in 1999 the effective transverse piezoelectric coefficient $e_{31,f}$ for PZT {111}-textured films. The maximum was found for PZT 45/55 with $e_{31,f}$ = -8.3 C/m^2 [75]. This value was comparable to those obtained by Sheppard [76] as d_{31} up to -80 pC/N ($e_{31,f}$ = -8.2 C/m^2) for sputtered {111}-textured PZT 50/50, 3.3 μm thick films have been measured using the wafer flexure method [77].

1.5.3 *Influence of film texture*

In 1997, Du and Uchino calculated phenomenologically the crystal orientation dependence of the piezoelectric properties in thin films. They conclude that PZT films with rhombohedral composition (for example PZT 60/40) with {100} epitaxial orientation should exhibit maximum longitudinal piezoelectric constant [78], [79]. In 2000, Taylor measured the piezoelectric properties of rhombohedral thin films (PZT 60/40, 0.9 μm) for {100}, {111} and "random" crystallographic orientation [80]. Largest $d_{33,f}$ of 100 pm/V was obtained with {100}-textured films compared to 77 pm/V and 63 pm/V for random and {111}-textured thin films respectively. These results were in a good qualitative agreement with the theoretical prediction of Du and Uchino. In 2000, Hiboux also observed similar results with sputter deposited PZT films. On {100} films, $d_{33,f}$ of 82 pm/V was measured compared to 60 pm/V for {111} films [81].

PZT {100}-textured thin films seem to exhibit the best piezoelectric properties, with respect to the longitudinal coefficient $d_{33,f}$. However, the question remains open for the transverse piezoelectric coefficient $e_{31,f}$ which is involved in microsensors and actuators (MEMS). In 1999, Muralt demonstrated that the $e_{31,f}$ coefficient for {111}-textured PZT thin films was peaking at $Zr = 0.45$ with $e_{31,f} = - 8.3 \pm 0.6$ C/m^2, thus, in the tetragonal region of the phase diagram and has been explained by missing domains contributions at the MPB [82]. Compared to {111}-texture thin films, preliminary results have shown that {100}-textured PZT films exhibited superior piezoelectric properties. A more extended investigation was thus required for this orientation.

1.6 STATE-OF-THE-ART OF PIEZOELECTRIC MEMS BASED ON PZT FILMS

Since the early 90's, efforts have been made to integrate piezoelectric PZT thin films in microsystems (see [83] for a review). At that time, the devices were mainly based on simple diaphragm structures. In 1992, Flynn used a resonating PZT/Si_3N_4 diaphragm to rotate, by friction coupling, a small glass lens [84]. It was one of the first micromachined micromotor. The microfabrication process was limited to the gold top electrode patterning and to the membrane microstructuration by silicon bulk micromachining in TMAH. Since 1993, thanks to better understanding of PZT thin films integration, to improved deposition processes and microfabrication techniques, Muralt and coworkers from EPFL demonstrated the efficiency of PZT films for actuation of vibrators [85] and diaphragms [86] for ultrasonic micromotors [87].

In 1997, piezoelectric micromachined sonar transducers have been presented by Bernstein [88], [89]. Millimeter-sized ferroelectric monomorph sonar transducers have been built using sol-gel PZT on micromachined silicon wafers. The devices were still based on simple square or rectangular doped silicon (1-20 μm) / PZT (4 μm) diaphragms with size ranging from 140 to 2000 μm. To avoid parasitic capacitance, the contacting lines of the top electrodes are insulated with a polyimide film.

Since 1996, thanks to anisotropic silicon dry etching techniques, new devices structures such as cantilevers and bridges became possible to fabricate. Using piezoelectric thin films from EPFL, Luginbuhl reported the microfabrication of PZT/Si microcantilevers [74]. However, structure bending due to residual stress and low transverse piezoelectric coefficient ($e_{31,f}$ = -3.3 C/m^2) have been measured, showing that the integration and process flow still need improvements.

In 1999, Schroth reported the application of sol-gel deposited PZT films for actuation of 1D and 2D scanners [90]. In this work, the authors have pointed out the influence of the film stress on the residual bending of the structures and concluded that the design should be tolerant to technology induced deformation, in particular to PZT thin film stress. Devices of small size were suggested.

Cantilevers for atomic force microscope (AFM) or scanning force microscopy (SFM) are also a play ground for PZT piezoelectric thin films. Intensive research has been carried out in Japan by Suga since 1996. They showed that PZT thin films allowed the production of self-excited microcantilevers for dynamic SFM with inherent sensing and actuating capabilities [91], [92]. Still in Japan, Nikon Corporation demonstrated similar results with the use of PZT cantilever for noncontact AFM [93], [94].

Today, there is a need for the integration of highly sensitive functional materials such as {100}-textured PZT thin films. As the device structures become more and more complex, the microfabrication of piezoelectric MEMS is facing new challenges in:

- The deposition of high quality PZT films on a wafer scale with greater thickness (a film of 5 μm thick would match the requirements for ultrasonic transducers applications)
- The integration on silicon (in particular, the control of film texture and the stress compensation)
- The need of new and dedicated microfabrication processes to produce complex devices with micron resolution (for example, partially unclamped diaphragms with small bridges and narrow grooves).

1.7 AIM OF THE THESIS

The aim of the thesis is thus to develop all the knowledge that is necessary for the successful realization of high performance piezoelectric microsystems based on PZT films/silicon deflecting structures. These structures are either very simple stress-compensated beams or membranes with various shapes and clamping conditions. The thesis will cover the following topics:

- The deposition and integration of high quality, {100}-textured, PZT thin films on silicon substrates.

- The development and mastering of advanced micromachining technologies such as electrode and PZT dry etching, silicon deep etching and silicon on insulator substrates.
- The study of concepts, physics, design, simulations of piezoelectric MEMS and the evaluation of demonstrators (acoustic sensor and ultrasonic transducer).

1.7.1 Deposition and integration of {100}-textured PZT thin films

Preliminary studies have shown that {100}-textured PZT thin films exhibited piezoelectric properties larger than state-of-the-art PZT films (often {111} or randomly textured). The actual piezoelectric properties of {111}-textured films are also far from what is expected from the calculated effective properties of bulk PZT ceramics. Thus, it is thought here to investigate further the wafer-scale sol-gel deposition of {100}-textured PZT thin films, to analyse microstructure, piezoelectric and dielectric properties as a function of composition and film thickness, and to find the optimal process conditions for as large as possible $e_{31,f}$, signal-to-noise ratio, and coupling constants.

1.7.2 Microfabrication of planar piezoelectric MEMS based on PZT thin films

Once the deposition and the integration of {100}-textured PZT films has been mastered, there remains the challenge of the microfabrication of the piezoelectric devices. The development of new microfabrication methods (dry etching of PZT, platinum bottom electrode and deep silicon etching) are necessary to produce complex devices with micron scale resolution. The goal here is to acquire all the process knowledge that is necessary to produce high quality and reproducible piezoelectric MEMS based on deflecting structures (beams or partially clamped membranes).

1.7.3 Piezoelectric MEMS demonstrators

As the first two issues have been solved, applications can be considered. In this section, the objectives are to apply the results obtained previously to produce new piezoelectric microsystems such as an acoustic sensor/microphone based on a PZT/Si cantilever and a piezoelectric micromachined ultrasonic transducers (p-MUT) for non-destructive testing.

1.7.4 Outline of the thesis

Apart this first chapter dedicated to a general introduction on the history, the background, the definitions of the piezoelectricity and its applications in MEMS, the thesis has been structured as follow:

Chapter 2 describes all the experimental methods used for the integration, the deposition and the characterization of sol-gel PZT {100}-textured thin films.

Chapter 3 presents the results of the study of piezoelectric and dielectric properties of highly {100}-textured PZT thin films. Structural analysis of the films, compositional and thickness dependence of the functional properties as well as aging behavior of the transverse piezoelectric coefficient are the major issues.

Chapter 4 results in a toolbox for the microfabrication of piezoelectric MEMS. Micromachining methods and process flow used in the microfabrication of piezoelectric devices based on deflecting structures are presented. A first application to the micromachining of PZT/Si microcantilevers is demonstrated and their basic electromechanical properties have been studied.

Chapter 5 presents the results of silicon/PZT piezoelectric micro-cantilevers as acoustic sensor for photoacoustic gas detector. The main issues are the cantilever stress compensation, the precise patterning of very narrow slits through PZT/Pt/SiO_2/Si by means of an all dry etching process and the device characterization and integration into photoacoustic gas detector.

Chapter 6 presents the results on the basic properties of piezoelectric micromachined ultrasonic transducer (pMUT). Apart microfabrication on SOI wafers, the admittance in air and liquid as well as ultrasonic wave propagation have been measured.

Chapter 7 is the conclusion and discuss potential opportunities for the future.

1.8 REFERENCES

1. Fluitman, J., *Microsystems technology: objectives.* Sensors and Actuators A, 1996. **56**: p. 151-166.
2. Vogler, D., *MEMS: A fast growing nich.* Solid State Technology, 2002. **January**: p. 26,29.

3. Feynman, R.P., *There's plenty of room at the bottom.* presented at the annual meeting of the American Physical Society, Caltech, 1959.
4. Bishop, D., A. Heuer, and D. Williams, *Microelectromechanical Systems: Technology and Applications*, in *MRS Bulletin.* 2001.
5. Senturia, S.D., *Microsystems design.* 2001, Boston: Kluwer Academic.
6. Ayazi, F. and K. Najafi, *High aspect-ratio polysilicon micromachining technology.* Sensors and Actuators A, 2000. **87**(1-2): p. 46-51.
7. Ayazi, F. and K. Najafi, *An all-silicon single-wafer micro-g accelerometer with combined surface and bulk micromachining process.* Journal of Microelectromechanical Systems, 2000. **9**(4): p. 544-550.
8. Muralt, P. *Piezoelectric thin films: from smart materials to smart applications.* in *ISIF.* 2000. Aachen.
9. Curie, J. and P. Curie, *Développement, par pression, de l'électricité polaire dans les cristaux hémièdres à faces inclinées.* C. R. Acad. Sc. Paris, 1880. **91**: p. 294-295.
10. Curie, J. and P. Curie, *Contraction et dilatation produite sur les cristaux hémièdres à faces inclinées.* C. R. Acad. Sc. Paris, 1881. **93**: p. 1137.
11. Nye, J.F., *Physical Properties of crystals: their representation by tensor and matrices.* 1985, Oxford: Oxford University Press.
12. Lefki, K. and J.M. Dormans, *Measurement of piezoelectric coefficient of ferroelectric thin films.* J. Appl. Phys., 1994. **76**(3): p. 1764-1767.
13. Muralt, P., *Piezoelectric thin films for MEMS.* Integrated Ferroelectrics, 1997. **17**: p. 297-307.
14. King, S.L., J.G.E. Gardeniers, and I.W. Boyd, *Pulsed-laser deposited ZnO for device applications.* Applied Surface Science, 1996. **96-98**: p. 811-818.
15. Jaffe, B., W.R. Cook, and H. Jaffe, *Piezoelectric Ceramics.* 1971, London: Academic Press.
16. Dubois, M.-A., *Aluminium nitride and lead zirconate-titanate thin film for ultrasonic applications: integration, properties and devices.*, in *Thesis n°2086.* 1999, Ecole Polytechnique Fédérale de Lausanne: Lausanne.
17. Gardeniers, J.G.E., Z.M. Ritmersma, and G.J. Burger, *Preferred orientation and piezoelectricity in sputtered ZnO films.* J. Appl. Phys., 1998. **83**: p. 7844-7854.
18. Sherrit, S., H.D. Wiederick, and B.K. Mukherjee, *A complete characterization of the piezoelectric, dielectric and elastic properties of Motorola PZT 3203 HD including losses and dispersion.* Proc. SPIE, 1997. **3037**: p. 158-169.

19. Berlincourt, D.A., C. Cmolik, and H. Jaffe. *Piezoelectric properties of polycrystalline lead titanate zirconate compositions.* in *Proceedings of IRE48.* 1960. New-York.
20. Tsubouchi, K. and N. Mikoshiba, *Zero-Temperature-Coefficient SAW Devices on AlN Epitaxial Films.* IEEE Tran. UFFC, 1985. **SU-32**(5): p. 634-644.
21. Auld, B.A., *Acoustic Field and Waves in Solids.* Vol. 1. 1973, New-York: Wiley Interscience.
22. Muralt, P., *Ferroelectric thin films for micro-sensors and actuators: a review.* J. Micromech. Microeng., 2000. **10**: p. 136-146.
23. Oikawa, M. and K. Toda, *Preparation of PZT thin films by an electron beam evaporation technique.* Appl. Phys. Lett., 1976. **29**(8): p. 491-492.
24. Castellano, R.N. and L.G. Feinstein, *Ion-beam deposition of thin films of ferroelectric PZT.* J. Appl. Phys., 1979. **50**(6): p. 4406-4411.
25. Ischida, M., et al., *Epitaxial growth of ferroelectric PLZT thin films.* Journal of Crystal Growth, 1978. **45**: p. 393-398.
26. Maeder, T., *Germination et croissance de films minces de PZT sur silicium passivé et substrats métalliques,* in *Material Science and Engineering.* 1997, EPFL: Lausanne.
27. Hiboux, S., *Study of growth and properties of in-situ sputter deposited PZT thin films,* in *Thesis n°2510.* 2001, Ecole Polytechnique Fédérale de Lausanne, EPFL: Lausanne.
28. Ramesh, R., et al., *Pulsed laser ablation-deposition and characterization of ferroelectric metal oxide heterostructures,* in *Science and technology of electroceramic thin film,* O.A.a.R. Waser, Editor. 1995, Kluwer: Dordrecht, The Netherlands. p. 1-22.
29. Sakashita, Y., et al., *Preparation and electrical properties of MOCVD-deposited PZT thin films.* J. Appl. Phys., 1991. **69**(12): p. 8352-8357.
30. Keijser, M.d., P.J. Van Veldhoven, and G.J.M. Dormans, *Organometallic chemical vapor deposition of lead zirconate titanate,* in *Science and technology of electroceramic thin films,* O. Auciello and R. Waser, Editors. 1995, Kluwer: Dordrecht, The Netherlands. p. 75-84.
31. Hong, E., et al., *Preparation and characterization of PZT thin films by MOCVD using a solid delivery system.* J. Mater. Res., 2000. **15**(6): p. 1284-1290.
32. Chen, I.-S., et al., *Preparation of piezoelectric PZT thin films by MOCVD for MEMS applications.* Mat. Res. Soc. Symp. Proc., 2000. **596**: p. 541-547.
33. Roeder, J.F., et al., *Liquid-delivery MOCVD: Chemical and Process Perspectives on Ferroelectric Thin Film Growth.* Adv. Mater. Opt. Electron., 2000. **10**: p. 145-154.
34. Chandler, C.D., C. Roger, and M.J. Hampden-Smith, *Chemical aspects of solution routes to perovskite-phase mixed-metal oxides from metal-organic precursors.* Chemical

Review, 1993. **93**: p. 1205-1241.

35. Livage, J., M. Henry, and C. Sanchez, *Sol-gel chemistry of transition metal oxides.* Solid State Chemistry, 1988. **18**: p. 259-341.
36. Brinker, C.J. and G.W. Scherer, *Sol-gel science: The physics and chemistry of sol-gel processing.* 1990, San Diego: Academic Press, inc.
37. Gurkovich, S.R. and J.B. Blum, *Preparation of monolithic lead-titanate by sol-gel process*, in *Ultrastructure Processing of Ceramics, Glasses and Composites*, L.L.H.a.D.R. Ulrich, Editor. 1984, Wiley-Interscience: New-York. p. 152-160.
38. Budd, K.D., S.K. Dey, and D.A. Payne, *Sol-gel processing of PT, PZ, PZT and PLZT thin films.* Br. Ceram. Proc., 1985. **36**: p. 107-121.
39. Schwartz, R.W., et al., *Solution chemistry effects in PZT thin films processing.* Integrated Ferroelectrics, 1992. **2**: p. 243-254.
40. Schwartz, R.W., et al., *Sol-gel processing of PZT thin films: A review of state-of-the-art and process optimisation strategies.* Integrated Ferroelectrics, 1995. **7**(1-4): p. 259-277.
41. Schwartz, R.W., et al., *Comments on the effects of solution precursor characteristics and thermal processing conditions on the crystallisation behaviour of sol-gel derivedc lead zirconate titanate thin films.* J. Mat. Res., 1997. **12**(2): p. 444-456.
42. Schwartz, R.W., *Chemical Solution Deposition of Perovskite Thin Films.* Chem. Mater., 1997. **9**: p. 2325-2340.
43. Seifert, A., et al., *Processing Optimization of Solution Derived* $PbZr_{1-x}Ti_xO_3$ *thin films for piezoelectric applications.* Integrated Ferroelectrics, 2001. **35**(1-4): p. 159-166.
44. Chen, S.Y. and C. I.W., *Cracking during pyrolysis of oxide thin films. Phenomenology, mechanisms, and mechanics.* J. Am. Ceram. Soc., 1995. **78**(11): p. 2929-2939.
45. Brooks, K.G., et al., *Orientation of Rapid Thermally Annealed Lead Zirconate Titanate Thin Films on (111) Pt substrates.* J. Mat. Res., 1994. **9**(10): p. 2540-2553.
46. Tuttle, B.A., et al., *Characterisation of chemically prepared PZT thin films.* Mat. Res. Soc. Symp. Proc., 1990. **200**: p. 159-165.
47. Chen, J., et al., *Rapid thermal annealing of sol-gel derived lead zirconate titanate thin films.* J. Appl. Phys., 1992. **71**(9): p. 4465-4469.
48. Lefevre, M.L., et al., *Microstructural development in sol-gel derived lead zirconate titanate thin films: the role of the precursor stoichiometry and processing environment.* J. Mater. Res., 1996. **11**(8): p. 2076-2084.
49. Al-Shareef, H.N., et al., *Electrodes for ferroelectric thin films.* Integrated Ferroelectrics, 1993. **3**: p. 321-332.

50. Vijay, D.P. and S.B. Desu, *Electrodes for PZT ferroelectric thin films.* J. Electrochem. Soc., 1993. **140**(9): p. 2640-2644.

51. Maeder, T., et al., *Conducting Barriers for Direct Contact of PZT Thin Films on Reactive Substrates.* Journal of The Electrochemical Society, 1999. **146**(9): p. 3393-3397.

52. Nakamura, T., et al., *Preparation of PZT thin films on Ir and* IrO_2 *electrodes.* Jpn. J. Appl. Phys., 1994. **33**(9B): p. 5207-5210.

53. Nakamura, T., et al., *Electrical properties of PZT thin films capacitors on Pt and Ir electrodes.* Jpn. J. Appl. Phys., 1995. **34**(9B): p. 5184-5187.

54. Ramesh, R., et al., *Ferroelectric LSCO/PZT/LSCO heterostructures on silicon via template growth.* Appl. Phys. Lett., 1993. **63**: p. 3592-3594.

55. Maeder, T., L. Sagalowicz, and P. Muralt, *Stabilized Platinum Electrodes for Ferroelectric Film Deposition using Ti, Ta and Zr Adhesion Layers.* Jpn. J. Appl. Phys., 1998. **37**: p. 2007-2012.

56. Willems, G.J., et al., *Nucleation and orientation of sol-gel PZT thin films on Pt electrodes.* Integrated Ferroelectrics, 1997. **15**: p. 19-28.

57. Chen, K.C. and J.D. Mackenzie, *Crystallization kinetics of metallo-organics derived thin film.* Mat. Res. Soc. Symp. Proc., 1990. **180**: p. 663-668.

58. Aoki, K., et al., *Dielectric Properties of (111) and (100) Lead-Zirconate-Titanate Films Prepared by Sol-Gel Technique.* Jpn. J. Appl. Phys., 1994. **33**: p. 5155-5158.

59. Muralt, P., et al., *Texture control of* $PbTiO_3$ *and* $Pb(Zr, Ti)O_3$ *thin films with* TiO_2 *seeding.* J. Appl. Phys., 1998. **83**(7): p. 3835-3841.

60. Maeder, T., et al., *Pb(Zr,Ti)O3 Thin Films by In-situ Reactive Sputtering on Micromachined Membranes for Micromechanical Applications.* British Ceram. Proc., 1995. **54**: p. 206-218.

61. Hiboux, S. and P. Muralt, *Piezoelectric and Dielectric Properties of Sputter Deposited (111), (100) and Random-Textured Pb(ZrxTi1-x)O3 (PZT) Thin Films.* Ferroelectrics, 1999. **224**: p. 315-322.

62. Cattan, E., et al., *Influence of* $PbTiO_3$ *buffer layers on microstructural properties of PZT films deposited by sputtering.* Mat. Res. Soc. Symp. Proc., 1996. **433**: p. 291-296.

63. Ishikawa, K., et al., *Effect of* $PbTiO_3$ *seeding layer on the growth of sol-gel-derived* $Pb(Zr_{0.53}\,Ti_{0.47})O_3$ *thin film.* Jpn. J. Appl. Phys., 1998. **37**: p. 5128-5131.

64. Phillips, L.S. and B.S. Ma, *Ferroelectric films by flash evaporation of PZT.* Electronics Components, 1971. **12**: p. 523-526.

65. Xu, F., et al., *Domain wall motion and its contribution to the dielectric and piezoelectric properties of lead zirconate titanate films.* Journal of Applied Physics, 2001. **89**(2): p.

1336-1348.

66. Kholkin, A., et al., *Interferometric study of piezoelectric degradation in ferroelectric thin films.* Microelectronic Engineering, 1995. **29**: p. 261-264.

67. Taylor, D.V., et al. *Thickness dependence of electrical and electromechanical properties of sol-gel derived PZT thin films.* in *Electroceramics V.* 1996. Aveiro (Portugal): European Ceramic Society.

68. Udayakumar, K., et al. *Sol-Gel derived PZT thin films for switching applications.* in *7th International Symposium on Application of Ferroelectrics.* 1990. Urbana-Champaign, IL.

69. Udayakumar, K., et al. *Ferroelectric thin film ultrasonic micromotors.* in *4th IEEE workshop MEMS.* 1991. Nara, Japan.

70. Chen, H.D., et al., *Electrical properties'maxima in thin films of lead-zirconate lead-titanate solid solution system.* Appl. Phys. Lett., 1995. **67**(23): p. 3411-3413.

71. Chu, F., et al., *Thickness dependence of the electrical properties of sol-gel derived lead zirconate titanate thin films with (111) and (100) texture.* Mat. Res. Soc. Symp. Proc., 1998. **493**: p. 409-414.

72. Fu, D., et al., *Observation of piezoelectric relaxation in ferroelectric thin films by continuous charge integration.* Jpn. J. Appl. Phys., 2001. **40**: p. 5683-5686.

73. Barzegar, G., et al., *Piezoelectric response of thin films determined by charge integration technique: Substrate bending effects.* J. Appl. Phys., 2003, **93** (8)

74. Luginbuhl, P., et al., *Piezoelectric cantilever beams actuated by PZT sol-gel thin film.* Sensors and Actuators A, 1996. **54**: p. 530-535.

75. Dubois, M.-A. and P. Muralt, *Measurement of the effective transverse piezoelectric coefficient $e_{31,f}$ of AlN and PZT thin films.* Sensors and Actuators A, 1999. **77**(2): p. 106-112.

76. Shepard, J.F., et al., *Characterization and aging response of the d_{31} peizoelectric coefficient of lead zirconate titanate thin films.* J. Appl. Phys., 1999. **85**(9): p. 6711-6716.

77. Shepard, J.F., P.J. Moses, and S. Troiler-McKinstry, *The wafer flexure technique for the determination of the transferse piezoelectric coefficient (d31) of PZT thin films.* Sensors and Actuators A, 1998. **71**: p. 133-138.

78. Du, X.-H., U. Belegundu, and K. Uchino, *Crystal orientation dependence of piezoelectric properties in lead zirconate titanate: theoretical expectation for thin films.* Jpn. J. Appl. Phys., 1997. **36**(9A): p. 5580-5587.

79. Du, X.-H., et al., *Crystal orientation dependence of piezoelectric properties of lead zirconate titanate near the morphotropic phase boundary.* Appl. Phys. Lett., 1998.

72(19): p. 2421-2423.

80. Taylor, D.V. and D. Damjanovic, *Piezoelectric properties of rhombohedral Pb(Zr, Ti)O_3 thin films with (100), (111), and "random" crystallographic orientation.* Appl. Phys. Lett., 2000. **76**(12): p. 1615-1617.

81. Hiboux, S., P. Muralt, and N. Setter, *Orientation and composition dependence of piezoelectric-dielectric properties of sputtered PZT thin films.* Mat. Res. Soc. Symp. Proc., 2000. **595**: p. 499-504.

82. Muralt, P., et al., *In-plane Piezoelectric coefficient of PZT Thin Films as a Function of Composition.* Ferroelectrics, 1999. **224**: p. 235-242.

83. Muralt, P., *PZT thin films for microsensors and actuators: Where do we stand ?* IEEE Transactions on ultrasonics, ferroelectrics, and frequency control. 2000 **47**(4): p 903-915

84. Flynn, A.M., et al., *Piezoelectric micromotors for microrobots.* J. Microelectromechanical Sytems, 1992. **1**: p. 44-51.

85. Muralt, P., et al., *Fabrication and characterization of PZT thin film vibrators for micromotors.* Sensors and Actuators A, 1995. **48**: p. 157-165.

86. Muralt, P., et al., *Piezoelectric actuation of PZT thin-film diaphragms at static and resonant conditions.* Sensors and Actuators A, 1996. **53**: p. 398-404.

87. Dubois, M.-A. and P. Muralt, *PZT Thin Film Actuated Elastic Fin Micromotor.* IEEE Transactions on Ultrasonics, Ferroelectrics, and Frequency Control., 1998. **45**(5): p. 1169-1177.

88. Bernstein, J.J., et al., *Micromachined high frequency ferroelectric sonar transducers.* IEEE Tran. UFFC, 1997. **44**(5): p. 960-969.

89. Bernstein, J., et al. *Micromachined ferroelectrics transducers for acoustic imaging.* in *1997 International Conference on Solid-State Sensors and Actuators.* 1997. Chicago.

90. Schroth, A., et al., *Application of sol-gel deposited thin PZT film for actuation of 1D and 2D scanners.* Sensors and Actuators A, 1999. **73**: p. 144-152.

91. Lee, C., et al., *Characterization of micromachined piezoelectric PZT force sensors for dynamic scanning force microscopy.* Rev. Sci. Instrum., 1997. **68**(5): p. 2091-2100.

92. Lee, C., T. Itoh, and T. Suga, *Self-excited piezoelectric PZT microcantilevers for dynamic SFM - with inherent sensing and actuating capabilities.* Sensors and Actuators A, 1999. **72**: p. 179-188.

93. Watanabe, S. and T. Fujii, *Micro-fabricated piezoelectric cantilever for atomic force microscopy.* Rev. Sci. Instrum., 1996. **67**(11): p. 3898-3903.

94. Miyahara, Y., *PZT cantilever for non-contact atomic force microscopy.* Appl. Surf. Sci., 1999. **140**: p. 428-431

CHAPTER 2

EXPERIMENTAL METHODS

The aim of this chapter is to summarize all the experimental methods used in the study of {100}-oriented PZT thin films presented in chapter 3. The deposition and integration processes as well as characterization methods are described in details.

2.1 DEPOSITION AND INTEGRATION OF SOL-GEL PZT THIN FILMS ON SILICON

2.1.1 Deposition of platinum bottom electrodes

Platinum bottom electrodes used in this thesis (excluding any seeding layer) were sputter deposited in a Balzers BAS-450 system with 10"x5" magnetron units. Base pressure amounts to typically 5e-7 mbar. First, 2 nm Ti adhesion layer is deposited on passivated (0.6 to 1.2 μm of thermal SiO_2) silicon wafers. Then a barrier layer consisting of about 20 nm TiO_2 is deposited by means of RF sputtering from a TiO_2 target. Finally, 100 to 120 nm of platinum are deposited by DC sputtering to form the bottom electrode. Deposition conditions are summarized in Table 2.1. To obtain the {100}-texture in PZT films, 10 nm thick {100}-textured $PbTiO_3$ (PT) seeding layer is sputter deposited on the platinum bottom electrode in a Nordiko 2000 system (Nordiko Ltd. Havant, Hant, UK).

Table 2.1: Sputtering conditions for the Pt/TiO$_2$/Ti bottom electrode and PT seeding layer.

	thickness (nm)	pressure (mbar)	gas flow (sccm)	power (W/cm^2)	temperature (°C)
Pt/TiO$_2$/Ti	100 / 20 / 2	5.3e-3	50, Ar	3.2 / 3.2 / 2	300
PbTiO$_3$ seeding	10	2.1e-2	20, O$_2$	Pb 2.5 / Ti 6.2	500

Figure 2.1 shows the Θ-2Θ X-ray diffractogram of Pt/TiO$_2$/Ti bottom electrode on passivated silicon substrate. The (100) peak of PbTiO$_3$ appears at 20.8°.

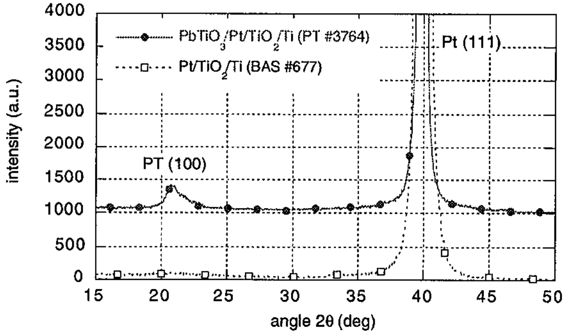

Figure 2.1: Θ-2Θ XRD diffractogram of Pt/TiO$_2$/Ti bottom electrode with the 10 nm PbTiO$_3$ (PT) seeding layer.

Figure 2.2 shows an SFM image of a 0.5 x 0.5 μm square of the platinum bottom electrode. (111) grains of about 50 nm have been measured. The RMS roughness is 1.87 Å.

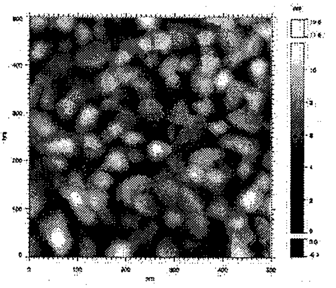

Figure 2.2: Scanning force microscopy of {111}-textured Pt/TiO$_2$/Ti/ bottom electrode deposited on passivated silicon. (D. Martrou - EPFL - LC, 2002)

2.1.2 Preparation of PZT solution precursors

Five precursor solutions of rhombohedral, MPB and tetragonal Pb(Zr_x, Ti_{1-x})O_3 with x = 0.3, 0.4, 0.45, 0.53 and 0.6 were synthesized using an improved 2-methoxyethanol route of Budd [1], [2]. The first step of the precursor preparation was the dissolution of the lead acetate reagent in 2-methoxyethanol followed by a distillation to remove water. The dehydrated powder is redissolved in dry 2-methoxyethanol during 1 hour at 110°C. Titanium and zirconium alkoxides were added and the solution was refluxed during 1 hour at 120°C. A vacuum distillation at 300 mbar and 125°C was used to remove reaction by-products and to adjust the concentration of the precursors to 0.4 M for all compositions. Figure 2.3 shows a schematic of the precursor preparation. To improve the drying behavior of the sol-gel, 4% vol. formamide was added to the solution (inhibition of the hydrolysis [3]). The solution was then filtered through 0.2 μm PTFE syringe filter and stored under dry argon. The solution life-time is estimated to about 1 year. Two solution precursors were prepared in order to balance the lead loss during the rapid thermal annealing (RTA). The standard one has 10% lead excess and the solution used for the last layer before the RTA has 30% lead excess.

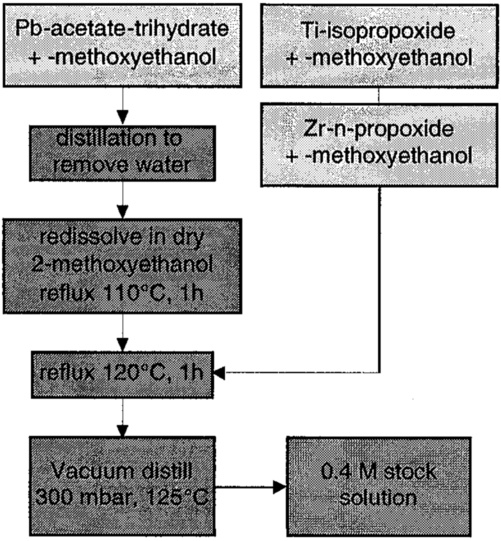

Figure 2.3: Schematic of the PZT solution precursors preparation

2.1.3 Deposition and crystallization of PZT thin films

CSD PZT thin films were deposited on platinized silicon wafer by multiple spin-coating at 3000 rpm for 40 s of the solution precursors. Each layer was subsequently slowly pyrolyzed at 350°C for 15 s (ramp of 20 °C/s). After the deposition of 4 single layers (3 layers with 10% lead excess, 1 layer with 30% lead excess), the PZT film was thermally annealed at 650°C for 1 min (standard) or 12 min (for the last RTA) using a rapid heating module (Process Products Corp., RTM 2016) in flowing oxygen. This operation was repeated 4 times to obtain 1 μm thin film. The heating rate used in the very first RTA was 30°C/s and is then reduced to 15°C/s for the following treatments. As film thickness of a single spin is about 60 nm, 16 and 64 single layers were required to form 1 and 4 μm thick PZT films respectively.

2.2 STRUCTURAL CHARACTERIZATION OF PZT THIN FILMS

2.2.1 Crystalline texture and microstructure

The crystalline texture and phase analysis were determined by X-ray diffraction on a Kristalloflex 805 (Siemens, Germany) diffractometer with CuK_α radiation. Θ-2Θ scans were carried out from 20 to 50° at 0.04° increment per 4 s. The texture index of the film (planes parallel to the surface only) has been obtained by normalizing the peak intensities with the corresponding peaks of a randomly oriented powder according to the following relation [4]:

$$P(hkl) = \frac{\dfrac{I(hkl)}{I_0(hkl)}}{\sum_{1}^{N} \dfrac{I(hkl)}{I_0(hkl)}} \tag{2.1}$$

where N is the number of peaks considered (in our case $N = 3$ as the relevant orientations are (100), (110) and (111)) and I(hkl) and I_0(hkl) are the integrated XRD peak intensities of the film and the randomly oriented PZT 52/48 powder (JCPDS file #33-784).

The surface and the cross-section morphology of the films were observed using scanning electron microscope (SEM) Philips XL30 (Eindhoven, Holland). On selected films, transmission electron microscopy (TEM) using Philips EM430 ST with built-in EDX detector was used for cross-sectional views and chemical analysis.

2.2.2 In-plane stress in thin films

The in-plane stress in thin films has been measured by observing the change of the curvature radius of the substrate before and after the film deposition. The change of curvature was recorded optically with a stress analysis instrument Tencor FLX-2900. The system is composed of a laser diode, a mirror and an array of photo-detectors. The laser beam is reflected by the surface of the sample and hits the detector at a position, which depend on the local angle made by the substrate and the horizontal reference.

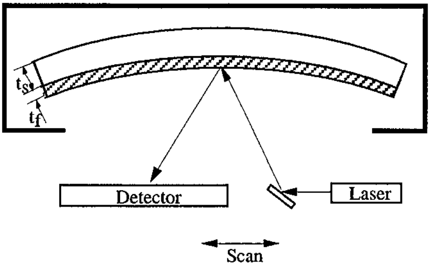

Figure 2.4: Measurement principle of the wafer curvature radius for film stress analysis.

The average curvature of the substrate is calculated by the least mean squares method. This procedure is applied before and after the film deposition and the average in-plane stress σ is calculated by the Stoney's formula:

$$\sigma = \frac{Y_s}{6(1-\upsilon_s)} \cdot \frac{t_s^2}{t_f} \cdot \left(\frac{1}{R} - \frac{1}{R_0}\right) \tag{2.2}$$

where $Y_s/(1\text{-}\nu_s)$ is the biaxial Young's modulus of the substrate (180.5 GPa for (100) oriented silicon wafers), t_s and t_f are the thickness of the substrate and the film respectively and R_0, R are the curvature radii before and after the film deposition. For PZT films, the curvature is measured for the first time after the film deposition and for the second time after the complete etching of the film. In that way, it is possible to take into account the modification of the bottom electrode due to the PZT deposition process.

2.3 FUNCTIONAL CHARACTERIZATION OF PIEZOELECTRIC THIN FILMS

2.3.1 Transverse and longitudinal piezoelectric coefficients

The relevant coefficients to measure in piezoelectric thin films are the effective values $d_{33,f}$ and $e_{31,f}$. Polycrystalline thin films exhibit a cylindrical symmetry where the polar axis is normal to the film plane, and the in-plane directions are equivalent. This symmetry is the same as of poled ceramics. Without loss of generality, one can reformulate the equations of state such that the free parameters are the in-plane strain (x_1, x_2) and the off-plane stress (σ_3). The direct effect reads then as follows [5]:

$$D_3 = e_{31,f} \cdot (x_1 + x_2) + d_{33,f}\sigma_3 + \varepsilon_{33,f}\varepsilon_0 E_3 \tag{2.3}$$

$$x_3 = d_{33,f}E_3 - c^E_{13}(x_1 + x_2) + \frac{\sigma_3}{c^E_{33}} \tag{2.4}$$

$$\sigma_{1,2} = -e_{31,f}E_3 + \left(c^E_{11} - \frac{\left(c^E_{13}\right)^2}{c^E_{33}}\right) \cdot x_{1,2} + \left(c^E_{12} - \frac{\left(c^E_{13}\right)^2}{c^E_{33}}\right) \cdot x_{2,1} + \frac{c^E_{13}}{c^E_{33}}\sigma_3 \tag{2.5}$$

where: $d_{33,f} = \frac{e_{33}}{c^E_{33}}$, $\varepsilon_{33,f} = \varepsilon^x_{33} + d_{33,f} \cdot \frac{e_{33}}{\varepsilon_0}$

The $d_{33,f}$ coefficient can be measured directly as x_3/E_3 provided that $x_1=x_2=\sigma_3=0$. This measurement has been done with a double-beam Mach-Zehnder interferometer (see Figure 2.5) that only measures the thickness change of a film clamped on a much thicker substrate (assuring $x_1=x_2=0$) at $\sigma_3=0$. The main advantage on this instrument lies in the fact that the film expansion along the 3-axis can be discriminated from the bimorph-like bending of the sample [6]. The modification of the optical path length is thus only affected by the film thickness variation.

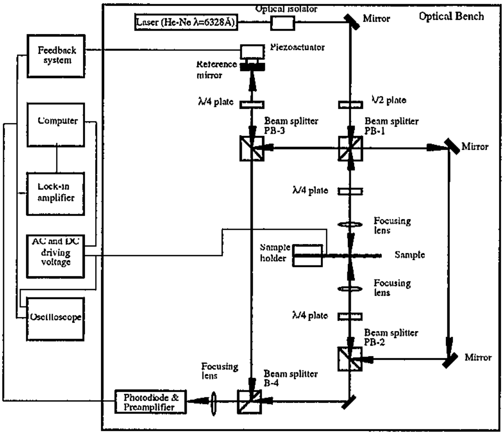

Figure 2.5: Schematic of the double beam interferometer [6]

The measurement of the transverse piezoelectric coefficient $e_{31,f}$ has been realized by means of a cantilever bending method (see Figure 2.6), collecting the charges as a function of x_1 and x_2 at zero σ_3 and electric field.

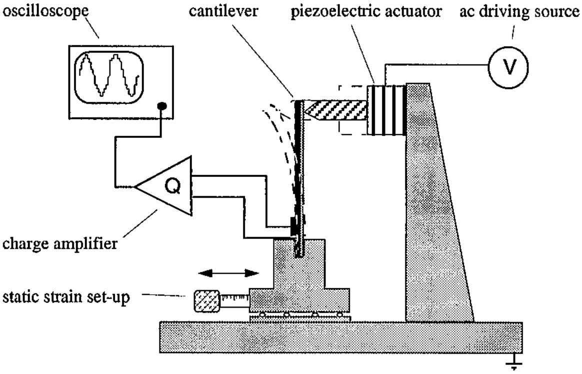

Figure 2.6: Schematic view of the measurement set-up for the $e_{31,f}$ transverse piezoelectric coefficient [7].

A small AC displacement (4.8 μm) is applied on the tip of the cantilever. The charges created by the strained piezoelectric film are collected by a very well defined top electrode. These charges are then converted to voltage by a charge amplifier and monitored on an oscilloscope. The effective transverse piezoelectric coefficient is calculated knowing the beam geometry, the clamping position and the beam deflection. Details about the sample preparation and the measurement technique can be found in [7]. Finally, prior to any measurements, the samples of all compositions are hot poled at 150°C under 50 to 250 kV/cm during 10 minutes.

2.3.2 Dielectric properties

The effective dielectric constant $\varepsilon_{33,f}$ (is theoretically in between fully clamped ε_{33}^{x} and free $\varepsilon_{33}^{\sigma}$) and the loss factor tan δ were measured with an LCR-meter HP-4194 from Hewlett-Packard. Measurements were carried out at 1 kHz and 10 kHz under different AC field (usually, 5 kV/cm amplitude on 1 μm film). Films thicknesses were obtained by profilometry (Alpha-Step 200, Tencor) and SEM observation.

2.4 REFERENCES

1. Budd, K.D., S.K. Dey, and D.A. Payne, *Sol-gel processing of PT, PZ, PZT and PLZT thin films.* Br. Ceram. Proc., 1985. **36**: p. 107-121.
2. Gurkovich, S.R. and J.B. Blum, *Preparation of monolithic lead-titanate by sol-gel process*, in *Ultrastructure Processing of Ceramics, Glasses and Composites*, L.L.H.a.D.R. Ulrich, Editor. 1984, Wiley-Interscience: New-York. p. 152-160.
3. Orcel, G. and L. Hench, *Effect of formamide additive on the chemistry of silica-gels. Part 1: NMR of silica hydrolysis.* Journal of Non-Crystalline Solids, 1986. **79**: p. 177-194.
4. Harris, G.B., *Quantitative measurements of preferred orientation in rolled uranium bars.* The Pilosophical Magazine, 1952. **43**(1): p. 113-123.
5. Muralt, P., *Piezoelectric thin films for MEMS.* Integrated Ferroelectrics, 1997. **17**: p. 297-307.
6. Kholkin, A.L., et al., *Interferometric measurements of electric field-induced displacements in piezoelectric thin films.* Rev. Sci. Instrum., 1996. **67**(5): p. 1935-1941.
7. Dubois, M.-A. and P. Muralt, *Measurement of the effective transverse piezoelectric coefficient* $e_{31,f}$ *of AlN and PZT thin films.* Sensors and Actuators A, 1999. **77**(2): p. 106-112.

CHAPTER 3

STUDY OF {100}-ORIENTED $Pb(Zr_x, Ti_{1-x})O_3$ PIEZOELECTRIC THIN FILMS FOR MEMS

3.1 INTRODUCTION

In MEMS based on piezoelectric thin films, two parameters govern the performances of the device: the transverse piezoelectric coefficient $e_{31,f}$ with the corresponding figures of merit and the piezoelectric film thickness. As the first parameter is directly related to the sensitivity of the device, the second is of primary importance to obtain large forces and high coupling factors in transducers applications. In {111}-textured PZT thin films studied previously, peaking transverse piezoelectric coefficient $e_{31,f}$ of -8.5 C/m^2 has been measured on 1 μm PZT 45/55 thin film [1]. However, during preliminary studies, it has been found that {100}-textured thin films exhibited even better properties. A more extended investigation was thus required to find optimal deposition process, growth conditions, {100} texture and film composition to achieve as high as possible $e_{31,f}$. To provide more force and power to the device, it is of a primary interest to integrate as thick as possible PZT films since the coupling factor is function of the active volume of the piezoelectric layer [2]. It is thus of interest to extend the thickness range of sol-gel films without incorporating porosity as it reduce the film hardness and the e_{ij} coefficients.

In this chapter, the growth and the functional properties of PZT {100}-textured films are investigated. The goals are to find texture and composition for optimal $e_{31,f}$ and further figures of merits (signal to noise ratio, coupling factors) and to increase film thickness up to 4 μm.

3.2 COMPOSITIONAL STUDY OF 1 μM {100}-TEXTURED PZT THIN FILMS

3.2.1 Structural analysis

For all compositions (Zr/Ti = 60/40, 53/47, 45/55, 40/60 and 30/70), highly {100}-textured thin films have been deposited. Figure 3.1 shows the Θ-2Θ X-ray diffractogram of the films as a function of the average Zr concentration.

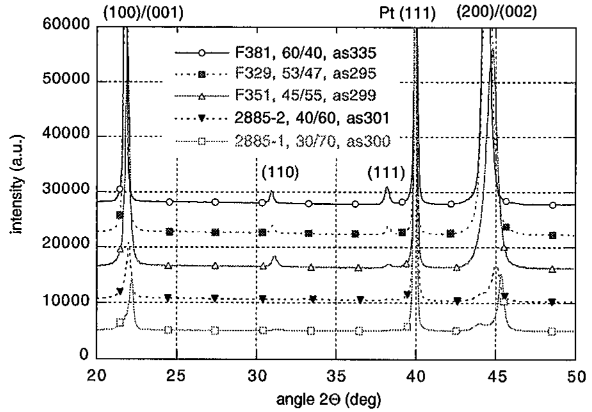

Figure 3.1: Θ-2Θ X-ray diffractogram of {100}-textured 1 μm PZT films deposited on $PbTiO_3/Pt/TiO_2/Ti/SiO_2/Si$ *substrate as a function of the average Zr concentration.*

The {100}-texture index are summarized in Table 3.1. For all compositions, values larger than 95% have been obtained.

Table 3.1: {100}-texture index of 1 μm PZT films as a function of composition

Film reference	Zr/Ti ratio	{100}-texture index
F381	60/40	95.4
F329	53/47	97.9
F351	45/55	98.0
#2885-2	40/60	97.5
#2885-1	30/70	98.2

Figure 3.2 shows SEM images of a top-view and a cross-section of 1 µm PZT 53/47 {100}-textured thin film. Dense film and a composition independent grain size of about 80 nm have been observed.

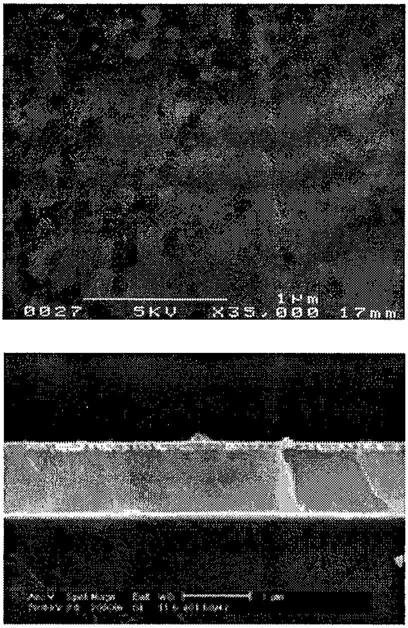

Figure 3.2: SEM images of a top-view and a cross-section of {100}-textured PZT 53/47 thin film (1 µm).

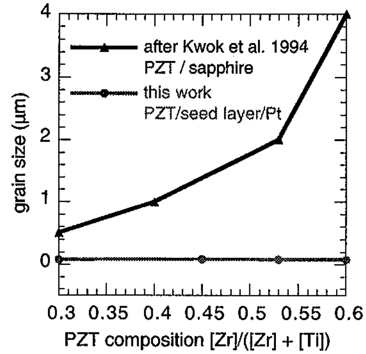

Figure 3.3: PZT film grain size as a function of the composition. Sapphire data from [3]

Compared to the data of Kwok [3] on PZT sol-gel films deposited on sapphire and annealed at the same temperature of 650°C, the constant grain size shows that the nucleation is mainly driven by the seed layer which has always the same composition ($PbTiO_3$, PT). The grain diameter is the same as for platinum grains (see Figure 3.4 and 3.5) indicating that the PT nuclei density is related to the platinum grain size.

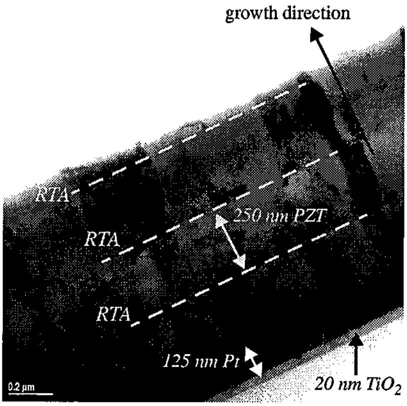

Figure 3.4: TEM image of a cross-section of 1 µm PZT film on PT/Pt/TiO_2 bottom electrode. The PZT thickness between two RTA is 0.25 µm (4 single spins).

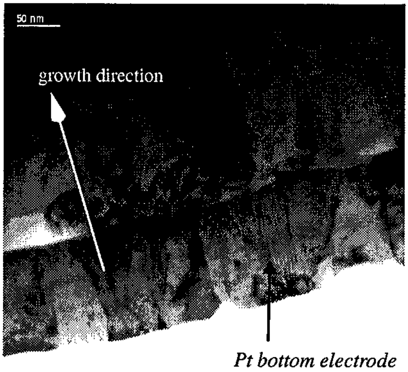

Figure 3.5: TEM image of a cross-section of the PZT/PT/Pt bottom electrode interface. The Pt grain size is 50-75 nm.

3.2.2 Optimization of the poling conditions

To obtain a net piezoelectric activity, the domains have to be aligned close to one direction. This process is achieved by applying an electrical field on the material. The poling process can be thermally activated and thus enhanced by increasing the sample temperature. To achieve the highest piezoelectric response, the poling conditions have been optimized with respect to the magnitude of the field, the temperature and the poling time.

Figure 3.6 shows the dependence of the $e_{31,f}$ coefficient as a function of poling field. For 1 µm film, electrical field larger than 200 kV/cm is required to obtain transverse piezoelectric coefficient larger than -12 C/m^2. This field corresponds to about 3 times the coercive field of the film (50 - 60 kV/cm for 1 µm film).

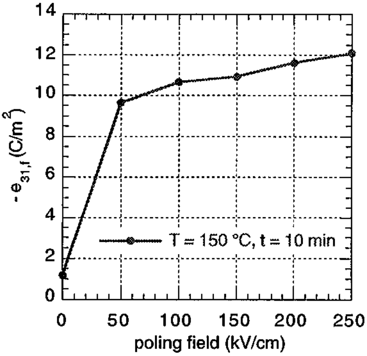

Figure 3.6: Transverse piezoelectric coefficient $e_{31,f}$ *of PZT 53/47 {100}-textured 1 μm thin film as a function of poling field.*

Figure 3.7 and 3.8 show the dependence of the piezoelectric coefficient $e_{31,f}$ as a function of poling time and poling temperature respectively.

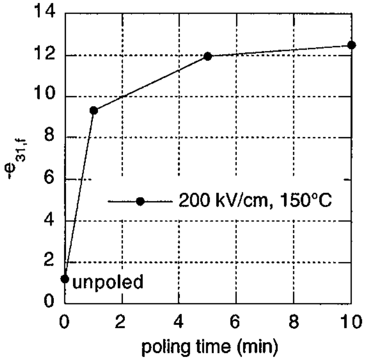

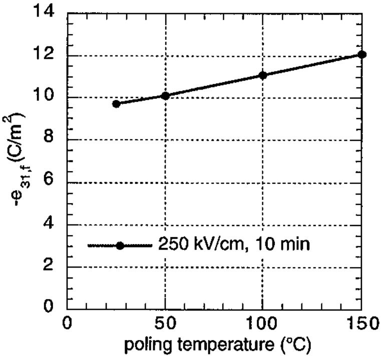

Figure 3.7: Transverse piezoelectric coefficient $e_{31,f}$ *of {100}-textured PZT 53/47 1 μm thin film as a function of poling time.*

Figure 3.8: Transverse piezoelectric coefficient $e_{31,f}$ *of {100}-textured PZT 53/47 1 μm thin film as a function of poling temperature.*

It turns out that an electric field of 250 kV/cm, a poling temperature of 150°C and a poling time of 10 min are the optimal poling conditions for 1 μm {100}-textured PZT thin films.

3.2.3 Transverse piezoelectric coefficients

Figure 3.9 shows the transverse piezoelectric coefficient $e_{31,f}$ as a function of the average Zr concentration. For comparison, data of {111}-textured sol-gel films from Muralt [1] are plotted as well. The results show that {100}-textured films exhibit higher transverse piezoelectric coefficients than {111}, peaking near the MPB (53% Zr) with a value of **-12.1 ± 0.3 C/m^2**. The {100}-texturing of PZT films allows thus an improvement of properties. To our present knowledge, the value of -12.1 ± 0.3 C/m^2 is the highest ever reported for PZT films grown on silicon and has been confirmed on our films by another laboratory applying another technique (-12.8 C/m^2 using wafer flexure method [4]). Previously reported values are -5 C/m^2 [5] and -8.4 C/m^2 [4], [6] (in this case we recalculated $e_{31,f}$ from the given d_{31} and the assumed elastic modulus and Poisson ratio given in the same paper). Interestingly, the maximal properties do not peak at the same composition. {111}-oriented films peak at 45/55 in the tetragonal side, whereas {100}-oriented films peak rather on the rhombohedral side of the morphotropic phase boundary, or close to it.

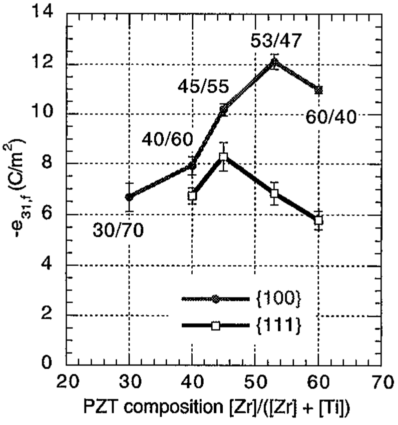

Figure 3.9: Effective transverse piezoelectric coefficients $e_{31,f}$ of {100} and {111}-textured PZT thin films (1 μm) as a function of average composition. {111} data from [1].

No calculations on e_{31} or d_{31} of single crystals have been made to date. However, phenomenological calculations have been made for d_{33} coefficients [7], [8], which have shown that d_{33} along (001) was higher on the rhombohedral side, whereas d_{33} along (111) should be larger on the tetragonal side. It was also concluded that d_{33} along (001) was larger than along (111). Our results show that $e_{31,f}$ follows the same tendencies.

In order to cross-check our results, we measured the transverse piezoelectric coefficient by means of the converse effect. The deflections of 9.5 mm long beams were measured as a function of ac applied voltage. The beams exhibited the same geometry as the ones used for the direct measurement, except that the top electrodes covered the whole beams. Figure 3.10 shows the deflection of a beam coated with a 1 μm thick {100}-textured PZT 53/47 film. A dc-bias was superimposed to avoid depolarization: $V(t)=V_0(1+\sin\omega t)$.

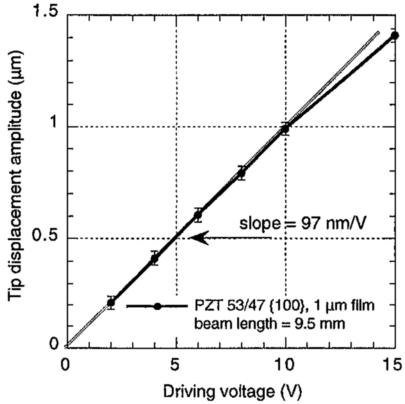

Figure 3.10: PZT/Si beam tip deflection as a function of ac unipolar driving electrical field. PZT: 53/47, {100}-texture, 1 μm. Silicon beam: L = 9.5 mm, w_b = 1.5 mm, h_{Si} = 390 μm, Top electrode: L = 9.5 mm, w_e = 1 mm

Following the derivation of Gardeniers [9], the tip deflection of the PZT/silicon beam is:

$$\delta(L) = -6 \cdot \frac{d_{31}}{s^E_{11,p} + s^E_{12,p}} \cdot \left(s_{11} - \frac{s^2_{12}}{s_{11}}\right)_{Si} \cdot \left(L \cdot L_e - \frac{L^2_e}{2}\right) \cdot \frac{1}{h^2_{Si}} \cdot \frac{w_e}{w_b} \cdot V \qquad (3.1)$$

where: d_{31} = transverse piezoelectric coefficient (pm/V)

$s^E_{11,p}$, $s^E_{12,p}$ = elastic compliance of silicon or PZT (m^2/N)

h_{Si}, h_p = substrate and PZT thickness (condition: $h_{Si} >> h_p$) (m)

w_e, w_b = beam and top electrode width (m)

L, L_e = beam and top electrode length (m) and $$\frac{d_{31}}{s_{11,p}^{E}+s_{11,p}^{E}} = e_{31,f} \tag{3.2}$$

If $w_e = w_b$ and $L_e = L$, equation (3.1) yields:

$$\delta(L) = -3 \cdot e_{31,f} \cdot \left(s_{11} - \frac{s_{12}^{2}}{s_{11}}\right)_{Si} \cdot \left(\frac{1}{h^{2}}\right)_{Si} \cdot L^{2} \cdot V \tag{3.3}$$

Except the Young modulus (Y = 91.2 GPa) given by Tuchiya [10], no data of the elastic compliance exists for PZT thin films. In a first approximation, elastic parameters have been approached by the bulk values $s_{11,p}^{E} = 13.8\times10^{-12}$ (m^2/N) and $s_{12,p}^{E} = -4.07\times10^{-12}$ (m^2/N) given by Jaffee [11].

In the linear region (between 2 and 10 V), a slope of 97 nm/V has been measured. Above 10 V, it is suggested that increasing of internal film stress yields smaller displacement and non-linear behavior. Using equation (3.3), an effective transverse piezoelectric coefficient **$e_{31,f}$ of −11.4 ± 1.1 C/m^2** is calculated. The difference between the coefficient measured with the direct and the converse effect is less than 5% and is compatible with experimental errors.

The $e_{31,f}$ of our films is superior to the $e_{31,f}$ derived from classical PZT ceramics data [11], [12] as – 9.6 C/m^2. To date it is not clear whether the improvement is due to a larger d_{31} (**-110 ± 10 pm/V** using the elastic compliance of ceramics) or due to smaller elastic compliances in thin films (stiffer). Whatever the experimental technique (beam in direct or converse mode, wafer flexure method) and according to the experimental errors, the {100}-textured PZT 53/47 thin film has shown the best transverse piezoelectric properties with **$e_{31,f}$ = -12 C/m^2**.

3.2.4 Dielectric properties

The dielectric permittivity and the loss factor measured at low field (5 kV/cm, 1 kHz) are given in Figure 3.11. Data of {111}-textured thin films from [1] are plotted as well.

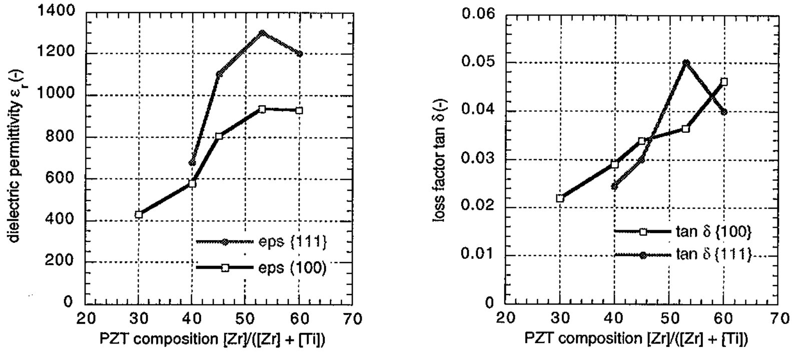

Figure 3.11: Left: dielectric permittivity; Right: dielectric loss factor as a function of average Zr concentration. Film thickness is 1 μm, AC field = 5 kV/cm at 1 kHz. {111} data from [1].

For (111) films, the maximum of the dielectric properties is observed at the MPB. For (100) films, the maximum seems to be in the rhombohedric part of the phase diagram, above 53% Zr. This result is similar to those observed for the piezoelectric properties. Major source of dielectric loss in ferroelectrics are domain wall oscillations. Figure 3.11 reflects the fact that near the MPB where the domain wall are more mobile, the dielectric constant as well as the dielectric loss are higher. As for the piezoelectric and dielectric properties, the dielectric loss seems to be larger for rhombohedric (100) and for tetragonal (111) films. However, it has not been investigated in details. Loss factor are ranging from 2% for tetragonal PZT 30/70 to about 4-5% for rhombohedric PZT 60/40.

Table 3.2 summarizes the functional properties of 1 μm PZT {100}-textured thin films as a function of average composition.

Table 3.2: Transverse piezoelectric coefficient and dielectric properties of {100}-textured PZT films as a function of average composition. Film thickness is 1 μm.

film reference	Zr/Ti	thickness (μm)	$-e_{31,f}$ (C/m^2)	$\varepsilon_{33,f}$ (-)	*tan δ* (-)
#2885-1	30/70	1.08	6.67 ± 0.55	428	0.022
#2885-2	40/60	0.9	7.92 ± 0.37	581	0.029
F351	45/55	1.0	10.19 ± 0.24	805	0.034
F329	**53/47**	**1.2**	**12.11 ± 0.31**	**935**	**0.037**
F381	60/40	1.2	10.99 ± 0.14	930	0.046

3.2.5 Figures of Merit

Until now we only evaluated the piezoelectric coefficients for optimization of properties. They describe directly achievable piezoelectric forces and charges. However, depending on application, more complex figures of merit (FOM) have to be considered (see Appendix A). Dielectric constant as well as dielectric loss contributes to signal-to-noise ratio and power efficiency. In sensors, the obtained signal is proportional to the piezoelectric coefficient $e_{31,f}$ while the dielectric noise current density is given by:

$$j_n = \sqrt{4k_BT\omega C\tan\delta} \qquad (\mathrm{A/Hz^{0.5}}) \qquad (3.4)$$

The signal-to-noise (S/N) figure of merit is thus defined by equation (3.5).

$$S/N = \frac{|e_{31,f}|}{\sqrt{\varepsilon_0\varepsilon_{33,f}\cdot\tan\delta}} \qquad (\mathrm{Pa^{0.5}}) \qquad (3.5)$$

Figure 3.12 shows that the signal-to-noise of {100}-textured PZT films is larger for Zr rich compositions but comparable to the one of {111} films for tetragonal compositions (Ti rich) due to the lower dielectric constant of {111}-textured films.

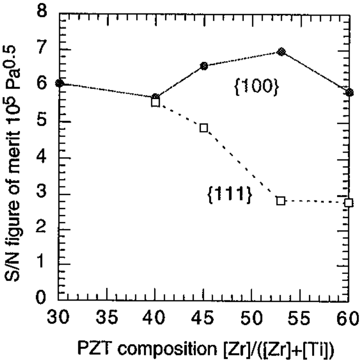

Figure 3.12: Signal-to-noise (S/N) FOM of {100} and {111}-textured 1 μm PZT thin films as a function of average composition.

In actuators, the relevant coefficient is the coupling factor k^2, which quantifies the energy transfer from the electrical system to the mechanical system [13]. The coupling coefficient depends on the geometry and the material involved. It is usually approached by finite element modeling. However, in some simple cases, k^2 can be calculated analytically. For a thin clamped disk, used as stator in ultrasonic micromotors [14], the coupling coefficient and the power efficiency figures of merit are given by:

Material's coupling factor $$(k_{p,f})^2 = \frac{2(e_{31,f})^2}{\varepsilon_0\varepsilon_{33,f}} \cdot \left(\frac{1-\nu}{Y}\right)_{Si} \tag{3.6}$$

Power efficiency $$\frac{(k_{p,f})^2}{\tan\delta} = \frac{2(e_{31,f})^2}{\varepsilon_0\varepsilon_{33,f}} \cdot \left(\frac{1-\nu}{Y}\right)_{Si} \cdot \frac{1}{\tan\delta} \tag{3.7}$$

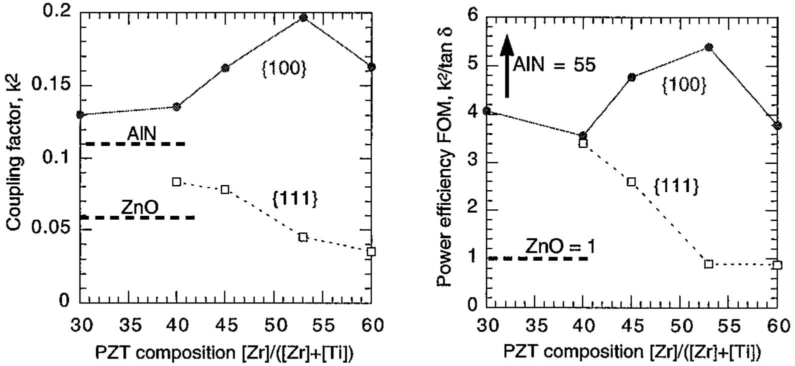

Figure 3.13: Left: coupling factor k^2; Right: power efficiency $k^2/\tan\delta$ of {100} and {111}-textured PZT thin films (1 μm) as a function of average composition. Data of {111}-textured films from [1]

In case of {100}-textured PZT thin films, it turns out that the 53/47 MPB composition is the best in all cases (see Figure 3.12 and 3.13). The situation is different for PZT {111} where a composition of 40/60 was found to be optimal for signal-to-noise, coupling constant and power efficiency. The FOM definitions and measured values are summarized in Table 3.3. For coupling coefficient and power efficiency, it was assumed that the PZT thin film is part of a composite structure that contains primarily silicon (Young modulus: Y = 130 GPa, Poisson's coefficient = 0.278).

Table 3.3: Figures of merit definitions and values for PZT {111} and {100}-textured PZT thin films

FOM	Definitions	**PZT {100} 53/47**	PZT {111} 40/60
$\varepsilon_{33,f}$ (-)	-	935	680
tan δ (-)	-	0.036	0.024
$-e_{31,f}$ (C/m^2)	-	**12.1**	6.73
S/N (10^5 Pa$^{0.5}$)	$\frac{\lvert e_{31,f}\rvert}{\sqrt{\varepsilon_0\varepsilon_{33,f}\cdot\tan\delta}}$	**7**	5.5
coupling factor k^2 (-)	$\frac{2(e_{31,f})^2}{\varepsilon_0\varepsilon_{33,f}}\cdot\left(\frac{1-\nu}{Y}\right)_{Si}$	**0.2**	0.08
power efficiency k^2/tan δ (-)	$\frac{2(e_{31,f})^2}{\varepsilon_0\varepsilon_{33,f}}\cdot\frac{1}{\tan\delta}\cdot\left(\frac{1-\nu}{Y}\right)_{Si}$	**5.4**	3.5

Due to its high transverse piezoelectric coefficient ($e_{31,f}$ = -12 C/m^2), {100}-textured PZT thin film at the morphotropic composition 53/47 is so far, the best material for application in piezoelectric MEMS, in particular for transducers and actuators. The coupling factor of PZT 53/47 {100}-textured is about 4 times higher than the one of ZnO and 2 times higher than PZT 40/60 {111}.

3.3 PROPERTIES OF {100}-TEXTURED PZT 53/47 THIN FILM AS A FUNCTION OF THICKNESS

PZT films integrated in devices are 0.5 to 2 μm thick (with one exception: 4 μm reported in [15]). Thicker films cause problems because of cracking and or formation of porosity. Two origins of cracking can be identified. One is specific to sol-gel processing and is due to shrinkage during the crystallization. The other is caused by the thermal mismatch with the substrate. The average thermal expansion of PZT 50/50 between process temperature (650°C) and phase transition (350°C) amounts to 8 ppm/°K, whereas silicon exhibits only 4 ppm/K. It was indeed observed that when using a zirconia substrate (6.4 ppm/°K), the upper limit of films without cracks could be increased to 7 μm [16]. However, zirconia substrate is of a little utility in MEMS as it is brittle and extremely difficult to pattern.

Another way to overcome cracking problems is to include some porosity in the film. This leads to a reduction of the hardness of the film, and thus lowers the piezoelectric coefficients of type e_{ij} (stress/electric field; or charge/strain) and the device performance (note that $d_{33,f}$ may be enhanced by porosity).

The aim of this section is to extend the thickness range of {100}-textured sol-gel films up to 4 µm, to analyze their microstructure, piezoelectric and dielectric properties. Poling optimization and films stresses are studied as well.

3.3.1 Structural characterization

3.3.1.1 Microstructure and texture

The deposition process has been described in chapter 2. For every micron, 4 single spins (3 with 10% lead excess + 1 with 30% lead excess) have been deposited. For example, 4 µm thick film required 64 spins (16 times (3 + 1) layers) and 16 rapid thermal annealing. Figure 3.14 shows SEM images of cross-sections and top-views of 2, 3 and 4 µm PZT 53/47 films. They show the columnar growth of the grains nucleated at the bottom electrode, and a dense and crack-free morphology. The diameter of grains increases slightly with thickness (185, 195 and 220 nm for 2, 3, and 4 µm thick films respectively).

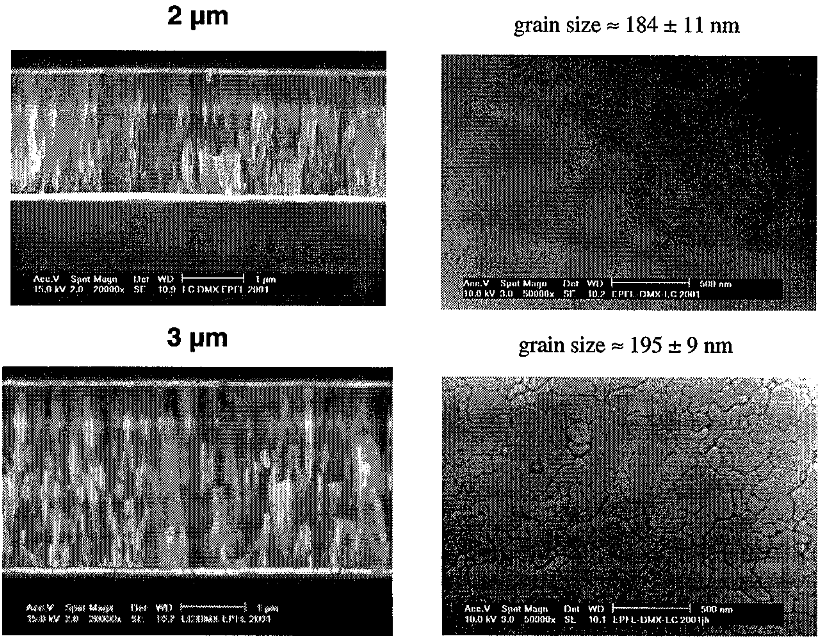

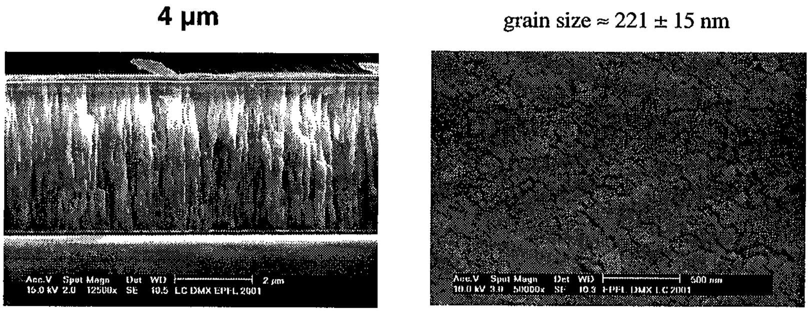

Figure 3.14: SEM images of cross-sections and top-views of 2, 3 and 4 µm thick {100}-textured PZT 53/47 films.

Figure 3.15 and 3.16 show cross-sectional TEM images of 4 µm thick PZT film. The majority of grains grew from the bottom electrode throughout the film to the top surface. The dimensions of the Pt grains initially control the PZT grain diameter. It also shows a clean interface to the Pt electrode that is free of second phases. The interruption of growth between subsequent anneals is hardly seen. Apparently, each PZT layer nucleates quasi epitaxially on the previous one. Only slight perturbations of growth are visible at the so formed crystallization interfaces.

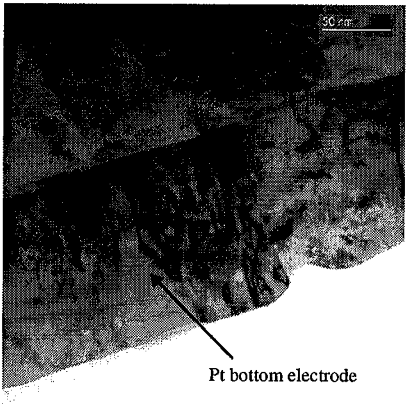

Figure 3.15: Interface between PZT {100}-textured PZT 53/47 4 µm film and the platinum bottom electrode.

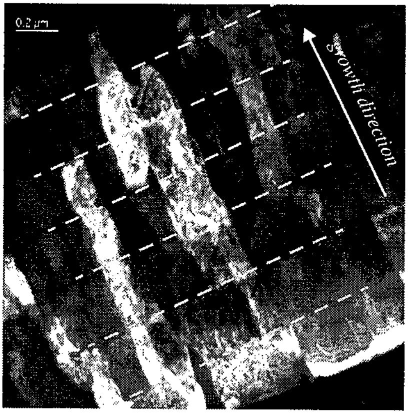

Figure 3.16: Dark Field (DF) TEM image cross-section of 4 µm thick PZT 53/47 {100}-textured film.

The films are highly {100}-textured. Figure 3.17 shows the Θ-2Θ X-ray diffractogram and the {100}-texture index of the PZT 53/47 films for the whole thickness range of 0.5 to 4 μm. A slight increase of the texture index can be observed with increasing thickness. This phenomenon is most probably linked to the fact that the mean diameter of the columnar grains is increasing with film thickness. The {100} grains exhibit a faster lateral growth than the grains of other orientations. So with time, other orientations tend to be suppressed.

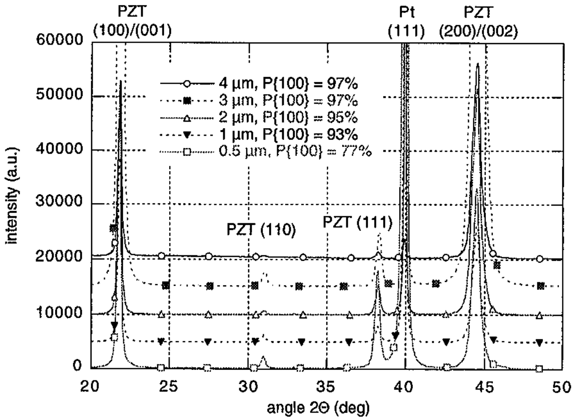

Figure 3.17: Θ-2Θ X-ray diffractogram of {100}-textured PZT 53/47 films deposited on $PbTiO_3/Pt/TiO_2/Ti/SiO_2/Si$ substrate as a function film thickness.

3.3.1.2 Film stress

Accurate knowledge of PZT film stress is of primary importance as it will drives the stress compensation and gives the limits in device design (minimal thickness of the silicon cantilever for instance). PZT films stresses of +110 MPa for 1 μm thick films, decreasing to +50 MPa for 4 μm thick films (see Figure 3.18) have been measured. These low stress values of dense and crack-free films are thought to be the result of a slow pyrolysis process. They are of the same magnitude than the stress generated by the thermal mismatch between the PZT and the silicon substrate. Taking thermal expansion coefficient of 4 ppm/°K for silicon and 8 ppm/°K for PZT, thermal stress of + 182 MPa is obtained for a crystallization temperature of 650°C. The decrease of the stress as the film thickness increases may be explained by elastic relaxation that is more probable in thick films.

During poling, it has been observed that the re-orientation of c-domains along the poling field (z-axis) increases further the stress to more tensile values. For 1 μm poled films, the stress increases by +70 MPa and amount to +180 MPa. These values were well reproducible and can be taken into account for device design.

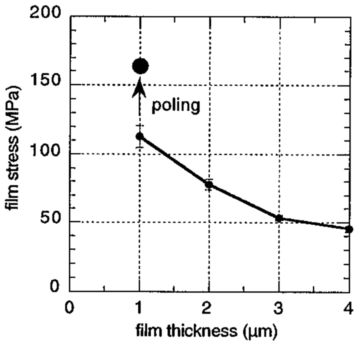

Figure 3.18: Mechanical stress of PZT 53/47 {100}-textured films as a function of film thickness.

3.3.1.3 Film composition

Cross-sectional TEM image represented in Figure 3.16 shows that the majority of grains grew from the bottom electrode throughout the film to the top surface. Apparently, the subsequent PZT layer nucleates quasi epitaxially on the previous one. Only slight perturbations of growth are visible at the so formed crystallization interfaces. The latter are even better seen at wet etched sections (see Figure 3.19).

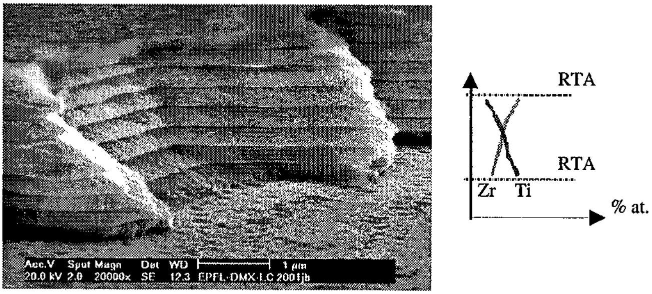

Figure 3.19: SEM image of side-view of 2 μm {100}-textured PZT 53/47 film wet-etched in HCl/HF solution.

However, these steps are not due to interface imperfections but to compositional gradients as revealed by EDX analysis (TEM facility). Above the crystallization interface (first single spin with 10% Pb excess solution), the composition is Ti rich (PZT 44/56 (± 2%)). In the center of the layer the composition amounts to 52/48 and is then gradually changing to Zr rich on the top of the crystallized layer (PZT 65/35) (see Figure 3.21). This composition gradient reflects the fact that the activation energy for nucleation is smaller and the free energy of formation is more negative (more exothermic) for Ti rich compounds [17].

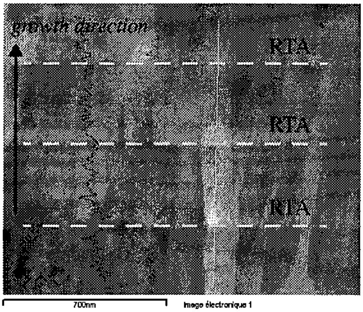

Figure 3.20: TEM image of cross-section of PZT layers separated by Rapid Thermal Annealing (RTA).

Measured compositions at the interface
Zr / Ti / Pb / O, PZT Zr/Ti

Above the interface: Ti-rich
9.7 / 12.3 / 17 / 61 = **PZT 44/56**
Below the interface: Zr-rich
13.6 / 7.3 / 18.6 / 60.5 = **PZT 65/35**
Middle of the layer:
11.1 / 10.2 / 18 / 60.7 = **PZT 52/48**

Error: ± 2%, in atomic percent, total = 100%

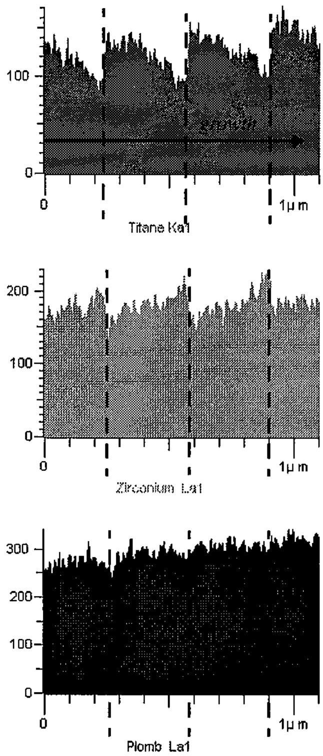

Figure 3.21: Ti, Zr and Pb EDX chemical analysis profile, arbitrary units. Growth direction is from left to right.

3.3.2 Piezoelectric properties

The evolution of $e_{31,f}$ as a function of film thickness has been determined for the composition yielding the best results at 1 μm (PZT 53/47). The results are summarized in Figure 3.22. Transverse piezoelectric coefficients of **-12 to -13 C/m²** have been achieved for the whole thickness range. It has been observed that the poling field needs to be adjusted to the thickness. Thicker films tend to degrade at lower fields, meaning that the break-down field is lower for thicker films (instantaneous break-down occurs at 500 kV/cm for 1 μm thick films and 300 kV/cm for 2 μm thick films). On the other hand, thicker films need fewer field for optimal poling.

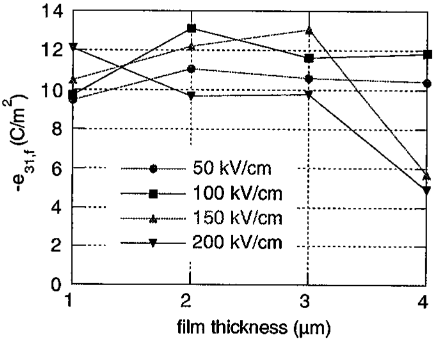

Figure 3.22: Transverse piezoelectric coefficient of {100}-textured PZT 53/47 thin films as a function of film thickness. Poling conditions: 150°C, 10 min.

To complete the description of piezoelectric properties, the longitudinal coefficients have been evaluated as well and are presented in Figure 3.23 as a function of film thickness. A typical loop as obtained by measuring the small signal $d_{33,f}$ as a function of a superimposed dc field is given in Figure 3.24. The loop was taken after hot poling with a positive field. This results in an asymmetry: $d_{33,f}$ in the positive direction is larger.

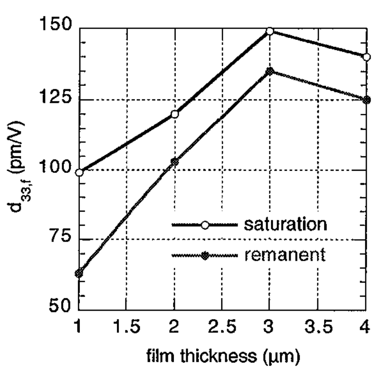

Figure 3.23: Longitudinal piezoelectric coefficient $d_{33,f}$ as a function of PZT 53/47 {100}-textured film thickness.

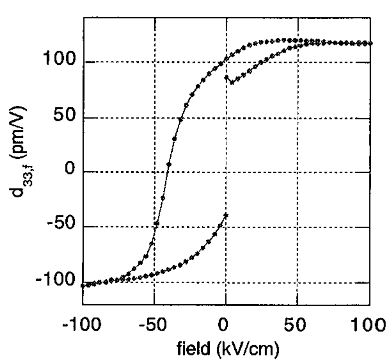

Figure 3.24: The clamped longitudinal piezoelectric coefficient $d_{33,f}$ loop as a function of dc electric field for a 2 μm thick positively poled PZT 53/47 {100} film.

In Figure 3.25, the results of our {100}-textured thin films are summarized in a $d_{33,f}$ vs. $e_{31,f}$ plot and compared to literature data of PZT bulk ceramics (pure PZT ceramics from Berlincourt) and modern optimized (doped) ceramics, 3203 HD from Motorola. It turned out that thin film data are better than the first, but still considerably lower than the latter data. Unfortunately there are no single crystal data for PZT that would allow the derivation of the theoretical properties of textured films. Approximate values for the electrostrictive constants Q_{ij} and c-domain polarization have been derived from poled bulk ceramics [18], [19], [20]. The $e_{31,f}$ coefficient of a c-domain clamped on a plane is derived from the standard Landau-Ginzburg-Devonshire [18] free energy as follows:

$$e_{31,f} = 2 \cdot Q_{12} \cdot \frac{P_3}{s_{11}^E + s_{12}^E} \cdot \varepsilon_0 \varepsilon_{33} \tag{3.8}$$

Taking the Q_{12}, P_3 (0.5 C/m^2), and lattice dielectric constant ε_{33} (382) from references [19], [20], and the elastic coefficients from [12], a value of -18.7 C/m^2 is calculated for a PZT 50/50 tetragonal (001) c-domain. Now, we can replace the maximal polarization by the effectively measured one, 0.2 to 0.25 after poling. This would yield an $e_{31,f}$ of -7.5 to -9.3 C/m^2. This can be considered as satisfying agreement, since the domain configuration is more complex and ferroelastic domains may contribute as well directly to the charge when domain walls move due to applied strains. It can be seen that the $e_{31,f}$ of our films are superior to the $e_{31,f}$ derived from classical PZT ceramics data (Berlincourt [12]) as –9.6 C/m^2 and to the $e_{31,f}$ of 1 μm PZT 45/55 {111}-textured thin film as -8.5 C/m^2. Surprisingly, the $e_{31,f}$ coefficients are almost constant for all the thickness range but not the $d_{33,f}$. The latter coefficient is increasing to values comparable to the $d_{33,f}$ of optimized PZT 3203 HD from Motorola. A possible explanation is the reduction of domains and domain walls as the grain size is increasing with the film thickness. {111} residual orientation is also decreasing as {100} grains are growing laterally to form larger grains (see Figure 3.14 and Figure 3.17).

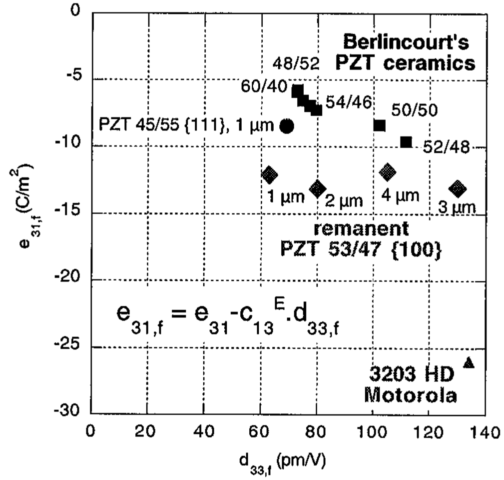

Figure 3.25: Comparison of {100}-textured PZT 53/47 1-4 μm thick films with Berlincourt's PZT bulk ceramics [12] and doped PZT 3203 HD from Motorola [21].

Taking $e_{31,f}$ = -12.5 C/m^2 and using elastic compliance of PZT bulk ceramics, d_{31} coefficient of -110 pm/V has been calculated. Some evidence shows that this improvement in $e_{31,f}$ is related to the degree of texture. Figure 3.26 suggests that a trend exists between the texture index and the $e_{31,f}$ coefficient. Note that the $e_{31,f}$ of the 4 μm film is slightly lower due to a possible degradation during the polarization of the film. Figure 3.27 summarizes the $e_{31,f}$ and $d_{33,f}$ values as a function of film thickness.

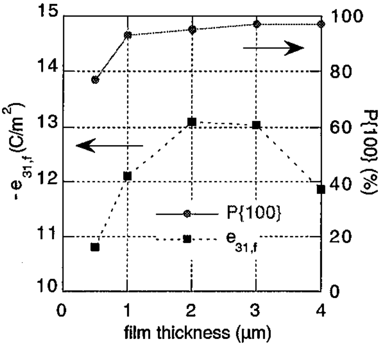

Figure 3.26: Transverse piezoelectric coefficient $e_{31,f}$ and {100} texture index as a function of PZT film thickness.

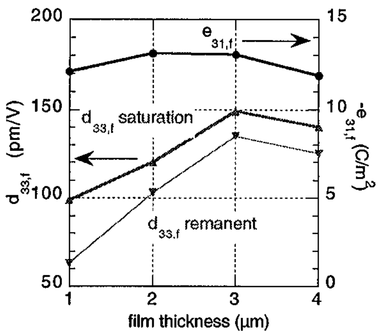

Figure 3.27: Transverse and longitudinal piezoelectric coefficients $e_{31,f}$ and $d_{33,f}$ as a function of PZT film thickness.

Table 3.4 compares typical piezoelectric properties of {100}-textured PZT 53/47 2 µm film with values of bulk ceramics given in the literature.

Table 3.4: Comparison of {100}-textured PZT 53/47 2 µm thin film properties with reference bulk PZT.

Parameters	**Film {100} remanent (this study)**	**Film {100} 50 kV/cm (this study)**	PZT 52/48 Berlincourt [12]	PZT Motorola 3203 HD [21]	PZT 50/50 {100} c-domain using Haun's parameters [20], [19]
$\varepsilon_{33,f}$	**1175**	**940**	980	1600	-
$e_{31,f}$ (C/m^2)	**- 12**	**- 14**	- 10	- 26	- 18.7
$d_{33,f}$ (pm/V)	**80**	**120**	107	140	196

Comparable longitudinal coefficients $d_{33,f}$ than doped PZT 3203 HD have been obtained with 4 µm thin film. However, the transverse piezoelectric coefficient of 4 µm films remains about 2 times lower. The {100} texturation improved the piezoelectric properties by 50% compared to existing {111} films. It also exhibited better properties than undoped bulk ceramics.

3.3.3 Dielectric properties

The dielectric permittivity and the loss factor of the films have been characterized in the whole range of thickness. Figure 3.28 shows the dielectric permittivity measured at low voltage (0.5 V, 1 kHz) as a function of film thickness and poling field. High dielectric permittivities of 1000 to 1200 have been obtained. It can be also observed that thicker films tend to degrade at lower poling field. For 3 and 4 μm films, poling fields above 100 kV/cm lead to film degradation as illustrated by the drop of the permittivity.

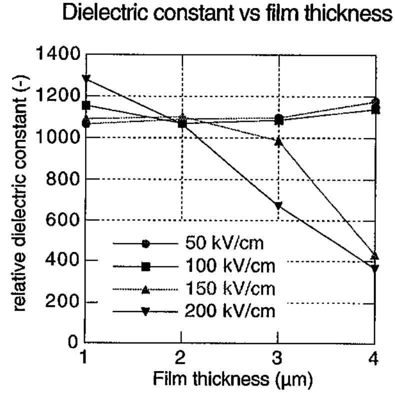

Figure 3.28: Dielectric permittivity of {100}-textured PZT 53/47 as a function of film thickness and poling field. Poling conditions = 150°C, 10 min

Figure 3.29 shows the dielectric loss of PZT 53/47 {100}-textured thin films measured at constant AC field (0.1 kV/cm and 1 kV/cm). As the film thickness increases, the dielectric loss decreases from 2.5 to 1.5%, showing the reducing influence of the interface between the PZT film and the bottom electrode. However, these values are still one order of magnitude larger than in bulk ceramics (0.2% for PZT 52/48) given by Berlincourt [12].

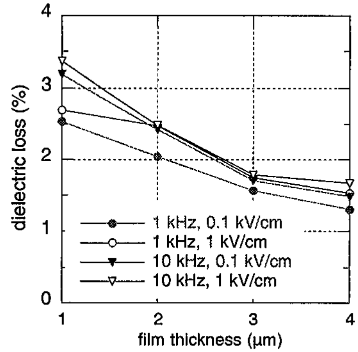

Figure 3.29: Dielectric loss of PZT 53/47 {100}-textured films as a function of film thickness measured at constant AC field (0.1 kV/cm and 1 kV/cm), frequency = 1 kHz and 10 kHz.

In operating devices such as transducers, the working field has a great influence on the dielectric loss. Figure 3.30 shows the variation of the loss factor of 2 μm {100}-textured PZT 53/47 film as a function of the working AC field and frequency. At 1 kHz, losses are almost constant below 0.5 kV/cm but increase dramatically above 5 kV/cm due to the onset of hysteretic effect.

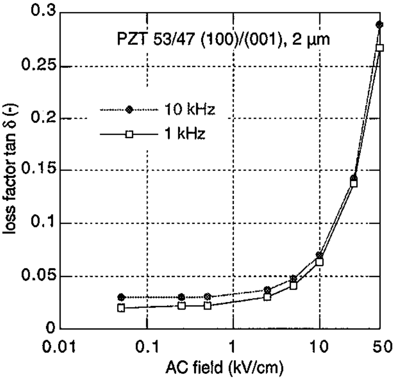

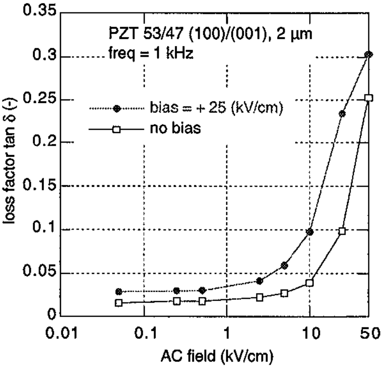

Figure 3.30: Dielectric loss factor as a function of AC field at 1 and 10 kHz

Figure 3.31: Dielectric loss factor as a function of AC field under zero and +25 kV/cm DC bias. Measurement frequency: 1 kHz

Figure 3.32 compares the dielectric loss of 2 μm PZT 53/47 {100}-textured thin film with commercial bulk ceramics (hard PZT 4D and soft PZT 5A from [22]). It shows that the behavior of our film is closer to the one of hard materials. However, at low AC field, the dielectric loss in thin films is larger (3% compared to 0.4 % for PZT 4D). For the 4 μm film, a dielectric loss of 1.6% has been measured at low field. This value is compatible with the one of PZT 5A but still 4 times larger than PZT 4D. Influence of backswitching, which is stronger in thin films than in bulk ceramics might explain the difference.

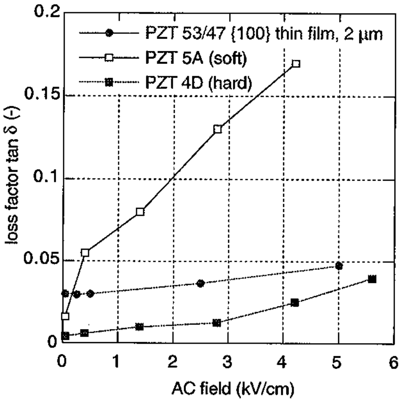

Figure 3.32: Comparison of dielectric loss tan δ of PZT 53/47 {100} 2 μm film and PZT bulk ceramics 5A and 4D (data from [22])

3.4 AGING OF TRANSVERSE PIEZOELECTRIC COEFFICIENT

3.4.1 Introduction

The aging of the piezoelectric properties (the change of $e_{31,f}$ with time or working voltage conditions) is a major issue when device operation is considered. In {100} tetragonal films, the maximum useful polarization is given by the c-domains, where the c-axis is perpendicular to the film plane. The piezoelectric properties of the films are directly related to the population and the structure of c-domains. The origin of aging can be related to two possible factors: (a) reduction of the population of c-domains (backswitching of 90° domains) and (b) depolarization of the film. As the first mechanism is related to extrinsic contributions (stabilization of the domains structure by defect [23]), the second results in a decrease of the intrinsic contribution which is proportional to the difference between the fraction of grains that are positively or negatively oriented. In PZT thin films, it turns out that the second mechanism is responsible for the aging of the piezoelectric properties rather than the suppression of domain walls motion [24]. The piezoelectric coefficient is directly related to the polarization of the film i.e. to the switching of ferroelectric domains along the poling axis. Figure 3.33 shows the two different switching processes that can be considered:

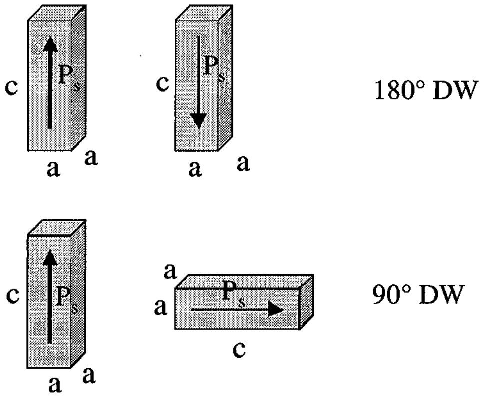

Figure 3.33: Switching of 90° and 180° ferroelectric domains and their consequence on induced strain.

Whereas the switching of 180° domains has no influence on the strain, backswitching of 90° domains modify the strain in the films. Kimura [25] measured the tetragonal distortion of c-domains in fatigued PZT thin films by x-ray synchrotron diffraction on (400) and (004) pattern of PZT. They found that tetragonal distortion of c-domains was closely related to the fatigue phenomenon. In this study, we measured directly the aging of the effective transverse piezoelectric coefficient $e_{31,f}$. Three cases of figure have been considered. First, the time aging is defined by the loss of the piezoelectric response as a function of time due to the depolarization of the film. This case is typical for sensors where no dc bias is applied during operation. Second, the unipolar aging is defined by the change of the transverse piezoelectric coefficient as a function of unipolar working voltage $V_0(1+\sin\omega t)$. The third case is so-called bi-polar aging. The working voltage has no dc bias and is simply defined by $V_0 \sin \omega t$.

Figure 3.34 shows the time aging of the transverse piezoelectric coefficient $e_{31,f}$ of poled 1 µm 53/47 {100}-textured PZT film. Initial value, about 15 min after poling is $e_{31,f} = -12.5$ C/m^2. A decrease (in absolute value) of the transverse piezoelectric coefficient of about - 4 %/decade has been measured, indicating that after 100'000 h (or 10 years), the $e_{31,f}$ should be in the order of -10 C/m^2. This value is similar to the one obtained by Shepard on d_{31} of PZT 52/48 sol-gel films [6].

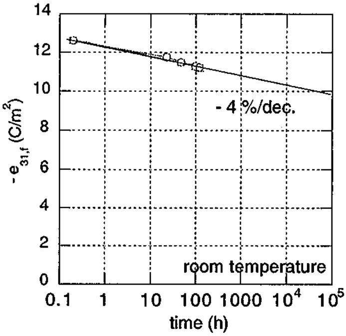

Figure 3.34: Time aging of the transverse piezoelectric coefficient $e_{31,f}$ of {100}-textured 1 μm PZT 53/47 film. Initial poling: 250 kV/cm, 10 min, 150°C

The aging of {100}-textured PZT 53/47 1 μm thin film under unipolar and bipolar electrical field are represented in Figure 3.35 and 3.36. The initial poling field was +250 kV/cm and the aging frequency was 10 kHz.

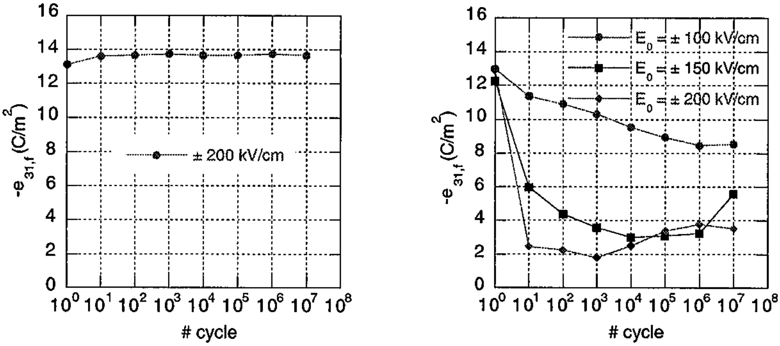

Figure 3.35: Unipolar aging: V_0 (1+sin ωt) with V_0 = 200 kV/cm of poled {100}-textured PZT 53/47 film (1 μm).

Figure 3.36: Bipolar aging: E_0 sin ωt with E_0 = 100, 150 and 200 kV/cm of poled {100}-textured PZT 53/47 film (1 μm).

Under unipolar field conditions, the transverse piezoelectric coefficient $e_{31,f}$ is slightly improved during the first three decades of cycling. Then a constant value is reached. Under bipolar field conditions, the aging behavior depends strongly of the magnitude of the electrical field. As 200 kV/cm destroy almost immediately all the piezoelectricity of the film, 100 kV/cm yields smooth decrease of the properties. Interestingly is the recovery of the properties occurring shortly after the minimum of the piezoelectric coefficient has been reached. This phenomenon might be related to the increase of frozen domains oriented along the polarization axis. However, the piezoelectric coefficient does not recover its initial value.

The time aging of the transverse piezoelectric properties of {100}-textured thin films has shown a slight reduction of the $e_{31,f}$ coefficient of about 4%/dec, similar to other results measured on sol-gel films. As no modification of the piezoelectric activity has been measured during unipolar aging, a strong depolarization occurs in case of bi-polar working field. Some restoring of the properties have been observed, maybe due to frozen domains oriented along the polarization axis.

3.5 SUMMARY

Dense and crack-free PZT thin films have been deposited on platinized silicon substrates by chemical solution deposition (CSD). Highly {100}-textured films (P{100} > 95%) were obtained by seeding the growth with 10 nm of {100}-textured $PbTiO_3$ deposited by sputtering. Due to faster lateral growth of {100} grains over {111}, the texture index of {100} orientation was found to increase with film thickness, from 77% for 0.5 μm film to more than 97% for 4 μm film. TEM studies have revealed that the composition of the individual crystallized layers was graded with amplitude of ± 20 % around the 53/47 MPB composition due to the difference of growth kinetics between Ti-rich and Zr-rich compounds.

On 1 μm film, the optimal composition with respect to the transverse piezoelectric properties was found at the 53/47 morphotropic phase boundary with effective transverse piezoelectric coefficient $e_{31,f}$ of -12 ± 0.3 C/m^2. This value has been measured by direct and converse effect. By applying another method (wafer flexure method), a value of $e_{31,f} = -12.8$ C/m^2 has been obtained by another laboratory. Compared to {111}-textured films where the maximum was situated at 45/55, our {100} films exhibit superior properties (about 50% higher). Similar values (-12 to -13 C/m^2) have been obtained in the whole investigated thickness range (1 - 4 μm).

The comparison of $e_{31,f}$ and $d_{33,f}$ as a function of film thickness with bulk ceramics data has shown interesting behavior. As the transverse piezoelectric coefficient did not vary significantly with thickness, the longitudinal constant $d_{33,f}$ increased considerably. Compared to optimized and doped hard PZT (3203 HD, Motorola), the $e_{31,f}$ coefficient are about two times lower but the $d_{33,f}$ coefficients are approximately the same.

The dielectric losses of our films have been also studied. Important reduction of the loss factor has been measured as the film thickness increases, showing a reduced influence of the interface with the electrodes. For 4 μm film, dielectric loss of 1.6% have been measured at low field. Such value is similar to the one of a soft PZT 5A ceramics but still 4 times higher than the one of a hard PZT (4D). Effect of backswitching, which is stronger in thin film may explain the difference. Above 5 kV/cm, significant increase of the dielectric loss is observed due to the onset of the hysteretic effect.

The piezoelectric aging under zero, unipolar and bipolar electrical field has been measured to predict the life-time of working devices. Slight aging of about -4%/decade has been measured for the time dependence of the transverse piezoelectric coefficient. 10 years after the initial poling (250 kV/cm, 10 min, 150°C), $e_{31,f}$ of -10 C/m^2 is expected. Whereas aging under AC unipolar field improve slightly the piezoelectric coefficient (increasing the film polarization), bi-polar excitation destroy the polarization state rapidly, depending of the amplitude of the electrical field.

In this study, it has been demonstrated that {100}-textured PZT 53/47 thin films are so far the best performing films that have been integrated on silicon for devices applications. They are to date the best solution for piezoelectric MEMS, in particular for transducers and actuators. It can be thought that further improvement of the piezoelectric properties is still possible (maybe a factor 2 in $e_{31,f}$) by doping. For example 2 % Nb or La will replace partially oxygen vacancies and thus, should increase the mobility of domains walls and enhance further the piezoelectric properties.

3.6 REFERENCES

1. Muralt, P., et al., *In-plane Piezoelectric coefficient of PZT Thin Films as a Function of Composition.* Ferroelectrics, 1999. **224**: p. 235-242.
2. Muralt, P., *Piezoelectric thin films for MEMS.* Integrated Ferroelectrics, 1997. **17**: p. 297-307.
3. Kwok, C.K. and S.B. Desu, *Low Temperature perovskite formation of lead zirconate*

titanate thin films by a seeding process. J. Mater. Res., 1993. **8**(2): p. 339-344.

4. Shepard, J.F., P.J. Moses, and S. Troiler-McKinstry, *The wafer flexure technique for the determination of the transferse piezoelectric coefficient (d31) of PZT thin films.* Sensors and Actuators A, 1998. **71**: p. 133-138.
5. Muralt, P., et al., *Piezoelectric actuation of PZT thin-film diaphragms at static and resonant conditions.* Sensors and Actuators A, 1996. **53**: p. 398-404.
6. Shepard, J.F., et al., *Characterization and aging response of the d_{31} peizoelectric coefficient of lead zirconate titanate thin films.* J. Appl. Phys., 1999. **85**(9): p. 6711-6716.
7. Du, X.-H., U. Belegundu, and K. Uchino, *Crystal orientation dependence of piezoelectric properties in lead zirconate titanate: theoretical expectation for thin films.* Jpn. J. Appl. Phys., 1997. **36**(9A): p. 5580-5587.
8. Du, X.-H., et al., *Crystal orientation dependence of piezoelectric properties of lead zirconate titanate near the morphotropic phase boundary.* Appl. Phys. Lett., 1998. **72**(19): p. 2421-2423.
9. Gardeniers, J.G.E., et al., *Direct measurement of piezoelectric properties of sol-gel PZT films.* Journal of the Korean Physical Society, 1998. **32**: p. S1573-77.
10. Tuchiya, T., et al., *Preparation and properties of piezoelectric lead zirconate thin film for microsensors and microactuators by sol-gel processing.* Journal of the Ceramic Society of Japan, Int. Edition, 1996. **104-156**: p. 159-163.
11. Jaffe, B., W.R. Cook, and H. Jaffe, *Piezoelectric Ceramics.* 1971, London: Academic Press.
12. Berlincourt, D.A., C. Cmolik, and H. Jaffe. *Piezoelectric properties of polycrystalline lead titanate zirconate compositions.* in *Proceedings of IRE48.* 1960. New-York.
13. Ikeda, T., *Fundamentals of piezoelectricity.* 1990, Oxford: Oxford University Press.
14. Muralt, P., et al., *Fabrication and characterization of PZT thin film vibrators for micromotors.* Sensors and Actuators A, 1995. **48**: p. 157-165.
15. Bernstein, J.J., et al., *Micromachined high frequency ferroelectric sonar transducers.* IEEE Tran. UFFC, 1997. **44**(5): p. 960-969.
16. Brooks, K.G., et al. *Sol-Gel deposition of PZT thin films on ceramic ZrO_2 substrates.* in *ISAF 1996, International Symposium on Applications on Ferroelectrics.* 1996.
17. Peng, C.H. and S.B. Desu, *Investigation of structure development in MOD PZT films by an optical method.* Ferroelectric thin films II, 1992: p. 335-340.
18. Haun, M.J., et al., *Thermodynamic theory of the lead zirconate solid solution system, part I: Phenomenology.* Ferroelectrics, 1989. **99**: p. 13-25.

19. Haun, M.J., et al., *Thermodynamic theory of the lead zirconate-titanate solid solution system, part III: Curie constant and sixth-order polarization interaction dielectric stiffness coefficients.* Ferroelectrics, 1989. **99**: p. 45-54.
20. Haun, M.J., et al., *Thermodynamic theory of the lead zirconate-titanate solid solution system, part V: Theoretical calculations.* Ferroelectrics, 1989. **99**: p. 63-86.
21. Sherrit, S., H.D. Wiederick, and B.K. Mukherjee, *A complete characterization of the piezoelectric, dielectric and elastic properties of Motorola PZT 3203 HD including losses and dispersion.* Proc. SPIE, 1997. **3037**: p. 158-169.
22. Gonnard, P. and L. Petit, *Non linear effects in piezoelectric materials.* Buletin de la Sociedad Espanola de Ceramica y Vidrio, 2002.
23. Schulze, W.A. and K. Ogino, *Review of literature on aging of dielectrics.* Ferroelectrics, 1988. **87**: p. 361-377.
24. Kholkin, A.L., et al., *Piezoelectric and dielectric aging in PZT thin films and bulk ceramics.* Integrated Ferroelectrics, 1997. **15**: p. 317-324.
25. Kimura, S., I. Koichi, and T. Tatsumi, *Tetragonal distorsion of c domains in fatigued PZT thin films determined by x-ray diffraction measurements with highly brillant synchrotron radiation.* Appl. Phys. Lett., 2002. **80**(13): p. 2365-2367.

CHAPTER 4

MICROFABRICATION AND ELECTROMECHANICAL PROPERTIES OF PZT/SILICON MICROCANTILEVERS

4.1 MICROFABRICATION OF PIEZOELECTRIC MEMS

4.1.1 Introduction

Silicon micromachining, which refers to fashioning microscopic mechanical parts out of a silicon substrate, has emerged as an extension of IC's fabrication technology [1]. During the last 20 years, it has been successfully employed to produce a variety of mechanical microstructures of a great diversity including beams, diaphragms, grooves, orifices, sealed cavities, pyramids and needles and has driven the rapid progress of Micro-Electro-Mechanical-Systems (MEMS). However, silicon structures represent only a structural element defining most of the mechanical properties of the devices and, usually, functionality still need to be added. This is the role of functional materials such as piezoelectric thin films to provide a direct transformation between a driving signal or read-out signal on the one hand, and a sensor or actuator parameter on the other hand. The basics of silicon MEMS microfabrication such as photolithography, pattern transfer with dry and wet etching techniques and common thin films deposition (SiO_2, Si_3N_4, poly-Si, Al, Cr, Ni, Au) have been described in the book of Madou [2] and no further details will be given here. Despite many demonstrators, the microfabrication of piezoelectric MEMS still suffers from inadequate micromachining processes and very few references have been published on the subject [3], [4], [5] (the two latter issuing partially from the present research). The integration of piezoelectric thin films and "exotic materials" used as diffusion barrier (TiO_2), electrodes (Pt) or seed layers ($PbTiO_3$) require new and specific micromachining processes that are not available in standard IC's fabs.

The dry etching of PZT and platinum thin films is, unfortunately, not a trivial task as the volatility of their reactive by-products is rather low. There is thus a need for new micromachining processes for PZT and Pt films to afford micro scale resolution, reasonable etching rate and to find a process flow that avoid any degradation of the PZT film functionality.

The aims of this chapter are to provide micromachining tools (dry etching methods) to produce piezoelectric MEMS with micro scale features, to stress key issues such as stress compensation, process flow, advanced SOI substrates and to demonstrate the fabrication and the electromechanical properties of PZT/Si microbeams.

4.1.2 PZT/Si planar structures: a playground for piezoelectric MEMS

Most of piezoelectric devices are based on laminated PZT/Si planar structures, which are defined as a flexible supporting silicon structure (5 - 20 µm thick) coated with a piezoelectric thin film (see Figure 4.1). Depending on applications, various geometry and clamping conditions can be considered: from the very simple cantilever to a fully clamped membrane or any partially clamped diaphragms (membrane fixed by four small bridges for instance). The electromechanical coupling is provided by the transverse piezoelectric coefficient $e_{31,f}$ (see chapter 1).

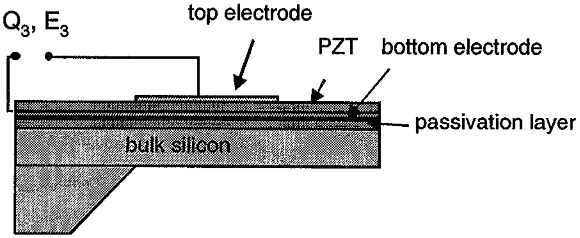

Figure 4.1: Laminated PZT/Si deflecting structure used in piezoelectric MEMS

To succeed in the microfabrication of such device, four important issues have to be addressed. First, and as demonstrated in chapter 3, the deposition of high quality PZT thin film on a wafer scale has to be solved. Second, specific micromachining methods and process flow have to be developed. Third, the mechanical stress through the structure need to be compensated to avoid any residual bending and, finally, the thickness of the supporting structure should be uniform.

Two different techniques have been used to fabricate devices based on planar PZT/Si structures. First, surface micromachining has been mainly employed to make simple accelerometers [6] (ZnO), [7] (PZT). One advantage of this method is that the poly-silicon layer can be used to define precisely the thickness of the supporting structure. But, it turned out (in particular in [7]) that the etching of the sacrificial layer (PSG) in HF often destroy the functional properties of the PZT thin film. Even with a silicon nitride encapsulation, pinholes occurred and the film was damaged. It has been also observed that the roughness of the poly-silicon layer disturbs strongly the growth of the PZT film giving thus low piezoelectric coefficients. Finally, the geometries of surface micromachined piezoelectric devices are limited by the kinetics of the lateral etching of the sacrificial layer. Beams larger than 50 μm are difficult to release in a reasonable time. The second technique is based on classical silicon bulk micromachining. Among reported devices, one can point out micromotors [8], [9] (PZT), [10] (ZnO), accelerometers, [11], [12] (PZT), audio microphone and microspeakers [13] (ZnO), 2-D scanners [14] (PZT), AFM tips [15], [16] (PZT) and ultrasonic transducers [17] (PZT). Here, the limiting factor is the uniformity of the silicon structure obtained with standard wafers.

4.1.3 Stress compensation

All films in the laminated structure exhibit a mechanical stress (tensile or compressive), which is function of materials and deposition methods. If the global residual stress is different of zero, a residual bending occurs that can reduce or even destroy the device sensitivity. Accurate knowledge of all films stresses is thus of a primary importance. Assuming a thin film stress (σ_{ι}), it induces a bending to freestanding structure. Each film (on average height h_i, thickness t_i) applies a bending moment with respect to the neutral plane (on height h_n) of the structure.

$$M = \sum_i \sigma_i t_i (h_i - h_n) = 0 \tag{4.1}$$

To obtain a zero residual bending and thus perfectly in-plane structure, the sum of all moments has to be nulled (M = 0).

The stress in piezoelectric PZT thin films depends on composition, texture, thickness and poling. Figure 4.2 shows the stress of PZT {100}-textured thin films as a function of composition for 1 μm film and as a function of thickness for PZT 53/47 films. At low Zr concentration (tetragonal film), the stress is compressive and is mostly due to the {100} orientation (c-axis in the plane). As the Zr concentration is increasing, film stresses are becoming more and more tensile (+110 MPa for PZT 53/47) due to the sol-gel process itself (shrinkage of the film during the pyrolysis). At the MPB and for thicker films, smaller film stresses have been measured and can be explained by elastic relaxation that is more probable in thick films.

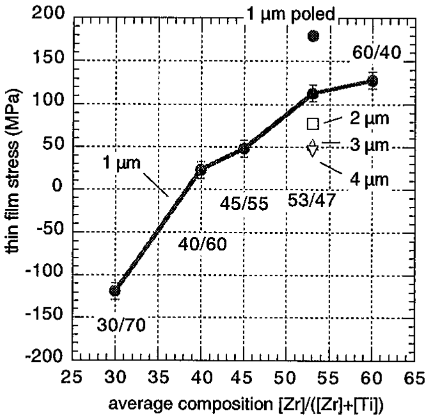

Figure 4.2: Stress of {100}-textured PZT thin films as a function of average composition and thickness.

To achieve precise stress compensation, the effect of poling has to be considered as well. Due to the re-orientation of c-domains along the poling field (z-axis), the tensile stress increases further from +110 MPa to +180 MPa for 1 µm PZT 53/47 thin film. These values were well reproducible and have been used for the compensation calculation. Table 4.1 shows that the film stresses of a laminated PZT/Si structure are all tensile except the thermal SiO_2, which is compressive (-300 MPa). Stress compensation (equation (4.1) = 0) has been achieved by adjusting the thickness of thermal SiO_2 to about 1000 nm.

Table 4.1: Typical thickness and film stress in PZT/Si deflecting structures

Materials	Deposition method	Film thickness (nm)	film stress (MPa)
thermal SiO_2	LPCVD - wet ox	set to 1000	-300 ± 5
Pt bottom electrode	PVD hot (300°C)	120	+550 ± 20
PZT 53/47 {100}	sol-gel	1100	+110 ± 10 (unpoled) +180 ± 10 (poled)
Au/Cr top electrode	evaporation	150	+280 ± 10

4.1.4 Process flow for the microfabrication of PZT/Si planar structures

The microfabrication of planar PZT/Si deflecting structure is, like any IC's classic process flow, based on several iterations of film deposition - photolithography - etching as depicted by Figure 4.3. In the process, many materials such as platinum, TiO_2/Ti adhesion layer, thermal SiO_2, PZT films as well as electrodes (gold or platinum) are involved.

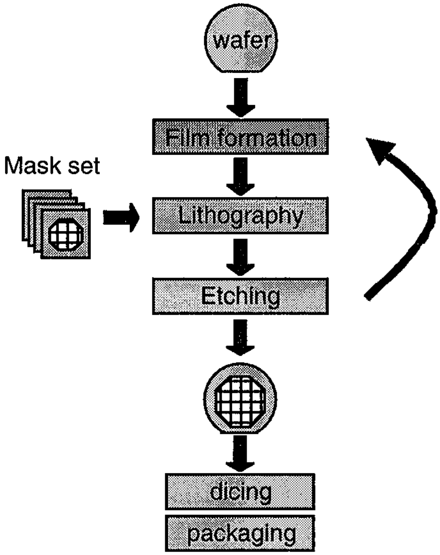

Figure 4.3: Major processing steps in IC or MEMS microfabrication

Figure 4.4 shows the generic process flow for the microfabrication of planar PZT/Si deflecting structures (in this particular example, a simple cantilever). Starting with the deposition of the piezoelectric thin film by sol-gel CSD (A), top electrode is deposited and patterned by lift-off (Au/Cr) or by plasma dry etching (platinum). To give access to the bottom electrode, vias are opened through the PZT film by wet or dry etching (C). The frontside shape of the structure (the gap surrounding the cantilever) is then patterned through the PZT/Pt/SiO_2 stack (D) using three different processes: PZT dry or wet etching, platinum dry etching and finally SiO_2 dry or wet etching.

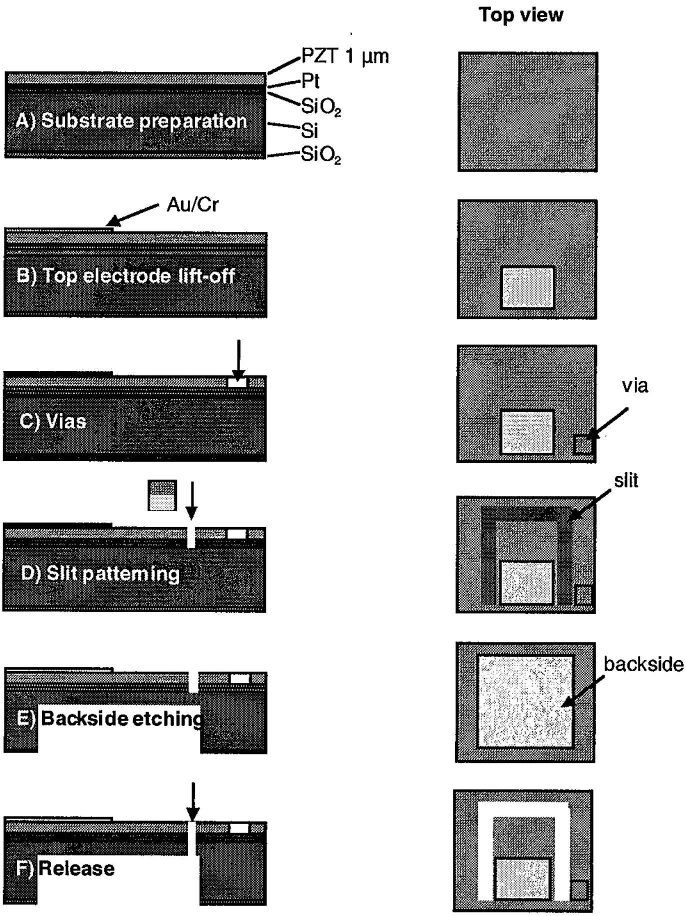

Figure 4.4: Generic process flow for the microfabrication of PZT/Si cantilever (cross section and top view)

Bulk silicon micromachining from the wafer's backside (E) is then performed to define the thickness of the structure (usually between 5 and 20 μm). The process is either dry (deep silicon etching in a plasma reactor) or wet in KOH. The definition of precise and uniform silicon thickness (for example: 20 ± 1 μm thick silicon cantilever out of a 390 μm thick wafer) is of primary importance as the devices sensitivity is usually function of $1/\text{thickness}^2$. Accurate etching time measurement, etch-stop on n-doped epi layer [18] or the use of Silicon-On-Insulator (SOI) substrate are possible solutions.

Finally, the deflecting structures are released (F) by deep silicon etching (dry) from the frontside. After the whole microfabrication sequence, the functionality of the piezoelectric thin film was fully preserved. Transverse piezoelectric coefficient $e_{31,\ f} = -12\ C/m^2$, dielectric properties $\varepsilon = 1100$ and $\tan\delta = 0.03$ have been measured on test samples with 1 µm PZT 53/47 {100}-textured thin film. The six micromachining steps of this process flow use many individual patterning and deposition processes. Some of them are of a primary importance in piezoelectric MEMS microfabrication and will be developed in what follow.

4.2 SELECTED PROCESS ISSUES IN PIEZOELECTRIC MEMS FABRICATION

PZT piezoelectric MEMS microfabrication requires many different processes such as top electrode deposition, dry etching of PZT and its electrodes as well as silicon bulk micromachining. In this section, only four relevant topics that are specific to the microfabrication of piezoelectric devices will be presented:

- Top electrodes deposition.
- Patterning of PZT film (wet and dry).
- Dry etching of platinum bottom electrodes.
- Silicon bulk micromachining (wet and dry).

Details on general issues such as photolithography or silicon thermal oxidation can be found in [2] or in the process book of the Center of Microtechnology (CMI) - EPFL [19].

4.2.1 Deposition and patterning of top electrodes

To collect the electrical charges on the PZT film, Au/Cr (100 / 10 nm) top electrodes have been deposited in Edwards Auto 306 evaporator and patterned by lift-off. Compared to platinum, Au/Cr top electrodes have two advantages. First, the patterning of Au/Cr top electrodes does not require dry etching methods, as lift-off process is very versatile and offers sufficient resolution (micron scale) for MEMS applications. Second, Au/Cr top electrodes do not need post-deposition annealing. With PVD deposited platinum, the PZT surface is damaged by the ions bombardment. Thermal annealing is then required to restore the interface [20].

4.2.2 Wet etching of PZT thin films

The wet patterning of PZT thin films is a critical topic in piezoelectric MEMS microfabrication. Despite the fact it is usually avoided because of the lack of etch control and photoresist undercut, the wet etching of PZT films remains a very versatile, fast and cheap method to open large areas (> 50 x 50 µm^2) like vias. Because of high concentrations of hydrofluoric acid (HF), most of etch recipes are not selective to SiO_2 and to the TiO_2 adhesion layer of the platinum bottom electrode. Delamination of the structure can thus occur. In term of etching rate, HCl solutions have found to be very effective and selective etchants [21]. In this thesis, we used a solution of 30 ml of concentrated HCl (47%), 70 ml of water and 5 drops of HF. At 60°C, the etching rate is about 50-100 nm/s. Figure 4.5 shows the tip of a 500 x 100 µm^2 microcantilever where the 1 µm PZT film has been patterned by wet etching. Underetching defects as large as 5-10 µm can be observed which give a masks design rule (geometry tolerance) of about 10 times the PZT thickness (Figure 4.6). Wet etching of narrow slit (width 3 - 10 µm) is thus impossible and dry etching techniques should be employed.

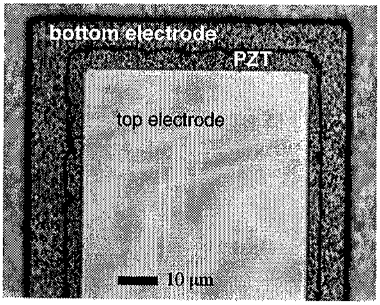

Figure 4.5: Optical image of top view of the tip of a 100x500 µm^2 PZT/Si cantilever

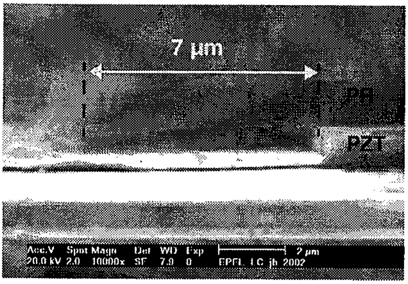

Figure 4.6: SEM image cross-section of PR/PZT after wet etching (undercut ≈ 7 µm).

4.2.3 Dry etching of PZT thin films

As the size of MEMS critical features shrank to several microns (< 10 µm), the dry etching of PZT becomes mandatory to obtain a high degree of patterned edge, smoothness and steep wall profiles. The principal requirements for a dry etching process of PZT films are:

- Selectivity with respect to the bottom electrode
- Anisotropy to define precise micron-scale geometries
- High etching rate
- Sufficient selectivity to the photoresist
- No damage to the films and no residue

Unfortunately, the dry etching of PZT films is not obvious as there is no common halogenous gas that forms volatile compounds with all three elements (Pb, Zr, Ti). The volatility of the reactive etch by-products is limited and ion bombardment is often required to help the etching process. It is thus difficult to achieve, at the same time, a high etching rate and a sufficient selectivity to the electrodes and to the photoresist (PR) mask.

Most of developed process used pure argon ion milling or Reactive Ion Etching (RIE) in simple parallel plate or inductively coupled plasma (ICP) reactor. Zeto demonstrated etch rate up to 100-250 nm/min with argon ion milling. However, sloped walls (35°-70° due to the PR instability), selectivity to the platinum bottom electrode and PR mask as well as material redeposition on the sidewalls were the limiting factors [22]. To overcome these drawbacks, Reactive Ion Etching (RIE) should be employed. Compared to ion milling, RIE offers several advantages such as more vertical walls, better selectivity with respect to the platinum electrode and less redeposition of etched material on the sidewalls.

Still from the study of Zeto, etch rates up to 100 nm/min have been achieved with monochlorotetrafluoroethane (HC_2ClF_4) etch gas and 500 W RF power in a standard parallel plate reactor. In this case, the stability of the photoresist was the limiting factor. For films thicker than 250 nm, the RF power has to be dramatically reduced down to 150 W to keep the PR removable. At such power level, the etching rate is only 13 nm/min. This example is representative of the problems occurring in RIE of PZT films. It is very difficult to find a trade-off between: reasonable PZT etch rate, PR dimensional stability and PR removability. Other studies gives similar results in term of etching rates (10-40 nm/min) in HC_2ClF_4 [23], in C_2F_6/Cl_2 [24] or in CF_4/Cl_2 [25] gases.

To overcome, at least partially, these limitations, Reactive Ion Beam Etching (RIBE) in a dual frequency ECR/RF reactor is a very smart solution that combines the best features of both methods [26]. As RIBE allows much lower working pressure than the RIE/ICP process (1-10 mPa compared to 1-10 Pa), the risk of material redeposition is reduced and the verticality of the sidewalls is improved thanks to the directionality of the bombarding ion beam. The bombardment of a reactive ion beam with gases such as SF_6, CF_4 or CCl_4 is very favorable to reduce the level of energy needed for the etching process and thus to obtain better trade-off between PR stability and etching rate.

The homemade reactor we used was based on a commercial ECR (Electron Cyclotron Resonance) ion gun from Plasmion [27] as depicted in Figure 4.7. The capacitive coupling of the substrate holder to a 13.56 MHz RF power supply contributes to the acceleration of the ions bombarding the substrate (negative bias voltage). To assure better PR stability, the substrate holder is water cooled, keeping the wafer surface at a temperature lower than 100°C.

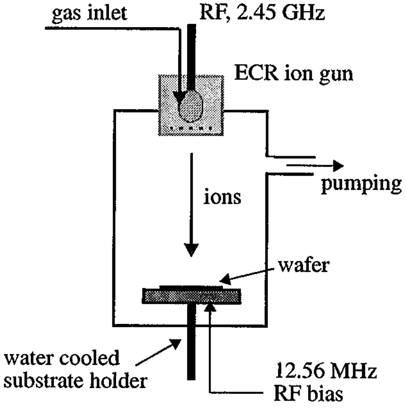

Figure 4.7: Schematic of ECR/RF ion gun

In RIE/ICP, chlorinated plasmas were generally employed because of the low melting point of metal chlorides with respect to the equivalent metal fluorides. In practice, fluorine ion bombardment (CF_4, SF_6, C_2F_6) was shown to be more selective with respect to the platinum electrodes. For RIBE of PZT films, a process with low ion energy ions (to avoid damage to photoresist and PZT surface) and low operating pressure (lower backscattering and redeposition) has been developed. Best results were obtained by mixing both chlorine and fluorine gases [28]. PR stability was improved by hard baking at 150°C.

Gases:	40% CCl_4 40% CF_4 20% Ar
Pressure	5 mPa
RF bias:	60 W
Etch rate:	max. 70 nm/min with selectivity of 0.5 to photoresist and 1.6 to Pt
Mask:	PR, Shippley 1818, 2.3 μm, hard bake 150°C, 30 min, air oven

Compared to pure RIE methods described previously, similar etch profile, PR stability and removability have been obtained with RIBE processes. However, in case of RIBE, etch rates were found to be 2 to 5 times higher. Figure 4.8 shows RIBE of PZT thin films using low working pressure (0.01 Pa) and low RF bias (60 W). In this case, steep walls and precise patterns have been obtained. But, as the working pressure is increased to 0.5 Pa and the RF bias to 120 W, the photoresist is hardly damaged and is not anymore removable (see Figure 4.9). In this case, the incident ion beam was found to be too energetic. The etching process is thus more physical than chemical. A trade-off has thus to be found between etching-rate (ions energy) and pattern definition / PR removability.

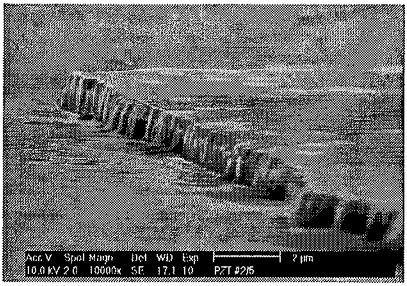

Figure 4.8: SEM side view image of patterned PZT thin film, working pressure = 0.01 Pa, 60 W RF bias, optimized etching chemistry.

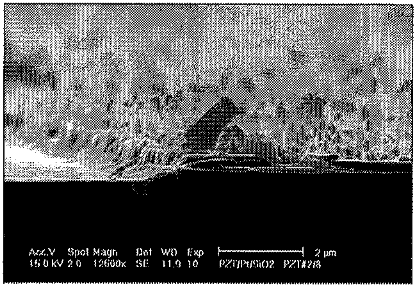

Figure 4.9: SEM side view image of patterned PZT thin film, working pressure = 0.5 Pa, 120 W RF bias, optimized etching chemistry.

4.2.4 Dry etching of platinum bottom electrode

Ferroelectric thin films for MEMS or memory applications require noble metal (platinum) or refractory metal oxide (IrO_2) electrodes. Due to their chemical inertness, the patterning of these materials is a difficult task. Like PZT, the platinum thin films can be patterned by wet etching. Aqua regia [29] or electrochemical wet etching in concentrated HCl [30] are the most known methods. However, these recipes do not work with very thin structures (< 10 µm), are very sensitive to the platinum surface contamination, are often subject to underetching of the adhesion layer and, last but to least, the HCl is a fairly good etchant for the PZT too!

For piezoelectric MEMS, dry etching techniques have to be chosen. Due to the low volatility of platinum compounds, the etching mechanisms are much more physical (ion bombardment) than chemical (formation of volatile reaction products). Here again, it is difficult to achieve a good etching selectivity with respect to the standard photoresist masks or the underlying substrate. Most of recent developed methods have used RIE/ICP (Reactive Ion Etching in Inductive Coupled Plasma) or simple ion milling but, in general, several limitations have been observed:

- Selectivity problems with PR
- SiO_2 masks are unacceptable (mask stripping in BHF would destroy the PZT)
- Residues on the sidewall are often observed and lead to fencing
- Poor patterns anisotropy with ion milling

To many aspects, the dry etching of platinum exhibits very similar problems that the PZT did. Here, chlorine based RIBE process with high-density plasma and low ions energy (to avoid damage to the photoresist) and operating at low pressure (to lower backscattering) has been developed [31], [32]. The optimal conditions were:

Gas:	CCl_4
Pressure	5 mPa
RF bias:	60 W (< 35 V)
Etch rate:	max. 60 nm/min with selectivity of 0.6 to photoresist and 0.7 to SiO_2
Mask:	PR, Shippley 1818, 2.3 µm, hard bake 150°C, 30 min, air oven

Figure 4.10 shows a SEM image cross-section of the PR/Pt/SiO_2 stack. The curved shape of the PR thin film is typical of highly physical dry etching process.

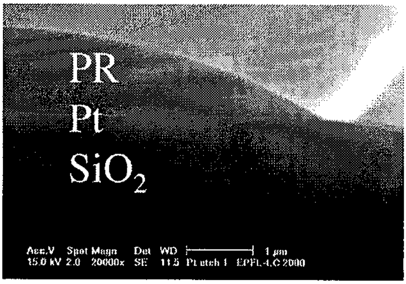

Figure 4.10: SEM image cross-section of dry etched Pt/TiO_2/SiO_2 stack

On a RIE/ICP reactor from STS, best results have been obtained with Cl_2 flow rate of 20 sccm, Ar flow rate of 70 sccm, working pressure of 1 Pa, RF coil power of 600 W and RF platen power of 150 W. The etching rate was about two times lower (32 nm/min) than the one obtained by RIBE and the selectivity was 0.35 and 0.5 with respect to PR (Shipley 1818, 2.3 µm thick) and SiO_2 respectively.

On both processes, it is obvious that the ion bombardment mainly governs the process. A tapered etch profile of PR mask and Pt is typical of physical etching. With 1 Pa, the working pressure in STS-ICP reactor is about 200 times higher than in ECR ion gun (5 mPa). However, it is still sufficiently low to avoid any redeposition of the metal on the mask sidewalls. Both Pt processes (RIBE and RIE/ICP) also offer a good selectivity to PZT (> 2) and has been successfully applied for the patterning of platinum top electrodes. The PR mask is striped in

Shipley Microposit Remover 1165 at 70°C followed by microwave plasma aching in oxygen.

4.2.5 Silicon bulk micromachining

To produce thin silicon supporting structures like beams or diaphragms, bulk silicon has to be etched in a uniform way, down to the desired thickness (usually < 20 µm). As the sensitivity of a sensor based on a cantilever is proportional to $1/(\text{silicon thickness})^2$, precise control of the silicon thickness has a direct influence on the production of uniform and homogenous devices. To control accurately the thickness of the silicon structures, many sophisticated wet-etching methods (mainly in KOH) using an etch-stop on a very well defined n-doped epi [18] or highly p-implanted silicon layers have been developed by many authors [33]. However, these methods suffer from difficult and complicated process implementation and stress non-uniformity. Despite a very low running cost, bulk silicon micromachining in KOH has important drawbacks: the shapes of the structures are restricted by the etching anisotropy (for example, V-shape trenches of 10 µm wide cannot achieve a depth larger than 7 µm due to the lower etching rate of the (111) planes), the KOH is very aggressive against the PZT and its electrodes (THE killing factor in case of broken membranes) and the uniformity is limited to about ± 10-15 µm after etching 380 µm of silicon.

Today, the silicon wet-etching in KOH tends to be replaced by plasma etching in RIE/ICP reactor. The dry and anisotropic etching process offers much more flexibility in term of design and is the solution of choice to define accurately small structure like very narrow gaps, grooves and even large surface in case of membrane patterning. The most commonly used process for deep silicon etching is the so-called Bosh process invented by Lärmer and Schilp [34]. By sequentially alternating etching steps (with SF_6 chemistry) and passivation steps (polymerization of the sidewall with C_4F_8), anisotropic etching can be obtained on feature sizes ranging from submicron to several millimeters [35]. High etching rate of 7-10 µm/min have been achieved in an Alcatel RIE/ICP 601^E reactor. Figure 4.11-A shows a SEM cross-section of a 10 x 50 µm trench. Vertical sidewalls and aspect ratio of more than 1:15 have been obtained. However, defining precise and uniform membrane thickness all over a wafer by deep silicon etching is a difficult task. It can be observed on Figure 4.11-C that the bottom of the etched cavity is not perpendicular to the sidewalls. This phenomenon can be explained by the masking effect of the walls and yields a non-uniformity of the structure thickness (thicker near the walls) that can amount to several microns. Furthermore, on the wafer level, a depth uniformity of about 3% (± 5-10 µm into 390 µm cavities) is typical with well-tuned process.

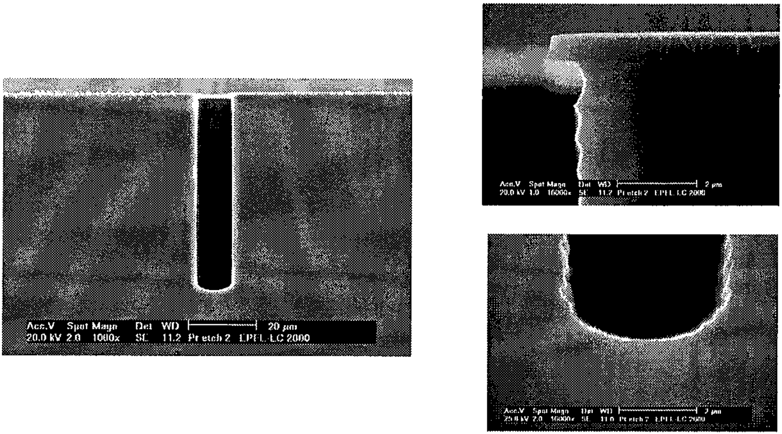

Figure 4.11: SEM images cross section of 10 x 50 µm slit etched by SF_6/C_4F_8 in silicon, AR = 15 and details of 3 µm slit (top and bottom).

To overcome, at least partially, these limitations, an etch-stop on a silicon oxide layer may offer an interesting solution.

4.2.6 Integration of PZT films on SOI and poly-SOI substrates

Silicon-on-Insulator (SOI) or poly-SOI substrates can be used to improve the uniformity of the structure thickness on the wafer scale. These two substrates use mono or polycrystalline silicon layer deposited on insulating and amorphous SiO_2 thin film (see Figure 4.12), which acts as an etch-stop during the bulk silicon micromachining.

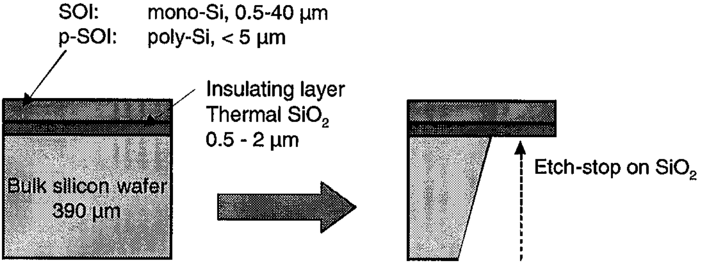

Figure 4.12: SOI and SOI-like substrates based on monocrystalline or poly-crystalline silicon device layer

In SOI wafers, the device silicon thickness (top silicon layer) is usually ranging from 0.2 μm to several hundreds of microns and the deposition of PZT films do not differ from the deposition of PZT films on classical silicon substrates. On 4 μm thick poly-silicon layer, additional processing steps are required as the roughness of the film is high (≈ 300 nm RMS). This yields loss of resolution during photolithography and PZT crystallization problems. To recover the surface state of polished silicon wafer, Chemical-Mechanical-Polishing (CMP) [36] of poly-silicon has been used (Figure 4.13). Chemical-Mechanical-Polishing of poly-silicon is a combination of chemical etching (oxidation of silicon in SiO_xH_y compounds) and the mechanical polishing using Al_2O_3 or silica particles (slurry).

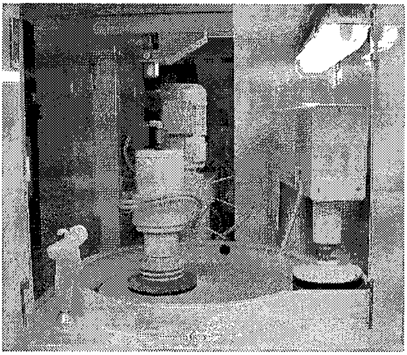

Figure 4.13: Picture of CMP equipment used for polishing thick poly-Si film.

200 nm SiO_2 passivation layer have been then deposited by PVD to insulate the platinum bottom electrode from the polysilicon layer. Finally, the platinum bottom electrode and the PZT films have been deposited with the standard process depicted in chapter 2.

Figure 4.14 show SEM images of the cross section of 1 μm PZT 53/47 {100}-textured deposited on $PbTiO_3/Pt/TiO_2/SiO_2$/poly-Si/SiO_2/Si substrate. No cracks and no delamination have been observed showing the excellent stability of the PVD SiO_2/poly-silicon structure.

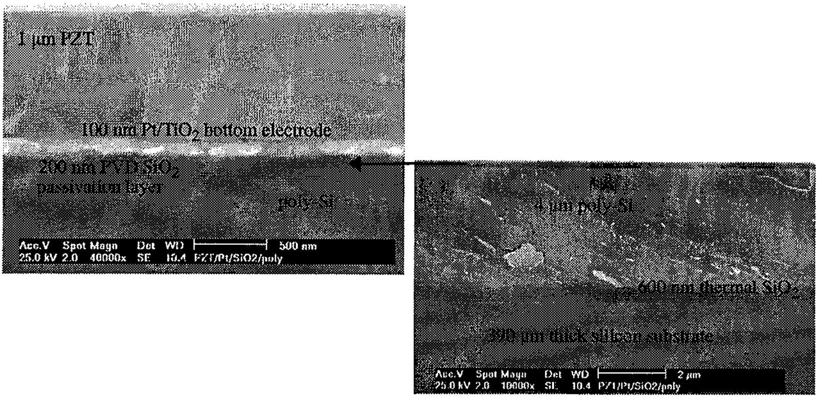

Figure 4.14: SEM images cross-section of 1 μm PZT 53/47 {100}-textured thin film deposited on CMP-polished 4 μm poly-silicon layer.

Figure 4.15 shows the Θ-2Θ XRD diffractogram of 1 μm PZT 53/47 film deposited on CMP-polished 4 μm poly-Si layer. Highly {100}-textured film with texture index of 96% has been obtained. This high texture index is the result of the CMP polishing of the poly-silicon layer.

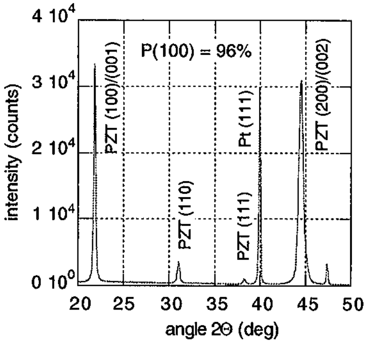

Figure 4.15: Θ-2Θ XRD diffractogram of 1 μm PZT 53/47 {100}-textured thin film deposited on $PbTiO_3/Pt/TiO_2/SiO_2$/poly-Si/SiO_2/Si substrate.

Excellent functional properties have been also obtained: $e_{31,f} = -11\ C/m^2$, $\varepsilon = 1000$, $\tan\delta = 0.05$. Integration of PZT thin films on poly-SOI substrate has been demonstrated and offers a valuable alternative to SOI wafers.

4.3 ELECTROMECHANICAL RESPONSE OF PZT/SILICON MICROCANTILEVERS

4.3.1 Bending theory of piezoelectric microbeams

The bending theory of PZT/Si piezoelectric cantilever (see Figure 4.16) has been mainly developed by two authors. In 1991, Smits [37] proposed a model with different loading conditions (uniform pressure, force or tip displacement). This model takes into account the ratio between the piezoelectric film thickness and the silicon substrate but not the effect of the lateral shrinkage due to the Poisson's effect.

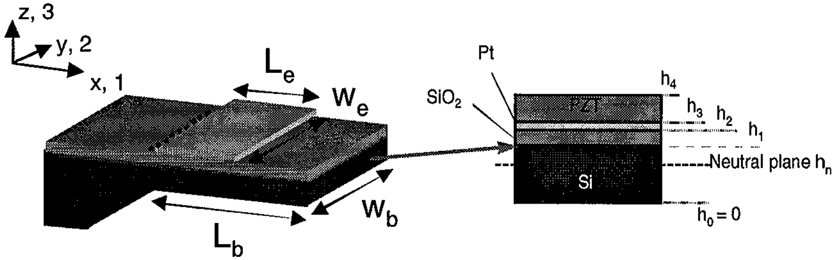

Figure 4.16: Schematic of PZT/Pt/SiO$_2$/Si microcantilever with the corresponding multilayer cross-section.

More recently, Gardeniers [38] published a model where the lateral deformation (Poisson's effect) was introduced as well as the dimension of the top electrode. However, it was restricted to thick substrates (i.e. $h_{Si} >> h_p$). This later model has been found to be very suitable to describe the bending of $e_{31,f}$ test samples in chapter 3. However, $e_{31,f}$ test samples are not similar to microbeams as their dimensions are much larger ($L = 9.5$ mm, $w_b = 1.5$ mm and $h_{Si} = 390$ μm).

The aim of this section is to evaluate upon what extent the models of Smits and Gardemiers may be applied in micromachined PZT/Si structures with typical dimensions of: length: $L = 500 - 1000$ μm, width: $w_b = 100 - 1000$ μm and silicon thickness: $h_{Si} = 5 - 50$ μm.

4.3.1.1 The model of Smits

Smits [37] expressed the vertical deflection $\delta(L)$ at the tip of a piezoelectric heteromorph structure with the top electrode covering the whole laminated structure as follow:

$$\delta(L) = -3 \cdot d_{31} \cdot s_{11,Si} \cdot s_{11,p} \cdot h_{Si} \cdot (h_{Si} + h_p) \cdot L^2 \cdot V \cdot \frac{1}{K} \qquad (4.2)$$

and:

$$K = 4s_{11,p}s_{11,Si}h_{Si}(h_p)^3 + 4s_{11,p}s_{11,Si}(h_{Si})^3h_p + (s_{11,p})^2(h_{Si})^4 + \ldots$$

$$\ldots + (s_{11,Si})^2(h_p)^4 + 6s_{11,p}s_{11,Si}(h_{Si})^2(h_p)^2 \qquad (4.3)$$

$$d_{31} = e_{31,f} \cdot (s_{11,p} + s_{12,p}) \qquad (4.4)$$

where:
d_{31} = transverse piezoelectric coefficient (pC/m)
$e_{31,f}$ = effective transverse piezoelectric coefficient = -12.5 (C/m^2)
$s_{11,p}$, $s_{12,p}$ = elastic compliance of PZT film (m^2/N)
$s_{11,Si}$ = elastic compliance of silicon = 7.7*10^{-12} (m^2/N)
h_{Si}, h_p = substrate and PZT film thickness (m)
L = beam and top electrode length (m)
V = applied voltage (V)

All the parameters are known except the elastic compliance of the PZT films. In a first approximation, they can be approached by the bulk values $s_{11,p} = 13.8\times10^{-12}$ (m^2/N) and $s_{12,p} = -4.07\times10^{-12}$ (m^2/N) given by Jaffee [39].

It can be observed that the Smits' equation does not take into account the lateral deformation of the beam represented by the Poisson's coefficient.

In the extreme case, when $h_{Si} >> h_p$, it simplifies to

$$\delta(L) = -3 \cdot d_{31} \cdot \frac{s_{11,Si}}{s_{11,p}} \cdot \frac{1}{(h_{Si})^2} \cdot L^2 \qquad (4.5)$$

Taking d_{31} = -128 pm/V, h_{Si} = 10 μm, L = 1 mm, simplified equation (4.5) gives a deflection of 2.036 μm/V compared to 1.779 μm/V taking all the terms in the K factor (equation (4.3)). The difference is about 14.4 %.

4.3.1.2 The model of Gardeniers

Using standard mechanics, Gardeniers [38] express the transverse deflection δ(L) of a piezoelectric/silicon heteromorph cantilever (of length L) as a function of the driving voltage V by:

$$\delta(L) = -6 \cdot \frac{e_{31,f}}{s_{11,p} + s_{12,p}} \cdot \left(s_{11} - \frac{s_{12}^2}{s_{11}}\right)_{Si} \cdot \left(L \cdot L_e - \frac{L_e^2}{2}\right) \cdot \frac{1}{h_{Si}^2} \cdot \frac{w_e}{w_b} \cdot V \tag{4.6}$$

$$\delta(L) = -6 \cdot \frac{e_{31,f}}{s_{11,p}(1 - \nu_p)} \cdot s_{11,Si}\left(1 - \nu_{Si}^2\right) \cdot \left(L \cdot L_e - \frac{L_e^2}{2}\right) \cdot \frac{1}{h_{Si}^2} \cdot \frac{w_e}{w_b} \cdot V \tag{4.7}$$

where:
d_{31} = transverse piezoelectric coefficient (pC/m)
s_{11}, s_{12} = elastic compliance of silicon or PZT (m^2/N)
ν_p, ν_{Si} = Poisson coefficients of silicon (0.278) and PZT
h_{Si} = substrate thickness (hyp. >> h_p, PZT thickness) (m)
w_e, w_b = beam and top electrode width (m)
L, L_e = beam and top electrode length (m)

and

$$\frac{d_{31}}{s_{11,p} + s_{12,p}} = e_{31,f} \tag{4.8}$$

If $w_e = w_b$ and $L_e = L$, equation (4.6) is given by

$$\delta(L) = -3 \cdot e_{31,f} \cdot \left(s_{11} - \frac{s_{12}^2}{s_{11}}\right)_{Si} \cdot \left(\frac{1}{h_{Si}^2}\right) \cdot L^2 \cdot V \tag{4.9}$$

Taking the same values for h_{Si} and L, equation (4.9) gives a deflection of 2.672 µm/V. Figure 4.17 shows a comparison of both model as a function of cantilever silicon thickness.

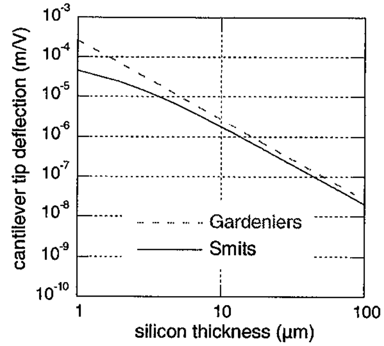

Figure 4.17: Comparison of the predicted tip cantilever deflection as a function of silicon substrate thickness for the models of Gardeniers and Smits

For low values of the silicon thickness, the deflection predicted by the model of Smits is lower than the one given by Gardeniers. For 10 μm thick cantilever, Smits predicts a value of 1.779 μm/V compared to 2.672 μm/V for Gardeniers.

4.3.2 Resonance frequency of multilayers PZT/Pt/SiO$_2$/Si microcantilevers

For the calculation of the resonance frequency, it has been assumed that residual stresses were negligible (silicon thickness > 10 μm). The resonance frequencies of a pure silicon cantilever are given by [40]:

$$\omega_i^2 = \frac{\lambda_i^4}{L^4} \cdot \frac{D}{\mu} \tag{4.10}$$

where D is the rigidity of the beam defined by:

$$D = \frac{E \cdot h^3}{48\pi^2} \tag{4.11}$$

and $\lambda_1 = 1.875$, $\lambda_2 = 4.694$, $\lambda_3 = 7.855$ and $\lambda_4 = 10.996$, h the silicon thickness, L the length of the beam, E the silicon's Young modulus (Pa) and $\mu = \rho h$ the silicon density per unit area. The resonance frequency is also dependant of the other layers in the stack (SiO$_2$, Pt and PZT). In this case, D and μ are replaced by D* and μ* defined by:

$$D^* = \frac{1}{4}\sum_{i=1}^{4}\left[\frac{(h_i - h_n)^3 - (h_{i-1} - h_n)^3}{s^E_{11,i}}\right] \tag{4.12}$$

$$\mu^* = \sum_i \rho_i h_i = \sum_i \mu_i \tag{4.13}$$

with h_n, the position of the neutral plane given by [41]:

$$h_n = \frac{1}{2}\cdot\frac{\sum_{i=1}^{4}\left[\frac{h_i^2 - h_{i-1}^2}{s^E_{11}i\cdot(1-\nu^2(i))}\right]}{\sum_{i=1}^{4}\left[\frac{h_i - h_{i-1}}{s^E_{11}i\cdot(1-\nu^2(i))}\right]} \tag{4.14}$$

where h_i is the z-position and $s_{11,i} = 1/E_i$ the compliance of the layer *i* (1 = silicon, 2 = SiO_2, 3 = Pt, 4 = PZT). The materials properties for the multilayer PZT/Pt/SiO_2/Si microcantilever are summarized in Table 4.2.

Table 4.2: Materials properties of the multilayers PZT/Si microcantilever

layer	h (μm)	s_{11} (Pa^{-12})	ρ (kg/m^3)	μ (kg/m^2)
PZT	1.1	12.4	7900	0.00869
Pt	0.12	7.35	20000	0.0024
SiO_2	1.2	14.2	2220	0.00266
Si	10	7.66	2330	0.0233

For 1 mm beam, 10 μm thick, a resonance frequency of 12.065 kHz and 12.489 kHz are calculated with single silicon layer and multilayer models respectively. The coupling factor of the resonance is given by

$$k^2 = 1 - \frac{\omega_r^2}{\omega_a^2} \tag{4.15}$$

where ω_r and ω_a are the resonance and anti-resonance frequencies.

4.3.3 Characterization methods

The deflection of the microcantilevers as a function of driving voltage has been characterized by means of optical methods. For quasistatic (small ac driving voltage out of resonance under various dc bias) and resonance measurements, the deflection of the beams has been recorded by 3D stroboscopic microscopy [42] (5 nm z-resolution) at the University of Paris/Orsay. This method allows to subtract any dc deflection (for example, due to residual stress). Impedance characterization at the resonance has been carried out using LCR-meter HP-4194 from Hewlett-Packard. Cantilevers thicknesses have been measured using scanning electron microscope (SEM) Philips XL30 (Eindhoven, Holland). Finally, finite element method (FEM) simulations have been carried out in collaboration with D. Schmidt from the Frauenhofer institute (IBMT) using ANSYS SOLID5 software. Materials and FEM fundamentals are given in [43]

4.3.4 PZT/Si microcantilevers arrays

Arrays of simple microcantilevers have been micromachined using the standard piezoelectric MEMS process depicted in section 4.2. PZT thin film used for these devices is PZT 53/47, {100}-textured, 1 μm thick. Functional properties measured on $e_{31,f}$ test samples are $e_{31,f} = -12$ C/m^2, $\varepsilon = 1100$ and $\tan \delta = 3\%$. Figure 4.18 shows an array with 24 microcantilevers of various length (500 and 1000 μm) and width (100, 200, 500 μm). Cantilevers silicon thicknesses are ranging from 10 to 20 μm.

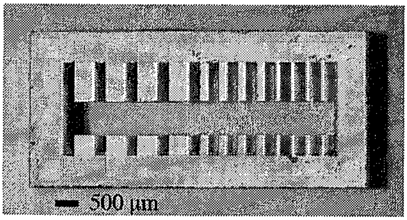

Figure 4.18: Array of PZT/Si microcantilevers

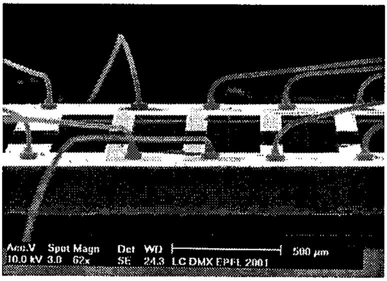

Figure 4.19: SEM side-view image of array with the bonded connecting wires.

To address all physical issues depicted previously, a simple 1000 x 100 μm PZT/Pt/SiO$_2$/Si microcantilever (#A21) has been fully characterized at the resonance and under quasistatic excitation conditions. Its real geometrical dimensions have been measured by SEM.

4.3.5 Characterization of PZT/Si microcantilever at the resonance

The characterization of the microcantilever at the resonance is of primary importance as it will help accessing important parameters such as coupling factors and effective piezoelectric coefficients by means of finite element simulation. To avoid air damping, the admittance curves of microcantilevers have been measured at low pressure (10 Pa). Figure 4.20 shows the admittance curves of the first resonance frequency of PZT/Si microcantilever #A21 (1000x100 μm^2) measured in air (10^5 Pa) and at 10 Pa.

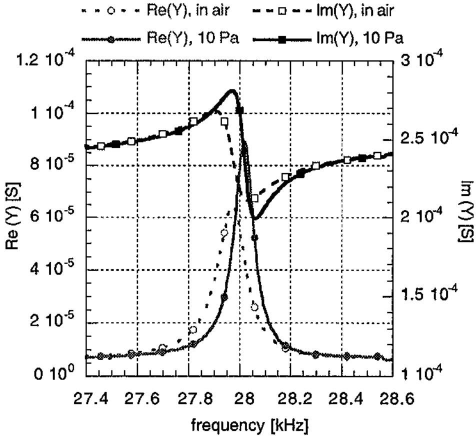

Figure 4.20: Admittance curve of a 1000x100 μm^2 PZT/silicon microcantilever #A21 at P_{atm} and at 10 Pa. $\omega_{1,\ air}$ = 28.017 kHz, $\omega_{1,\ vac}$ = 27.971 kHz.

The coupling and quality factors k and Q amounted to 9.8% / 415 in air and to 8.1% / 610 at 10 Pa respectively. Taking the resonance frequency measured at 10 Pa into equation (4.10) with the multilayer model, a silicon thickness of 23.6 μm is calculated. As the model depicted in equation (4.10) does not take into account thickness non-uniformities, this value is only an averaging that can be used for modal analysis only. Indeed, it has been observed by SEM that the silicon thickness of the microcantilever was not uniform as depicted by Figure 4.21. This non-uniformity was due to the masking effect of the walls during the deep silicon dry etching (see section 4.2.5).

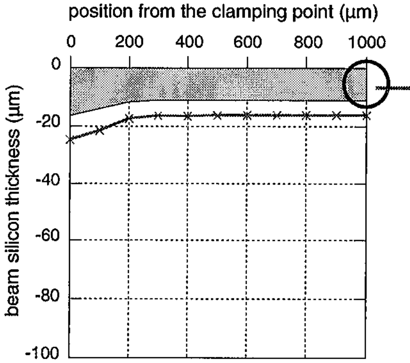

Figure 4.21: Thickness profile of beam #A21 showing the non-uniformity near the clamping point.

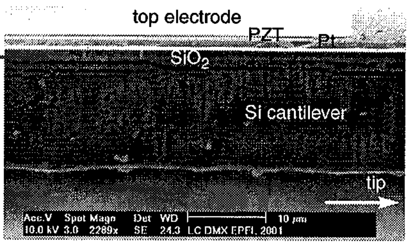

Figure 4.22: SEM image cross-section of microcantilever #A21 near the tip. Silicon thickness = 16 ± 1 μm

FEM undamped modal analysis has been used to simulate and fit admittance curves on measured data. The real microcantilever thickness profile observed by SEM has been integrated in the model. Figure 4.23 shows the simulated and measured admittance curves for the fundamental resonance of microcantilever #A21.

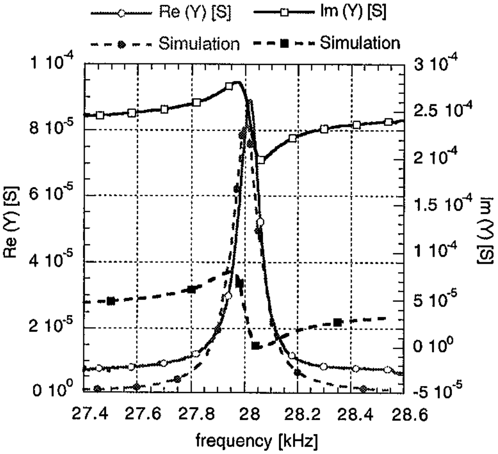

Figure 4.23: Comparison of measured and simulated admittance curves of microcantilever #A21 at the first resonance.

It turns out that both real and imaginary parts are shifted to higher values. This is due to a parasitic capacitance (connecting lines and contact pads) and to the fact that the dielectric loss has not been integrated in the FEM model. Fitting of admittance curves gives also access to materials parameters, in particular to the effective piezoelectric coefficient. Table 4.3 compares the piezoelectric coefficients obtained by FEM simulation with typical experimental data out of PZT 53/47 {100}-textured, 1 µm thick. The transverse piezoelectric coefficient calculated by FEM is close to the real measured value (10.4 C/m^2 by FEM compared to 11-12 C/m^2).

Table 4.3: Comparison of the properties of PZT films obtained by FEM simulation with experimental data of {100}-textured PZT 53/47, 1 µm thick.

	FEM simulation	{100}-textured PZT 53/47, $h_p = 1$ µm
ε	1100	1100
$-e_{31,f}$ (C/m^2)	10.4	11 - 12
$d_{33,f}$ (pm/V)	55	62

The shapes of FEM simulated modes of microcantilever #A21 are represented in Figure 4.24.

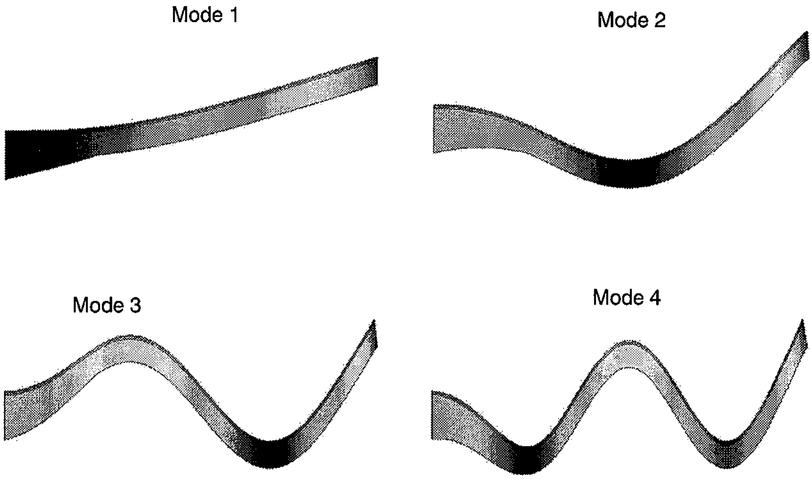

Figure 4.24: FEM simulations of resonance modes of beam #A21 using observed thickness profile. Note: the transverse deflection is overscaled compared to the longitudinal axis. D. Schmitt, Fraunhofer-IBMT, 2001

Table 4.4 summarizes the measured resonance frequencies and coupling factors with FEM simulated values [43]. The correspondence between measured and simulated frequencies is rather excellent. The higher frequencies obtained by FEM simulation, in particular for the fundamental mode, may originate from the fact that the platinum bottom electrode has been neglected in the model. Platinum is a soft and heavy material and it would drive the frequencies to lower values.

Table 4.4: Comparison of measured and FEM simulated resonance frequencies and coupling factors of microcantilever #A21. Real thickness profile from SEM image is used.

Modes	$f_{i,m}$ measured in vac. (kHz)	f_i simulated by FEM [43] (kHz)	difference $f_{i,m} - f_{FEM}$ (%)	calculated coupling factor *k* from admittance curves (-)	FEM simulated coupling factor *k* (-)
1	27.971	28.8	3.1	8.1	9.1
2	162.39	167.7	3.2	4.69	3.9
3	433.78	442.4	2	4.38	3.4
4	831.95	832.9	0.1	3.63	1.5

Figure 4.25 shows the real deflection of modes measured by 3D stroboscopic microscopy. For the fundamental mode, a tip deflection of about 8 μm is measured. For mode 3, the maximal deflection is less than 200 nm.

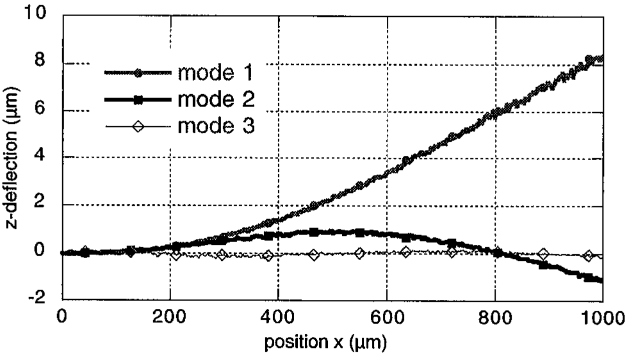

Figure 4.25: z-deflection of cantilever #A21 as a function of resonance mode measured by 3D stroboscopic microscopy.

The comparison between FEM simulated and measured resonance frequencies has shown an excellent agreement. The largest difference (3%) was found for the fundamental mode. As the electromechanical coupling of this mode is larger (curvature of same sign), a very small error on the silicon thickness profile near the clamping point may affect significantly the position of the first resonance. Similar phenomenon but with a larger magnitude (7%) was also reported by Luginbuhl on small PZT/Si_3N_4/Si cantilevers and has been explained by incorrect modeling of the clamping point [44].

4.3.6 Characterization of PZT/Si microcantilever under quasistatic actuation

For the same 1000 x 100 μm^2 microcantilever, quasistatic measurements have been performed at 1 kHz with 1 V ac excitation and increasing dc bias. Figure 4.26 shows the quasistatic deflection profile of the microcantilever #A21 as a function of squared position x^2 and applied dc bias measured by 3D stroboscopic microscopy. It shows an excellent linearity with respect to x^2. Figure 4.27 shows also a linear behavior between the maximal deflection at x = L and the applied dc bias up to 6 V.

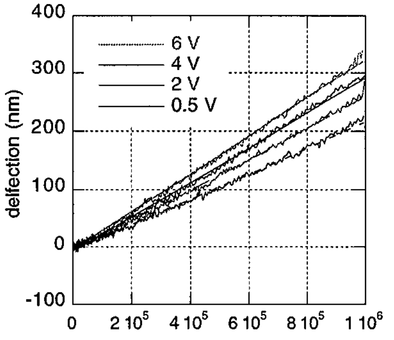

Figure 4.26: Quasistatic deflection profile of microcantilever #A21 as a function of the squared position x^2 from the clamping point and dc bias.

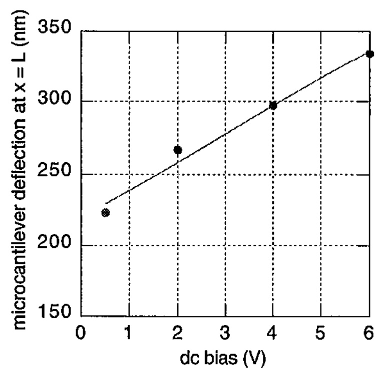

Figure 4.27: Quasistatic deflection at x = 1000 µm of the microcantilever #A21 as a function of applied dc bias. Driving ac voltage is 1 V at 1 kHz.

Using the thickness profile depicted in Figure 4.21, FEM static simulation has given a deflection of 0.626 µm/V (Figure 4.28) compared to 0.225 µm/V at 0 dc bias (Figure 4.27). It is thought that the difference originates mainly from errors in the silicon thickness profile as small difference in the silicon thickness h_{Si} changes the beam deflection in h_{Si}^2.

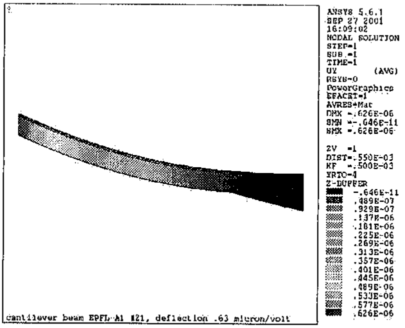

Figure 4.28: FEM static simulation of microbeam #A21.
D. Schmitt, Fraunhofer-IBMT, 2001

Taking the average silicon thickness measured by means of the resonance frequency (23.6 µm), the transverse piezoelectric coefficients d_{31} can be calculated based on the equation of Gardeniers and Smits. The obtained d_{31} are ranging from -80 to -120 pC/m. Both models have given similar results. $e_{31,f}$ can be than derived using equation (4.4) and assuming the elastic constants of bulk PZT ceramics from Jaffe [39]. Compared to measured piezoelectric coefficients (-12 C/m^2), the $e_{31,f}$ values calculated here are lower (-8 C/m^2, remanent value). Here again, the averaging of the microcantilever silicon thickness profile is thought to be the main source of error.

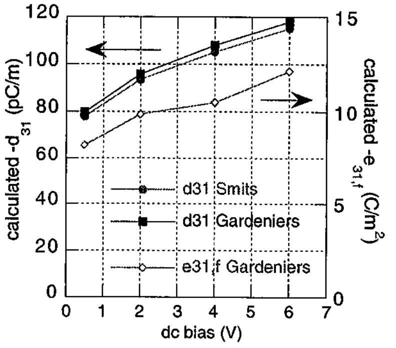

Figure 4.29: d_{31} and $e_{31,f}$ piezoelectric coefficients derived from the slope of Figure 4.26 as a function of dc bias and calculation model. PZT bulk ceramics elastic constant from Jaffe [39] are assumed.

It is also possible that the elastic compliance ($s_{11,p}$ + $s_{12,p}$) in PZT films is lower than in bulk ceramics (dense films are stiffer than bulk ceramics). Consequently, higher $e_{31,f}$ and thus lower d_{31} coefficients would be calculated. Tuchiya, in fact, suggested the latter point. He reported a Young's modulus for PZT films of 91.6 GPa [45]. The corresponding $s_{11,p}$ is thus $10.9*10^{-12}$ Pa^{-1} compared to $13.8*10^{-12}$ for bulk ceramics. Taking a Poisson coefficient of 0.3, $s_{11,p} + s_{12,p}$ amounts to $7.6*10^{-12}$ Pa^{-1}. Taking these values, the difference is rather small and $e_{31,f} = -8.3$ C/m^2 and $d_{31} = -63$ pC/m would be obtained at remanent conditions (0 dc bias).

4.4 SUMMARY

A) Microfabrication of piezoelectric MEMS

In this section, critical issues of piezoelectric MEMS microfabrication have been discussed. To overcome resolution problems in complex device structures, wet etching of PZT films and platinum bottom electrodes have been replaced by new plasma dry etching methods. Micron scale patterns have been obtained using new reactive ion beam etching (RIBE) processes. Due to working pressures two order of magnitude lower than in conventional reactive ion etching (RIE) in inductively-coupled-plasma (ICP) reactors (5 mPa compared to 1 Pa), RIBE processes were found to be much less sensitive to redeposition of etching by-products. The developed processes exhibited also much higher etching rates (2 - 5 times) and similar results in term of etch profile, photoresist stability and removability. These new processes have been successfully integrated into a microfabrication sequence that fully preserves the functionality of piezoelectric thin films. At the end of the micromachining sequence, transverse piezoelectric coefficient $e_{31,f}$ of -12 C/m^2 (at 110 Hz), dielectric permittivity ε of 1100 and loss factor tan δ of 0.03 (at 1 kHz) have been measured on test samples with 1 μm PZT 53/47 {100}-textured thin film.

In-plane laminated PZT/Si structures have been obtained by compensating the tensile stress of platinum bottom electrode and PZT film with compressive SiO_2 thermal oxide. In PZT films, the increase of stress due to poling (up to 50%) has been considered as well. Finally, the integration of PZT thin films on 4 μm thick poly-silicon layer (so called poly-SOI substrate) has been successfully demonstrated. Chemical-Mechanical-Polishing (CMP) of poly-silicon layer has been used to reduce the substrate roughness and thus favor uniform growth of the PZT film. Consequently, highly {100}-textured 1 μm PZT 53/47 thin film and excellent piezoelectric properties ($e_{31,f} = -11$ C/m^2) have been obtained. The combination of thick poly-silicon layer with PZT films may open new perspectives in the microfabrication of piezoelectric MEMS based on surface micromachining.

B) Electro-mechanical properties of PZT/Si microcantilevers

Electro-mechanical properties of piezoelectric microcantilevers have been studied at the resonance and under quasistatic excitations. FEM simulations have shown excellent agreements with respect to measured resonance frequencies and coupling factor. The effective piezoelectric coefficient has been derived by means of measuring the microcantilever admittance curves at the resonance. $e_{31,f}$ = - 10.4 C/m^2 has been calculated, which is well compatible with the values measured on test samples in chapter 3 (- 12 C/m^2). The difference may originate mainly from the approximation of the real silicon thickness profile of the microcantilevers, which is due to the non-uniformity of the deep silicon dry etching process. Whatever the technique we used (test samples or microcantilevers), highly reproducible $e_{31,f}$ values of -10 to -12 C/m^2 have been obtained with PZT 53/47 {100}-textured thin films.

Transverse piezoelectric coefficients $e_{31,f}$ as a function of applied dc bias have been derived from quasistatic (off-resonance) operations of microcantilevers. While theoretical models of Smits and Gardeniers have been applied to calculate d_{31} coefficients, elastic compliance of bulk PZT has been introduced to derive the $e_{31,f}$ coefficients. It turns out that both models have given similar results with $e_{31,f}$ = -8.0 C/m^2 at 0 dc bias (remanent value). This value is lower than those measured on test samples (-12 C/m^2). Here again, it is thought that the difference originates mainly from errors in averaging the real silicon thickness profile of the microcantilever. Finally, the elastic compliance of PZT films that can be different compared to bulk ceramics may play a role as well. Using the values given by Tuchiya, $e_{31,f}$ of -8.3 C/m^2 would be obtained.

4.5 REFERENCES

1. Elwenspoek, M. and H. Jansen, *Silicon micromachining*, ed. C.U. Press. 1998, Cambridge.
2. Madou, M., *Fundamentals of Microfabrication*. 1997, Boca Raton: CRC Press.
3. Gross, S.J., et al., *Reliable integration of piezoelectric lead zirconate titanate with MEMS fabrication process*. Proceedings of the SPIE, 2001. **4558**: p. 72-80.
4. Baborowski, J., et al. *Micromachining of Piezoelectric MEMS*. in *Transducers 2001*. 2001. Munich.
5. Muralt, P., et al., *Integration of Piezoelectric* $Pb(Zr_xTi_{1-x})O_3$ *(PZT) thin films into micromachined sensors and acuators*, in *Materials and Process Integration for MEMS*,

P.F.E.H. Tay, Editor. 2002, Kluwer Academic Publishers, The Netherlands.

6. DeVoe, D.L. and A.P. Pisano. *A Fully Surface-Micromachined Piezoelectric Accelerometer.* in *Transducers '97, International Conference on Solid-State Sensors and Actuators*. 1997. Chicago.

7. Kim, J.H., et al., *Fabrication Processof PZT Piezoelectric cantilever unimorphs using surface micromachining.* Integrated Ferroelectrics, 1997. **15**: p. 325-332.

8. Flynn, A.M., et al., *Piezoelectric micromotors for microrobots.* J. Microelectromechanical Sytems, 1992. **1**: p. 44-51.

9. Dubois, M.-A. and P. Muralt, *PZT Thin Film Actuated Elastic Fin Micromotor.* IEEE Transactions on Ultrasonics, Ferroelectrics, and Frequency Control., 1998. **45**(5): p. 1169-1177.

10. Racine, G.-A., P. Muralt, and M.-A. Dubois, *Flexural-standing-wave elastic force motor using ZnO and PZT thin film on micromachined silicon membranes for wristwatch applications.* Smart Mater. Struct., 1998. **7**: p. 404-416.

11. Baborowski, J., et al., *Fabrication and Characterization of Micromachined Accelerometers based on PZT thin films.* Ferroelectrics, 1999. **224**: p. 283-290.

12. Kunz, K., P. Enoksson, and G. Stemme, *Highly sensitive triaxial silicon accelerometer with integrated PZT thin film detectors.* Sensors and Actuators A, 2001. **92**: p. 156-160.

13. Lee, S.S. and R.M. White, *Piezoelectric cantilever acoustic transducer.* J. Micromech. Microeng., 1998. **8**: p. 230-238.

14. Schroth, A., et al., *Application of sol-gel deposited thin PZT film for actuation of 1D and 2D scanners.* Sensors and Actuators A, 1999. **73**: p. 144-152.

15. Lee, C., T. Itoh, and T. Suga, *Self-excited piezoelectric PZT microcantilevers for dynamic SFM - with inherent sensing and actuating capabilities.* Sensors and Actuators A, 1999. **72**: p. 179-188.

16. Miyahara, Y., *PZT cantilever for non-contact atomic force microscopy.* Appl. Surf. Sci., 1999. **140**: p. 428-431.

17. Bernstein, J.J., et al., *Micromachined high frequency ferroelectric sonar transducers.* IEEE Tran. UFFC, 1997. **44**(5): p. 960-969.

18. Kloeck, B., et al., *Study of electrochemical etch-stop for high-precision thickness control of silicon membranes.* IEEE Transactions on Electron Devices, 1989. **36**(4): p. 663-669.

19. Fluckiger, P., et al., *Standard processes at the Center of Microtechnology - EPFL.* 2002, http://microtechnique.epfl.ch/cmi/.

20. Lee, E., et al., *Effects of top electrode annealing on the PZT thin film.* Integrated Ferroelectrics, 1997. **16**: p. 165-174.

21. Troiler-McKinstry, S., et al. *Etched piezoelectric structures.* in *International Symposium of Applied Ferroelectrics, ISAF.* 1986. Bethlehem.

22. Zeto, R., et al., *Dry etching of sol-gel PZT.* Mat. Res. Soc. Symp. Proc., 1999. **546**: p. 159-164.

23. Pan, W., et al., *Reactive ion etching of PZT and* RuO_2 *films by environmentally safe gases.* J. Mater. Res., 1994. **9**(11): p. 2976-2980.

24. Chung, C.W., *Reactive ion etching of PZT thin films in an inductively coupled plasma.* J. Vac. Sci. Technol. B, 1998. **16**(4): p. 1894-1900.

25. Jung, J.-K. and W.-J. Lee, *Dry etching of PZT films in* CF_4 *and* Cl_2/CF_4 *inductively coupled plasmas.* Jpn. J. Appl. Phys., 2001. **40**: p. 1408-1419.

26. Williams, K., et al. *Reactive ion beam etching of ferroelectric materials using a RF inductively coupled ion beam source.* in *IEEE International Symposium on Application of Ferroelectrics (ISAF'96).* 1996.

27. Boukari, F., et al., *A very compact electron cyclotron resonance ion source.* Rev. Sci. Instrum., 1994. **65**(4): p. 1097-1099.

28. Baborowski, J., et al., *Mechanisms of* $Pb(Zr_{0.53}Ti_{0.47})O_3$ *Thin Film Etching with ECR/RF Reactor.* Integrated Ferroelectrics, 2000. **31**: p. 261-271.

29. Vossen, J.L. and W. Kern, *Thin Film Process*, ed. 1. Vol. V-1. 1978, New-York: Academic Press.

30. Frankenthal, R.P. and D.H. Eaton, *Electroetching of platinum in the titanium-platinum-gold metallization on silicon integrated circuits.* J. Electrochem. Soc. : Solid-state science and technology, 1976. **123**(5): p. 703-706.

31. Baborowski, J., P. Muralt, and N. Ledermann, *Etching of platinum thin films with dual frequency ECR/RF reactor.* Integrated Ferroelectrics, 1999. **27**: p. 243-256.

32. Baborowski, J., et al., *Etching of* RuO_2 *and Pt thin films with ECR/RF reactor.* Vacuum, 2000. **56**: p. 51-56.

33. Lang, W., *Silicon Microstructuring technology.* Materials Science and Engineering, 1996. **R17**: p. 1-55.

34. Lärmer, F. and A. Schilp, *US6284148: Method for anisotropic etching of silicon.* 2001: USA.

35. Hynes, A.M., et al., *Recent advances in silicon etching for MEMS using the* ASE^{TM} *process.* Sensors and Actuators A, 1999. **74**: p. 13-17.

36. Yasseen, A.A., N.J. Mourlas, and M. Mehregany, *Chemical-Mechanicap Polishing for polysilicon Surface Micromachining.* J. Electrochem. Soc., 1997. **144**(1): p. 237-242.

37. Smits, J.G. and W. Choi, *The Constituent Equations of Piezoelectric Heterogeneous Bimorphs.* IEEE Transactions on Ultrasonics, Ferroelectrics, and Frequency Control., 1991. **38**(3): p. 256-270.
38. Gardeniers, J.G.E., et al., *Direct measurement of piezoelectric properties of sol-gel PZT films.* Journal of the Korean Physical Society, 1998. **32**: p. S1573-77.
39. Jaffe, B., W.R. Cook, and H. Jaffe, *Piezoelectric Ceramics.* 1971, London: Academic Press.
40. Szabo, I., *Höhere Technische Mechanik.* 1956, Berlin: Springer.
41. Söderquist, J., *Similarities between piezoelectric thermal and other internal means of excitation vibrations.* J. Mircomech. Microeng., 1993. **3**: p. 24-31.
42. Petitgrand, S., *3D measurement of micromechanical devices vibration mode shapes with stroboscopic interferometric microscope.* Optics and Lasers in Eng., 2001. **36**: p. 77-101.
43. Schmitt, D., *Materials and FEM Fundamentals.* 2001, Fraunhofer IBMT: Karlsruhe.
44. Luginbuhl, P., et al., *Piezoelectric cantilever beams actuated by PZT sol-gel thin film.* Sensors and Actuators A, 1996. **54**: p. 530-535.
45. Tuchiya, T., et al., *Preparation and properties of piezoelectric lead zirconate thin film for microsensors and microactuators by sol-gel processing.* Journal of the Ceramic Society of Japan, Int. Edition, 1996. **104-156**: p. 159-163.

ABSTRACT

This work dealt with the establishment of a reproducible and industrially exploitable fabrication technology for piezoelectric MEMS based on PZT thin films. {100}-textured piezoelectric 1-4 μm thick films were found to be the most suited materials for MEMS applications where a strong transverse $e_{31,f}$ coefficient is required. Values of 11.5 to 12.5 C/m^2 throughout the investigated thickness range have been obtained. PZT MEMS requires some special microfabrication processes. The patterning of platinum electrodes in ICP reactor with an Ar/Cl_2 gas mixture gave satisfying results. For 1 μm PZT films, excellent results were achieved with dry etching in an ECR/RF low-pressure reactor. Above 1 μm thickness, wet etching technique was used. The chosen process flow was such that all layers up the top electrode were first deposited, and then sequentially patterned. In this way, the functional properties were completely maintained. Finally, the process flow related to PZT was successfully combined with deep silicon etching techniques to produce free standing structures. The applicability of the processes has been demonstrated by means of two piezoelectric micro-electro-mechanical devices. First, a cantilever acoustic sensor for low frequency applications (< 50 Hz) has been developed for integration in photoacoustic gas detectors. A high device sensitivity of up to 150 mV/Pa has been obtained with noise level corresponding to a few mPa, mainly due to the preamplifier. The second device was based on a silicon/PZT diaphragm to produce a vibrating structure in view of fabricating ultrasonic transducers for position sensors and non-destructive testing probes. The study of the basic properties of such structures has shown excellent results as coupling factors k^2 up to 5% for PZT 2 μm / Si 4 μm SOI membranes held with four small bridges. Ultrasonic wave transmission between two devices has been achieved up to a distance of 200 mm.

The microfabrication of piezoelectric MEMS was found to be a complex task where all aspects from materials, microfabrication, and device design to assessment of performance are closely interconnected. Piezoelectric MEMS can offer exciting opportunities to fabricate innovative and performing devices.

VERSION ABRÉGÉE

Cette recherche couvre l'établissement d'un procédé reproductible et exploitable industriellement pour la fabrication de microsystèmes piezoélectriques basés sur des couches minces de PZT. Grâce à la texturation selon {100}, les propriétés de ce matériau ont démontré qu'elles étaient particulièrement adaptées aux microsystèmes requérant un grand coefficient transverse $e_{31,f}$. Dans toute la gamme d'épaisseur étudiée (1-4 μm), un coefficient $e_{31,f}$ de 11.5 à 12.5 C/m^2 a été obtenus. La fabrication de microsystèmes piezoélectriques nécessite des procédés particuliers. La structuration des électrodes inférieures en platine dans un réacteur ICP avec une chimie Ar/Cl_2 a donné de bons résultats. Pour une couche mince de 1 μm de PZT, d'excellents résultats ont été obtenus dans un réacteur basse pression ECR/RF. Toutefois, au dessus de 1 μm, la gravure humide a dû être utilisée. La succession des procédés a été choisie de telle sorte que toutes les couches minces jusqu'à l'électrode supérieure ont été déposées préalablement puis structurées l'une après l'autre. De cette manière, les propriétés fonctionnelles de la couche piezoélectrique ont été complétement conservées. Finalement, les procédés associés à la couche piezoélectrique ont été combinés avec succès à la gravure profonde du silicium pour produire des structures de type membrane ou poutre. L'application de ces procédés a été démontrée avec succès par la microfabrication de deux microsystèmes. Le premier est un capteur acoustique pour basses fréquences (< 50 Hz) basé sur une poutre. Une sensibilité de 150 mV/Pa et un niveau de bruit correspondant à quelques mPa ont été mesurés. Ce microphone a ensuite été intégré avec succès dans un détecteur de gaz photoacoustique. Le deuxième device est basé sur des membranes composites PZT/Si avec comme objectif la réalisation de transducteurs ultrasoniques pour des capteurs de position et des outils de contrôle non-destructifs. L'étude des propriétés fondamentales a montré d'excellent résultats avec des facteurs de couplage k^2 de 5% pour un diaphragme composé de 2 μm de PZT déposé sur 4 μm Si obtenu avec une technologie SOI. La transmission d'onde ultrasonique dans l'air a été détectée jusqu'à une distance de 200 mm.

La microfabrication de microsystèmes piézoélectriques basés sur des couches minces de PZT est une tâche complexe où tous les aspects, qu'ils soient matériaux, microfabrication, design et étude des performances sont étroitements liés. Les microsystèmes piézoélectriques offrent des opportunités excitantes pour la réalisation de devices innovants et performants.

LIST OF ABREVIATIONS

AFM	Atomic Force Microscopy
BHF	Buffered HF
CMOS	Complementary Metal Oxide Systems
CMP	Chemical Mechanical Polishing
CSD	Chemical Solution Deposition
DW	Domain Wall
ECR	Electron Cyclotron Resonance
FEM	Finite Elements Modelling
FOM	Figure of Merit
ICP	Inductively Coupled Plasma
LPCVD	Low Pressure Chemical Vapor Deposition
MEMS	Micro Electro Mechanical Systems
MOCVD	Metal Organic Chemical Vapor Deposition
MPB	Morphotropic Phase Boundary
PCB	Printed Circuit Board
PLD	Pulsed Laser Deposition
cMUT's	Capacitive Micromachined Ultrasonic Transducers
pMUT's	Piezoelectric Micromachined Ultrasonic Transducers
PR	PhotoResist
PSG	Poly Silicon Glass (sacrificial layer)
PVD	Physical Vapor Deposition
PZT	$Pb(Zr_x, Ti_{1-x})O_3$
RF	Radio Frequency
RIBE	Reactive Ion Beam Etching
RIE	Reactive Ion Etching

RTA	Rapid Thermal Annealing
SAW	Surface Acoustic Wave
SEM	Scanning Electron Microscope
SFM	Scanning Force Microscope
SMD	Surface Mounted Devices
S/N	Signal to Noise ratio
SOI	Silicon On Insulator
TEM	Transmission Electron Microscope
XRD	X-ray Diffraction

LIST OF SYMBOLS

Chapter 1 - Introduction

c_{ij}	elastic modulus (N/m^2)
D_i	density of charge (C/m^2)
d_{ik}	piezoelectric coefficient expressed either in (pm/V) or (C/N)
$d_{33,f}$	effective longitudinal piezoelectric coefficient for thin films (pm/V)
d_{33}	longitudinal piezoelectric coefficient, unclamped (pm/V)
d_{31}	transverse piezoelectric coefficient, unclamped (pm/V)
e_{ij}	piezoelectric coefficient (C/m^2)
$e_{31,f}$	effective transverse piezoelectric coefficient for thin films (C/m^2)
$\varepsilon_{ij}{}^{T}$	dielectric permittivity tensor (kl = 1..6 and ij = 1..3)
$\tan \delta$	dielectric loss (-)
ε_0	permittivity = 8.854e-23 (F/m)
E_i	electrical field (V/m)
$s_{kl}{}^{E}$	elastic compliance (m^2/N)
σ_k	mechanical stress (N/m^2)
S_k	strain (-)

Chapter 2 - Experimental methods

I(hkl)	intensity of the orientation hkl
I_0(hkl)	intensity of the orientation hkl in reference random powder

P(hkl)	texture index
ν_s	Silicon Poisson's coefficient = 0.278 (-)
R_0	substrate radius of curvature before film deposition (m)
R	substrate radius of curvature after film deposition (m)
t_s	substrate thickness (m)
t_f	film thickness (m)
Y_s	Young's modulus (GPa)
$Y_s/(1-\nu_s)$	Biaxial Young's modulus (GPa)

Chapter 3 - Study of {100}-oriented PZT piezoelectric thin films for MEMS

$\delta(L)$	beam vertical deflection at x = L (m)
h_{Si}	silicon substrate thickness (m)
h_p	piezoelectric film thickness (m)
w_e	electrode width (m)
w_b	beam width (m)
L	beam length (m)
L_e	electrode length (m)
V	applied voltage (V)
$k^2_{p,f}$	piezoelectric material coupling factor (-)
Y	Young's modulus (GPa)
ν	Poisson's coefficient (-)
P_3	polarization along 3-axis (C/m^2)
Q_{12}	electromechanical coupling constant

Chapter 4 - Microfabrication and electromechanical properties of PZT/Si microcantilevers

D	rigidity (Nm)
D*	rigidity of a multilayer (Nm)
E	Young's modulus (N/m^2)
h_n	vertical position of the neutral plane (m)
h_i	vertical position of the the film i (m)
h_{Si}	silicon structure thickness (m)
k^2	coupling factor (-)
M	moment (Nm)
μ	density per unit area (kg/m^2)

μ^*	density per unit area of a multilayer (kg/m^2)
ρ	density (kg/m^3)
σ_i	film stress (MPa)
t_i	film thickness (m)
ω_i	resonance frequency of mode i (Hz)
ω_r	resonance frequency (Hz)
ω_a	anti-resonance frequency (Hz)

Chapter 5 - PZT/Si piezoelectric cantilevers and bridges as low frequency acoustic sensor for miniaturized photoacoustic gas detector

a	width of a slit (m)
b	length of a slit (m), developed length = 3*b for a cantilever
C	slit air conductance (m^3/s)
D_h	hydraulic diameter (m)
$D_3(x)$	charge density as a function of position x (C/m^2)
E_{Si}	silicon Young's modulus
f	modulation frequency (Hz)
h_{Si}	silicon structure thickness (m)
J	current response (A)
Kn	Knudsen number (-)
L	structure length (m)
ν	Poisson's coefficient (-)
η	air viscosity (Nm)
P_0	pressure amplitude (N/m^2)
P_{atm}	atmospheric air pressure (N/m^2)
Q	charge response (C)
Q	air flow (Pa m^3/s)
ρ	air density (kg/m^3)
Re	Reynolds number (-)
S, S_0	acoustic sensor sensitivity (V/Pa)
t	slit length = cantilever thickness (m)
u	air speed (m/s)
V_1, V_2	volume (frontside and backside) (m^3)
w_{el}	top electrode width (m)
ω	excitation frequency (Hz)
x	position (m)

$\xi(x)$	strain profile along a beam (-)

Chpater 6 - Fundamental properties of piezoelectric micromachined ultrasonic transducers (pMUT's)

E	Young's modulus (MPa)
h	disc thickness (m)
k^2	coupling factor (-)
ν	Poisson's coefficient (-)
r	radius (m)
U_D	Elastic energy of a plate (J)
$w(r)$	vertical deflection of a plate (m)
t_p	piezoelectric film thickness (m)
t_{Si}	silicon structure thickness (m)
t_{Pt}	platinum bottom electrode thickness (m)
t_{SiO2}	silicon oxide film thickness (m)

ACKNOWLEDGEMENTS

I acknowledge gratefully Professor Nava Setter who provided me with all the means necessary to carry out this research and last but not least, for keeping high the Lab spirit !

I would like to thank my thesis supervisor, Dr. Paul Muralt, for his constant support and availability, and for the freedom he gave me during this thesis.

I warmly acknowledge my collegues Dr Jacek Baborowski and Dr Sandrine Gentil for the excellent support during this thesis, in particular on dry etching and electronic microscopy (Jacek) and on sol-gel precursors and X-ray diffraction (Sandrine). But most of all, for the excellent team work and the brainstorming sessions in Zone 8.

I am indebted to the other members of the jury who agreed to be co-examiners: Prof. D. Landolt (EPFL), Prof. P. Gaucher (Ecole Centrale Paris), Prof. H. Bleuler (EPFL), and Dr. F. Gueissaz (Asulab, Swatch Group).

I warmly thank Dr Philippe Fluckiger and his team of the Center of Microtechnology (CMI-EPFL) for their excellent support and for all the daily work on equipments maintenance. I also acknowledge Mr Corradini (IMT-IPM) and Mr Vaucher (Accort) for all the "critical" work on device bonding.

I wish also to thank Dr Martin Forster (Siemens-Cerberus), Dr Philippe Bachmann (Aritron) and Dr Jean-Paul Pellaux (Orbisphere) for their collaboration in the development of the photoacoustic gas cell.

I wish to thank Dr D. Schmitt (Fraunhofer-IBMT, Karlsruhe) for his help with the FEM simulations of micro-cantilevers and Dr S. Petitgrand (Université de Paris-Orsay) for his support with the stroboscopic measurements of vibrating structures.

I thank also the IR-Microsystems team; Dr Markus Kohli, Dr Bert Willing and Dr Andreas Seifert for their advices and support in many aspects.

The machine shop of the Department of Materials is acknowledged for their prompt and excellent realisation of all the complicated mechanical parts I needed.

I would like to acknowledge all my friends and collegues: Sandrine, Claude, Juliette, Marc, Jacek, Arnaud, Captain TEM, Zian, Lucian, Anna, Igor, Jacques, Eva, Dragan, Enrico, Florian, Kyle, Simon and Kapil who helped me in this entrepreneurship long track by keeping high the spirit.

Finally, I would like to warmly acknowledge my parents and grand-parents, my dear petite marmotte and my brothers Gen. P.Y. "meca!" Pelton, Me D.A. Floris for their constant support.

* * *

TABLE OF CONTENTS

INTRODUCTION

EXPERIMENTAL METHODS

Study of {100}-oriented PZT piezoelectric thin films for MEMS

Microfabrication and electromechanical properties of PZT/Silicon microcantilevers

PZT/Si piezoelectric cantilevers and bridges as low frequency acoustic sensor for miniaturized photoacoustic gas detectors

FUNDAMENTAL PROPERTIES OF PIEZOELECTRIC MICROMACHINED ULTRASONIC TRANSDUCERS (PMUT'S)

CHAPTER 5

PZT/SI PIEZOELECTRIC CANTILEVERS AND BRIDGES AS LOW FREQUENCY ACOUSTIC SENSORS FOR MINIATURIZED PHOTOACOUSTIC GAS DETECTORS

5.1 INTRODUCTION

During the last 15 years, the growing awareness toward the environment has driven the research on multiple gas sensors for atmospheric pollution monitoring, detection of toxic molecules in industrial disposals and prevention of fire and risk of explosion. Selectivity, high sensitivity as well as reliability and long term stability are some of the characteristics required for hazardous gas detection.

The principle of photoacoustic gas detection is based on the measurement of a pressure modulation generated by the absorption of an infrared (IR) radiation. This IR radiation is transform into gas intermolecular vibrational-rotational energy, which is quickly released in the form of translational energy and thus pressure change in the photoacoustic cell. The signal produced by the following pressure increase is detected by an acoustic sensor (see Figure 5.1). The selectivity is obtained by inserting an interference bandwidth filter corresponding to the absorption wavelength of the gas to detect (for example, 4.25 μm for CO_2, 3.55 μm for CH_4). One of the great advantages of photoacoustic gas detectors over other gas sensors are the selectivity (IR filter), the high sensitivity and, in optimized cells, the linear response to the gas concentration.

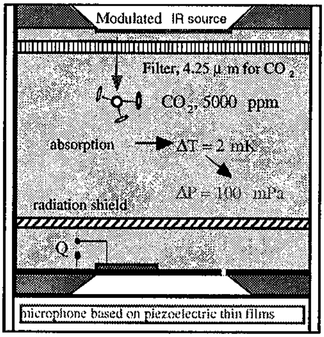

Figure 5.1: Schematic of a photoacoustic gas detector

Historically, the photoacoustic effect has been discovered by Bell in 1880 with the photophone [1]. In the original experiment, an intensity-modulated sunlight beam was focused on a selenium cell. The change of the cell electrical resistance with the light intensity was then converted into a modulated telephonic speech. In 1881, Roentgen and Tyndall extended this effect to liquids and gases [2], [3]. Later, in the middle of the 20th century, Pfund gave new impulsions with his work on the infrared absorption of gases [4]. But it is only in the 70's with the work of Kreutzer that started the real development of photoacoustic spectrometry [5]. Photoacoustic gas cells using thermally modulated IR source mounted with interference filters appeared only at the end of the 80's thanks to the pioneering work of Oehler [6], [7].

Today, photoacoustic detectors are made with commercial microphones with typical dimensions of ø 10 x 7 mm height and are thus occupying a large volume (0.5 cm^3). For many applications such as smoke detectors or probes to measure dissolved gases, the miniaturization of the photoacoustic gas cell is a must. The use of micromachined IR emitters and new miniaturized piezoelectric microphones can thus help reducing the size and increasing the sensitivity of photoacoustic detectors. The magnitude of typical pressure amplitudes to detect is about 100 mPa, which corresponds to a CO_2 concentration of about 5000 ppm [8]. Since the IR light modulation is limited to an upper frequency of 100 Hz (limited by the IR source thermal inertia), there is a need for dedicated miniaturized microphones with high sensitivity at low frequencies (10 - 30 Hz).

Up to now, only pressure sensors based on diaphragm deflection have been used. However, very compliant and thin structures are required to exhibit sufficient sensitivity [9]. It has been also observed by Ried that an all-edge clamped membrane usually presents residual stresses that reduce further the sensor response [10]. Consequently, to enhance the performances, a smart solution consists in replacing the diaphragm by a partially unclamped structure like a cantilever or a bridge.

Cantilevers with piezoelectric thin films are basic structures for a number of applications, such as accelerometers [11], audio microphone and microspeakers (>200 Hz) [12] or AFM probes [13]. Their potential as acoustic sensor for low frequencies could be of a primary interest. Using simple mechanics and introducing transverse piezoelectric effect, first calculations based on one dimensional strain profile have shown that piezoelectric cantilevers can afford sensitivity about 24 times higher than simple and fully clamped membrane of comparable size and thickness (see Figure 5.2).

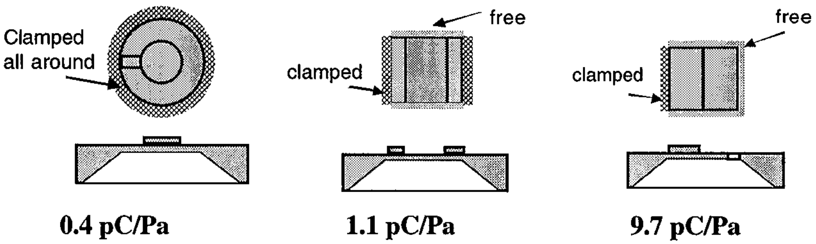

Figure 5.2: Theoretical sensitivity of a membrane, bridge and cantilever ($e_{31,f}$ = -12.5 C/m^2, diameter, length = 2 mm, silicon thickness = 10 μm). See §5.2.2 and §5.2.3 for the complete derivation.

In 1996, White and Lee have proposed the cantilever concept for an audio microphone and microspeaker [12]. To detect the deflection of the cantilever, a 0.5 μm thick ZnO layer has been used. As shown in chapter 1, the transverse piezoelectric coefficient of ZnO is about 15 times lower than the one of (100) PZT 53/47 described in chapter 3. Important improvements on the device sensitivity are thus expected.

The presence of a slit in partially unclamped structures such as cantilever and bridge implies an air leak to the structure backside. This dramatically reduces the sensitivity at low frequency due to the equalization of the pressure on both side of the device. The art of making piezoelectric cantilever acoustic sensor is thus to design very narrow slit and perfectly in-plane structures in order to achieve low air conductance through the slit and thus low cut-off frequency (< 10 Hz). In the work of Lee, despite multiple deposition of different thin films on both sides of the cantilever to balance the stresses, a large residual deflection of more than 20 μm still occurred, which exclude the use of this microphone for frequencies below 200 Hz. However, it was suitable for audio frequencies.

The aim of this chapter is to present the device physics, specific microfabrication issues and the characterization of piezoelectric acoustic sensors for low frequency applications. Integration into miniature photoacoustic gas detector is demonstrated as well.

5.2 DEVICE PHYSICS OF CANTILEVER AND BRIDGE ACOUSTIC SENSOR

The device physics of piezoelectric cantilever and bridge acoustic sensors has been divided in three parts. First, the residual stresses in the structure have to be mastered, meaning that the geometry of the beam (thickness, length) have to accommodate a residual stress in the order of the typical error of film stress measurements. Second, the sensitivity of cantilever and bridge acoustic sensors will be derived using the law of mechanics and piezoelectricity. Finally, the influence of the air conductance through the slit surrounding the structure will be determined to predict the frequency response of the device.

5.2.1 Cantilever bending due to residual stress in thin films

To achieve sufficient sensitivity at 10-20 Hz, the air leak through the slit around the structure has to be controlled and minimized. In that sense, any residual bending due to uncompensated stress within the structure will increase the air conductance and thus, dramatically decrease the sensor sensitivity. In a first approximation, we have assumed that the conductance does not significantly change if the residual deflection is not larger than the beam thickness h_{Si}. Knowing the typical error on film stress measurements ($\sigma_{res} = 10$ MPa), we can calculate the dimensions of a beam that will not give a deflection larger than its thickness.

The cantilever tip deflection δ due to the residual stress σ_{res} in a t_f thick film is given by:

$$\delta = \sigma_{res} \cdot \frac{1-\nu}{E} \cdot \frac{3 \cdot t_f \cdot L^2}{h_{Si}^2} \tag{5.1}$$

Where E and ν are the Young modulus and Poisson's coefficient of silicon, h_{Si} and L the thickness and length of the cantilever.

The residual moment (Nm) (equivalent to a residual stress (MPa) in a $t_f = 1$ μm film) that give a cantilever tip deflection of 10 μm is shown in Figure 5.3 as a function of L and h.

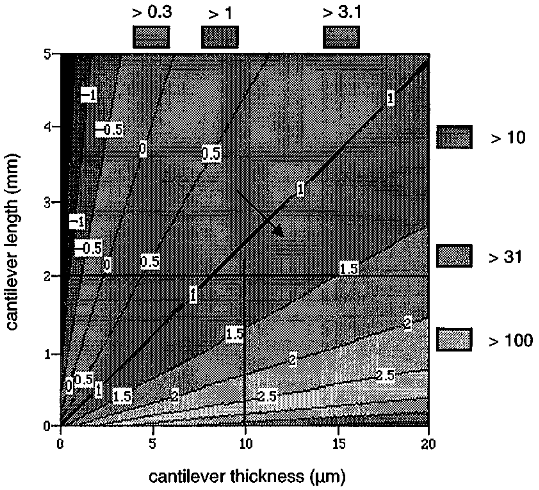

Figure 5.3: Residual moment (log scale) generating a 10 μm bending at the tip of a cantilever of length L and thickness h_{Si} (equivalent to the stress (MPa) of 1 μm thin film).

Below the line "1", corresponding to 10 MPa, any larger residual stress will not generate a tip deflection larger than 10 μm. Thus, a cantilever length shorter than 2.5 mm with a thickness of 10 μm or more represents an optimal trade-off between the sensor response and the sensitivity to uncompensated and residual stress. For comparison, 10 MPa is equivalent to the stress generated by 30 nm of thermal SiO_2 ($\sigma = -300$ MPa).

5.2.2 Sensitivity of cantilever acoustic sensor - piezoelectric part

Basically, two important parameters drive the response of a cantilever acoustic sensor. First, the intrinsic sensitivity of the piezoelectric cantilever is mainly related to the geometry of the beam and the transverse piezoelectric coefficient. Then, the frequency response of the device far from the resonance is directly related to the pressure gradient between the two sides of the beam, i.e. is function of the air flowing through the slit surrounding the cantilever. The size of the slit is thus extremely important.

Without considering the phenomenon of the air conductance, the sensitivity of an acoustic sensor based on a PZT coated cantilever (see Figure 5.4) is derived as follow:

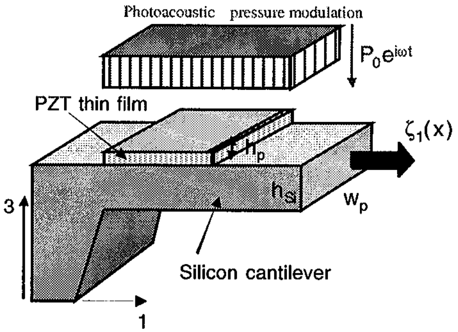

Figure 5.4: Silicon cantilever under a photoacoustic pressure modulation.

The in-plane strain in the piezoelectric thin film along the 1-axis, in the limit of a thin PZT film ($h_p << h_{Si}$), is given by equation (5.2).

$$\xi_1(x) = \frac{3}{E_{Si}h_{Si}^2}\cdot(L-x)^2\cdot P(t) \tag{5.2}$$

Where h_{Si} is the cantilever thickness, E_{Si} the silicon Young modulus, L the length of the cantilever and $P(t) = P_0e^{i\omega t}$, the photoacoustic pressure modulation.

Due to the transverse piezoelectric effect, this strain creates a D-field along the 3-axis.

$$D_3(x) = e_{31,f}\cdot(1-\upsilon)\cdot\xi_1(x) \tag{5.3}$$

Where $D_3(x)$ is the charge density, $e_{31,f}$ the transverse piezoelectric coefficient and ν the silicon Poisson's coefficient.

The charge is then given by equation (5.3) integrated between 0 and L/2 and multiplied by the width w_{el} of the top electrode.

$$Q(t) = \int D_3(x) \cdot w_{el} \cdot dx = e_{31,f} \cdot (1-\upsilon) \cdot w_{el} \cdot \frac{3}{Eh_{Si}^2} \cdot P(t) \cdot \int_0^{\frac{L}{2}} (L-x)^2 dx \quad (5.4)$$

Integrating equation (5.4), the charge and current response to a pressure modulation $P(t) = P_0 e^{iwt}$ are respectively given by:

$$Q(t) = \frac{7}{8} \cdot e_{31,f} \frac{(1-\upsilon)w_{el}}{E} \cdot \frac{L^3}{h^2} \cdot P(t) \quad (5.5)$$

$$J(t) = \frac{7}{8} \cdot e_{31,f} \frac{(1-\upsilon)w_{el}}{E} \cdot \frac{L^3}{h^2} \cdot i\omega \cdot P(t) \quad (5.6)$$

Assuming an electrode width w_{el} equal to the cantilever length (square cantilever), the sensitivity of the device is proportional to L^4/h^2. Figure 5.5 shows the device sensitivity as a function of cantilever length and thickness. Taking $e_{31,f} = -12.5$ C/m^2, L = w_{el} = 2 mm and h_{Si} = 10 μm, a sensitivity S_0 of about 9.7 pC/Pa or 610 pA/Pa @ f = 10 Hz ($\omega = 2\pi f$) is expected.

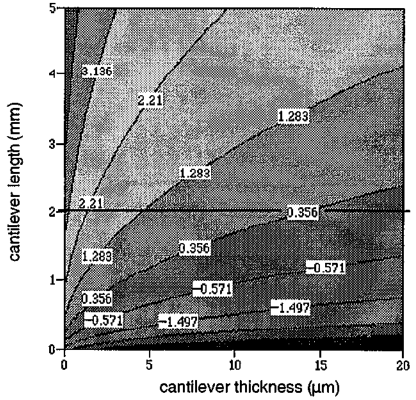

Figure 5.5: Dependence of cantilever sensitivity S_0 on geometrical factors (length and thickness).

5.2.3 Sensitivity of bridge acoustic sensor - piezoelectric part

The derivation of the sensitivity of a bridge acoustic sensor is very similar to the case of the cantilever. Taking an uniform pressure load P(t), the in-plane strain in the piezoelectric thin film along the 1-axis, in the limit of a thin PZT film ($h_p << h_{Si}$), is given by equation (5.7) [14].

$$\xi_1(x) = \frac{L^2}{2 \cdot E_{Si} \cdot h_{Si}^2} \cdot \left[1 - \frac{6x}{L} + \frac{6x^2}{L^2}\right] \cdot P(t) \tag{5.7}$$

where h_{Si} is the bridge thickness, E_{Si} the silicon's Young modulus, L the length of the bridge and $P(t) = P_0 e^{i\omega t}$ the amplitude of the photoacoustic pressure modulation.

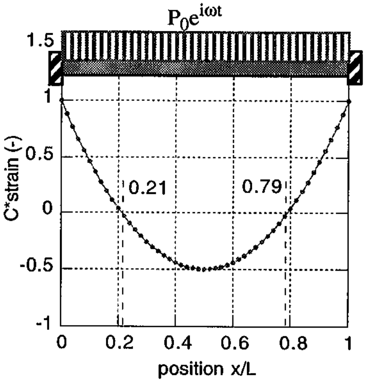

Figure 5.6: Mechanical strain profile in PZT/Si bridge loaded with uniform pressure excitation $P_0e^{i\omega t}$.

Figure 5.6 shows the strain as a function of the relative position x/L. One see that the sign is changing at x=0.21*L and x=0.79*L. To collect charges of same sign, the top electrode has been positioned in the two intervals: [0; 0.21*L] and [0.79*L; L]. The charge and the current response are then measured by summing the charge density $D_3(x)$ into the two intervals.

$$Q(t) = 0.096 \cdot e_{31,f} \frac{(1-\upsilon)w_{el}}{E} \cdot \frac{L^3}{h_{Si}^2} \cdot P(t) \tag{5.8}$$

$$J(t) = 0.096 \cdot e_{31,f} \frac{(1-\upsilon)w_{el}}{E} \cdot \frac{L^3}{h_{Si}^2} \cdot i\omega \cdot P(t) \tag{5.9}$$

For comparison, the sensitivity of a bridge of same thickness is about 9 times lower than the sensitivity of the cantilever design. To obtain the same sensitivity, the thickness of the structure has to be reduced by a factor 3 or the length multiplied by a factor 2. The bridge design offers two advantages: it is less sensitive to residual stress than cantilevers and the air conductance of the slit is reduced by 1/3. Lower working frequencies can be achieved.

For a 2 mm bridge, 10 μm thick, a sensitivity of 1.1 pC/Pa or 67 pA/Pa @ 10 Hz is expected. The resonance frequency of such structures is well above 20 kHz.

5.2.4 Frequency response of gradient pressure sensor

In partially unclamped pressure sensors (either bridge or cantilever), the presence of a slit around the structure influences strongly the sensitivity at low frequency. It depends directly of the pressure gradient between the two sides of the device (see Figure 5.7). It is thus necessary to minimize the air leak to the so-called damping volume on the rear side (about 1 cm^3, defined by the packaging). Flat structures and very narrow slits are thus mandatory.

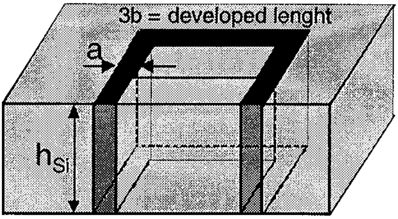

*Figure 5.7: Slit geometry around a bxb cantilever. The slit dimensions are: width = a, developed length = 3*b, height = h_{Si}*

The airflow through the microslit depends of many parameters as the size of the slit itself, the aspect ratio (width * developed length), the surface roughness and the flow regime (viscous/molecular and laminar/turbulent). Indeed, for large slits, the viscous interactions between the gas molecules within the slit are predominant. But as the size of the slit is approaching the micrometer, there are less than less molecules flying in the gap and the elastic interactions are the relevant phenomenon. The latter situation is comparable to what happens in vacuum systems.

A) Air flow in microslits

To evaluate the flow in the slit, it is necessary to introduce an equivalent hydraulic diameter as defined by:

$$D_H = \frac{4 \cdot A}{L_w} \cong 2a \tag{5.10}$$

where: A = slit cross-section = 3*b*a in μm^2.

L_w = wetted perimeter ≈ 2*3*b in μm.

Taking b = 2 mm (2x2 mm cantilever) and a slit width of a = 5 μm, we calculated D_H = 10 μm. The molecular interactions within the slit are given by the ratio between the air mean free path and the equivalent dimension of the slit, D_H. This ratio is called the Knudsen number as defined by:

$$Kn = \frac{\lambda}{D_H} \tag{5.11}$$

where: λ = 0.065 μm = mean free path of air at 273 °K and 10^5 Pa.

D_H = hydraulic diameter in μm.

Three cases of figure can be considered. If $Kn < 0.01$, the regime is viscous and the gas flow is limited by its viscosity. This particular case occurs with the cantilever microphones (with 5 μm slit, D_H = 10 μm: Kn = 0.0065). If $Kn > 0.5$, the regime is molecular. This case is found when the gas mean free path is much larger than the pipe diameter or the vacuum enclosure. Between Kn = 0.01 to 0.5, the regime is transitional and the gas flow is governed by viscosity and molecular phenomena. With cantilever microphones, the transition with the viscous regime ($Kn < 0.01$) is found with $a > 3.25$ μm ($D_H > 6.5$ μm) and the molecular regime ($Kn > 0.5$) occurs for $a < 0.05$ μm ($D_H < 0.13$ μm).

In the range where the state of the gas is viscous, the flow can be turbulent or laminar. The Reynolds number defines the limit between the turbulent and the laminar flow:

$$Re = \frac{\rho \cdot u \cdot D_H}{\eta} \tag{5.12}$$

where: ρ = 1.29 kg/m^3, the gas density at 10^5 Pa, 25°C.

u = air velocity through the slit (m/s).

D_H = 10 μm, the hydraulic diameter of the slit.

$\eta = 1.8 \cdot 10^{-5}$ kg/m s, the air viscosity at 25°C.

If $Re > 2100$, the flow is entirely turbulent, while for $Re < 1100$, it is entirely laminar. The exact limit depends upon many parameters such as the roughness of the slit and other experimental factors. According to Bernoulli equation, the air speed through the slit is estimated to 1.2 m/s for a pressure difference of 1 Pa (note that in photoacoustic cells, the pressure amplitude is often less than 100 mPa). The corresponding Reynolds number gives 0.88. The airflow between the photoacoustic cell (V_1) and the damping volume (V_2) is governed by the conductance of the slit of the microphone. Based on the assumption of a viscous and laminar flow, the air conductance of a rectangular cross section can be calculated by the relation given by Heinze [15] and Holland [16]:

$$C = \frac{1}{12}\cdot\frac{a^3 b}{\eta}\cdot\frac{\bar{P}}{h_{Si}} \tag{5.13}$$

where a and b are the section dimensions ($b >> a$), h_{Si} the height of the slit (equal to the cantilever thickness), $\eta = 1.8\ 10^{-5}$ kg/m s, the air viscosity and $\bar{P} \approx P_{atm}$, the average air pressure.

B) Sensitivity of gradient microphone

The sensitivity of the gradient microphone is function of the number of molecules flowing from the photoacoustic cell V_1, through the slit, to the damping volume V_2 during one modulation.

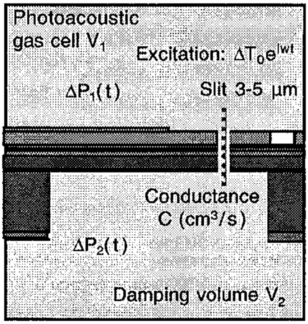

Figure 5.8: Air flow in gradient pressure microphone. The sensitivity is function of [$\Delta P_1(t)$-$\Delta P_2(t)$].

Assuming a temperature modulation $\Delta T_0 e^{i\omega t}$ of the gas in the photoacoustic cell (volume V_1), the amount of molecules that leave V_1 to keep the equilibrium is given by:

$$\Delta N_1(t) = \frac{V_1 \Delta P_1(t) - V_1 \bar{P} \cdot \dfrac{\Delta T_0 e^{i\omega t}}{T_m}}{k_B(T_m + \Delta T_0 e^{i\omega t})} \tag{5.14}$$

where $\Delta P_1(t)$ is the pressure variation in V_1, $\bar{P} = 100000$ Pa, the atmospheric pressure and $k_B = 1.38e{-}23$ J/K, the Boltzman constant.

Meanwhile, in the damping volume V_2 where a constant temperature T_m is assumed, we can write:

$$\Delta N_2(t) = \frac{V_2 \cdot \Delta P_2(t)}{k_B T_m} \tag{5.15}$$

where $\Delta P_2(t)$ is the pressure variation in the damping volume V_2. The conservation of the total number of molecules yields:

$$\Delta N_1(t) + \Delta N_2(t) = 0. \tag{5.16}$$

Introducing Equations (5.14) and (5.15) in (5.16), $\Delta P_2(t)$ can be derived as a function of $\Delta P_1(t)$.

The flow of molecules entering the damping volume V_2 due to the photoacoustic modulation into the photoacoustic cell V_1 is driven by the conductance of the slit:

$$\Delta N_2'(t) = \frac{1}{k_B T_m} \cdot C \cdot [\Delta P_1(t) - \Delta P_2(t)] \tag{5.17}$$

Rearranging Equations (5.14), (5.15) and (5.17), a differential equation for $\Delta P_2(t)$ is obtained. The solution is complex and is given by:

$$\Delta P_2(t) = e^{-\left[\frac{C \cdot \Delta T_0 e^{i\omega t}}{i\omega \cdot V_1 T_m} + \frac{C \cdot (V_1 + V_2)}{V_1 V_2} \cdot \omega\right]} \cdot \frac{C \cdot \bar{P} \cdot \Delta T_0}{V_2 T_m} \cdot \int_t U(t)dt \tag{5.18}$$

where:

$$U(t) = e^{\frac{C \cdot (V_1 + V_2)}{V_1 V_2} \cdot t + i\omega t + \frac{C \cdot \Delta T0 e^{i\omega t}}{i\omega \cdot V_1 T_m}} \tag{5.19}$$

Knowing $\Delta P_2(t)$, $\Delta P_1(t)$ can be calculated as well as the sensitivity $S(\omega, t) = [\Delta P_1(t) - \Delta P_2(t)]$ of the microphone. In this model, it was firstly assumed a fixed temperature modulation of the gas $\Delta T_0 e^{i\omega t}$ in the photoacoustic cell V_1. This temperature modulation originated from the heat absorption of the gas. In that case, the influence of the air leak of the microphone in the calculation of the acoustic modulation was integrated in the model. Similar results can be obtained by assuming directly a pressure modulation $\Delta P_0 e^{i\omega t}$ for the photoacoustic signal. In that case, the sensitivity of the microphone is formulated by:

$$S(\omega) = \frac{1}{V_1} \cdot \left[\frac{i\omega}{\frac{C \cdot (V_1 + V_2)}{V_1 V_2} + i\omega} \right] \tag{5.20}$$

The relative sensitivity of the microphone is obtained by the sensitivity given by equation (5.20) divided by the sensitivity at high frequency S_0. Numerical simulations have shown that for a typical thermal excitation of 0.02°C at 300 °K and $\bar{P}$ = 100'000 Pa with $V_1 = V_2 = 1$ cm^3 and C = 7.5 cm^3/s, the deviation between the two models was inferior to 0.4%.

With a 5 μm slit around a 10 μm thick 2x2 mm cantilever, the calculated conductance according to equation (5.13) is 34.7 cm^3/s. Figure 5.9 shows that at 10 Hz, about 55 % of the photoacoustic signal is lost through the slit of the microphone. With 3 μm slit, the calculated conductance is 7.5 cm^3/s and only 5.4 % of the photoacoustic signal is lost at 10 Hz.

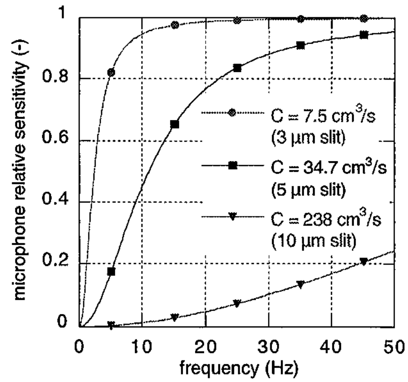

Figure 5.9: Simulation of the relative sensitivity of a gradient microphone for different slit conductance C (cm^3/s).

Table 5.1 summarizes the relative sensitivity at 10 and 20 Hz, the air conductance and the frequency at which $S(\omega) = 0.5$ and 0.8 for 3, 5 and 10 μm slits connected to a damping volume V_2 of 1 cm^3. It shows that very narrow slits of 3 to 5 μm are mandatory to achieve a reasonable sensitivity between 10 and 20 Hz

Table 5.1: Relative sensitivity as a function of slit width for 2x2 mm cantilever, 10 μm thick

slit width (μm)	sensitivity S/S_0 @ 10 Hz, (-)	sensitivity S/S_0 @ 20 Hz, (-)	conductance (cm^3/s)	cutting freq. $S/S_0 = 0.5$ (Hz)	frequency $S/S_0 = 0.8$ (Hz)
3	0.946	0.986	7.5	2.4	4.85
5	0.45	0.766	34.7	11.1	22.3
10	0.013	0.049	278	88.5	177

Let's now consider the simplest case where the volume V_1 is much larger than V_2 ($V_1 >> V_2$). This case is encountered when the front side volume is infinite and the backside volume (or damping volume) is defined by the packaging of the sensor electronics (usually, $V_2 \approx 1\ cm^3$). The frequency response of the sensitivity is thus given by:

$$S(\omega) = \frac{S_0}{\frac{C^2}{V_2^2} \cdot \frac{1}{4\pi^2 f^2} + 1} \tag{5.21}$$

The filling time τ of the damping volume and the cutting frequency f_c, which corresponds to a sensitivity of 0.5 are given by:

$$\tau = \frac{1}{\omega_c} = \frac{C}{V_2} \tag{5.22}$$

$$f_c = \frac{C}{2\pi \cdot V_2} \tag{5.23}$$

$$S(\omega_c) = \frac{S_0}{2} \tag{5.24}$$

The derivation of theoretical models for piezoelectric cantilever and bridge gradient microphones has shown the importance of etching very narrow slits around the structures. Indeed, slits of 3 to 5 μm are mandatory to obtain devices with sufficient sensitivity at low frequency. This shows also the importance to avoid any residual bending of the PZT/Si structures to keep the air conductance as low as possible.

5.3 MICROFABRICATION SPECIFIC ISSUES

The device microfabrication has been carried out using the standard process flow presented in chapter 4. Figure 5.10 shows a detail of a 4" wafer with cantilevers and bridges acoustic sensors (see Figure 5.11 and 5.12) and test structures for the measurement of the transverse piezoelectric coefficient $e_{31,f}$. On wafer #1202, dielectric constant of 1096, loss factor of 3.3% and $e_{31,f}$ of -12.8 ± 0.5 C/m^2 have been measured, showing that the microfabrication process did not affect the functional properties of the piezoelectric film.

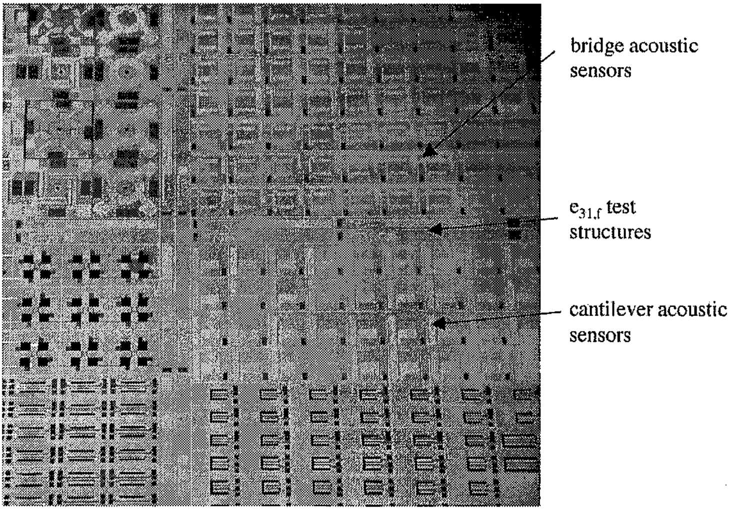

bridge acoustic sensors

$e_{31,f}$ test structures

cantilever acoustic sensors

Figure 5.10: Top view of 4" wafer with acoustic sensors and $e_{31,f}$ test structures

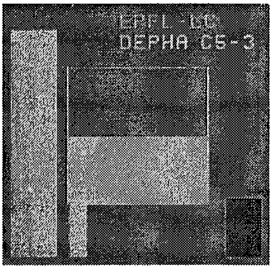

Figure 5.11: Cantilever acoustic sensor C5-3, wafer #1202, slit 5 μm.

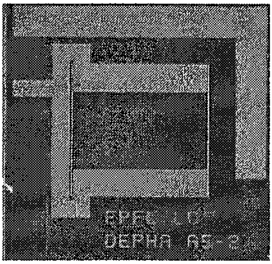

Figure 5.12: Bridge acoustic sensor A5-2, wafer #1202, slit 5 μm.

5.3.1 Stress compensation

As to the cantilever microphone, one of the first concerns was that film stress would bend the cantilever so much as the latter would be deflected out of the plane of the device frame, leading to too large gas conductivity and small response at low frequencies. The stress compensation developed in chapter 4 has been successfully applied. PZT tensile stress has been compensated by compressive SiO_2 thin film. The effect of poling has been taken into account as well. Figure 5.13 and Figure 5.14 show the 3D topography and the cross-section of the middle line of a 2x2 mm^2 PZT/Si cantilever before and after poling, as measured by means of a scanning laser microscope (UBM).

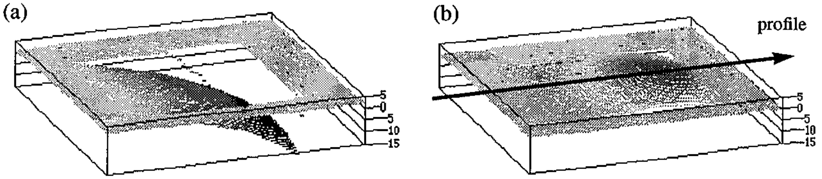

Figure 5.13: 3D topography of 2x2 mm^2 cantilever acoustic sensor C3-1 (a) before poling, (b) after poling. SiO_2 stress compensation layer is 1200 nm thick.

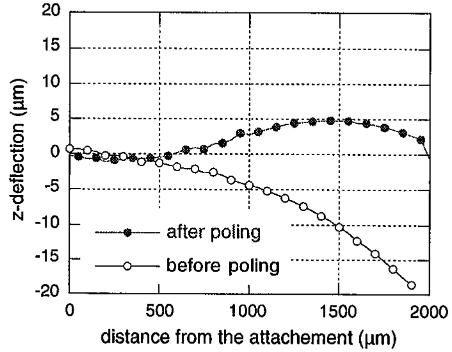

Figure 5.14: Deflection profile in the middle of the cantilever C3-1 before and after poling of the piezoelectric thin film.

Before poling, a tip deflection of about –18 µm has been measured. After poling (250 kV/cm, 10 min, 150°C), the cantilever becomes almost flat with a small bow of +5 µm in the center. This residual deflection represents only 0.25% of the cantilever length and corresponds to a residual stress of about 5 MPa in 1 μm film deposited on 10 μm thick silicon cantilever. This shows that the compensation of PZT stress by adjusting the thickness of underlying SiO_2 layer was successful. With 2x2 mm cantilever, the total error on the stress measurement (about 34 MPa) remains the limiting factor to obtain more balanced structures (10 μm tip deflection on 2x2 mm^2 cantilever is already obtained with 10 MPa residual stress).

5.3.2 Patterning of 3-10 μm slits by dry etching

For cantilever and bridge, slits of 3, 5 and 10 μm have been patterned. All dry etching process, including dry etching of PZT and platinum has been used. Figure 5.15 to Figure 5.17 show SEM images of 3, 5 and 10 μm slit through the PZT / Pt / SiO_2 / Si stack.

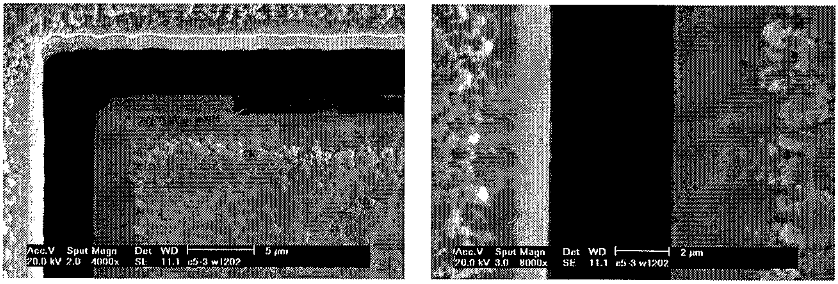

Figure 5.15: SEM images of - left: 5 μm slit corner - right: zoom of 5 μm slit etched through PZT/Pt/SiO_2/Si. Real slit width = 4.4 μm.

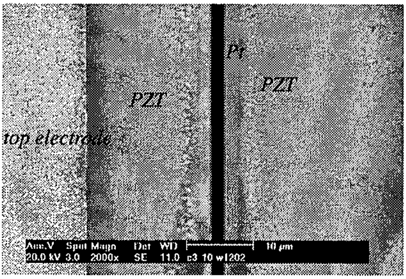

Figure 5.16: SEM top view image of a 3 μm slit etched through PZT/Pt/SiO_2/Si. Top width = 2 μm.

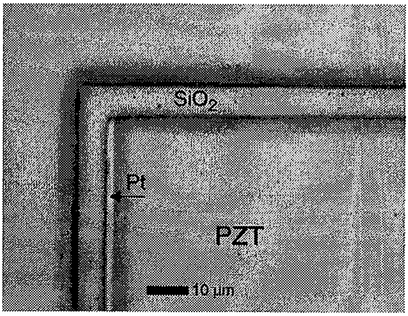

Figure 5.17: Optical image of 10 μm slit dry etched through PZT/Pt. 1 μm alignment error between PZT and Pt mask is observed.

At the end of the dry etching processes, the trench width was found to be slightly shrinked due to the instability of the photoresist. For 5 and 3 µm slits the top dimension of platinum trench are thus 4.4 and 2 µm respectively. However, below the platinum electrode, the internal width of the slit is slightly larger (about + 0.5 µm) due to silicon underetching.

5.3.3 Electronics and packaging

To take advantage of small signals or noisy environment, the integration of the read-out electronics (transistors) on the same silicon substrate than the micromechanical sensors would be an advantage and has been often studied, in particular with piezoresistive and electrostatic devices [17]. However, with piezoelectric devices, the hybrid integration (electronics on a separated printed board) has to be chosen as the crystallization conditions of PZT thin films (650°C in oxygen) are mostly incompatible as a post-processing of IC's processes. In this thesis, the piezoelectric microphone has been bonded directly on the printed circuit board (PCB) of the charge amplifier (SMD components). Hybrid integration allows faster re-design of the devices, the separation of electronics and device parts and much lower microfabrication complexity.

A piezoelectric sensor is modeled as a charge source with a shunt capacitor and resistor as shown in Figure 5.18. Because of the high dielectric constant of PZT ($\varepsilon_r > 1000$), current detection has been chosen. The current amplification is also better suited when amplification is remote to the sensor [18].

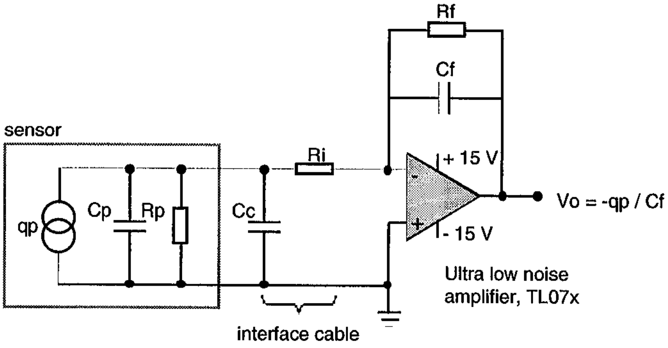

Figure 5.18: Electrical circuit of a charge amplifier with ultra low noise op amp TL07x

The charge amplifier balances the charge injected into the negative input by charging the feedback capacitor C_f. The resistor R_f bleeds the charge off capacitor C_f at a low rate to prevent the amplifier from drifting into saturation. The resistor R_f also provides a dc bias path for the negative input. The transfer function of the amplifier is given by:

$$V(t) = \frac{A}{C_f + \frac{1}{i\omega R_f C_f}} \cdot P_0 e^{i\omega t} \tag{5.25}$$

where A depends on the beam geometry and on the piezoelectric coefficient, C_f and R_f are the feedback capacitor and resistor and ω the modulation frequency. When ω is large, the transfer function is simply given by:

$$V(t) = \frac{A}{C_f} \cdot P_0 e^{i\omega t} \tag{5.26}$$

The value of C_f and R_f set the low cutoff frequency of the amplifier. The action of the amplifier maintains 0 V across its input terminals so that the stray capacitance associated with the interface cabling does not present a problem. C_c and R_i are the capacitance and the internal resistance of the cable interface. The frequency response of such charge amplifier is showed in Figure 5.19. With a generated charge of about 1-10 pC, a very low C_f capacitance (10 - 100 pF) is required to obtain an output signal level of few volts. As the working frequencies of photoacoustic gas detectors are ranging from 10 to 50 Hz, high value of the resistance R_f (GΩ range) is required to shift the cut-off frequency f_L below 5 Hz for instance.

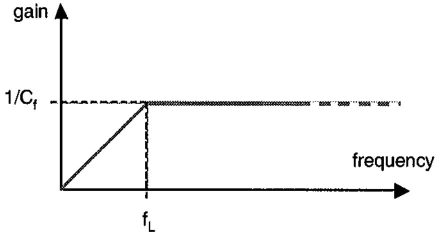

$$f_L = \frac{1}{2\pi R_f C_f}$$

Figure 5.19: Frequency response of charge amplifier at low frequency. The f_L cut-off frequency is defined by the feedback R_f and C_f

After the polarization of the PZT film, the sensor is glued on the PCB (see Figure 5.20) of a calibrated SMD charge amplifier ($C_f = 10$ pF, $R_f = 10$ GΩ, $f_L = 1.6$ Hz). The metal cup on the rear side defines a 0.7 cm^3 damping volume (see Figure 5.21).

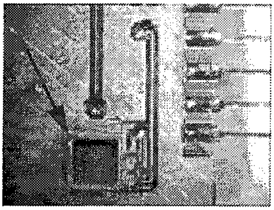

Figure 5.20: Cantilever acoustic sensor glued on the PCB of the SMD charge amplifier.

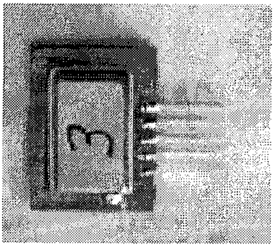

Figure 5.21: Backside of the SMD charge amplifier. The metal cap defines the damping volume.

5.4 ACOUSTIC SENSORS CHARACTERIZATION

5.4.1 Experimental methods

The sensitivity and the frequency response of the acoustic sensors have been measured in a sealed box where a pressure excitation is generated by a loudspeaker. The sensor sensitivity is obtained by comparison with the signal given by a reference microphone (Panasonic WM-034DBU, [19]) and corrected with respect to the frequency response of the charge amplifier.

Real geometrical dimensions of the devices have been measured using scanning electron microscope (SEM) Philips XL30 (Eindhoven, Holland). Non-destructive measurements of the structure thickness (cantilever or bridge) have been obtained by means of their resonance frequency and the model depicted in chapter 4 for the resonance frequency of a PZT/Si multilayer.

5.4.2 Sensitivity and frequency response of cantilever acoustic sensor

Silicon thickness of the cantilever and geometrical dimensions of the slit surrounding the structure have been found to be the key factors driving the device response. As high sensitivity is obtained with thin structures, narrow microslits are requested to provide sufficient sensitivity a low frequency. The aim of this section is to characterize cantilever acoustic sensors with respect to their maximal sensitivity (given by the pure piezoelectric model) and with respect to their frequency response (given by the air conductance model). Influence of cantilever thickness, slit width and damping volume is presented.

A) Cantilever with 5 μm slit

Figure 5.22 shows the frequency response of 2x2 mm cantilever acoustic sensor C5-3 with nominal 5 μm slit as a function of the damping volume. Above 30 Hz, the device exhibits a high sensitivity of 170 mV/Pa. Measurement of the device resonance frequency gives the thickness of the cantilever which amounts to 17 ± 1 μm. Taking equation (5.6), a theoretical sensitivity of 308 mV/Pa (with 10 pF charge amplifier) is calculated. It is thought that the difference may originate from two aspects. First, the air friction within the slit damps the cantilever movement and thus decreases the sensitivity. Second, due to the deep silicon etching process, the silicon thickness of the cantilever is not uniform. As in microcantilevers (chapter 4), the beam is usually thicker near the attachment point and thus, where the strain (and the generated electrical charges) should be maximal. Quantitative predictions are thus rather difficult as the control of the geometry of the cantilever is difficult to achieve. With respect to frequency, the 1/(1+1/f) behavior predicted by the device physics has been observed. The sensitivity is decreasing rapidly at low frequency due to the air leak flowing through the slit.

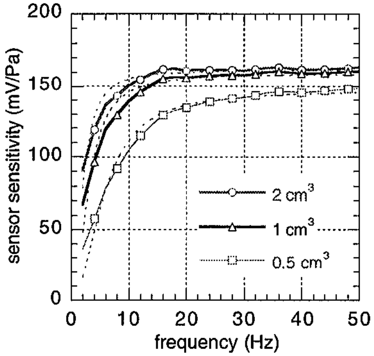

Figure 5.22: Frequency response of 2x2 mm^2 cantilever with 5 μm slit (top dimension on Pt film is = 4.2 μm) and fit using equation (5.21). Cantilever thickness is 17 ± 1 μm

By increasing the damping volume, the time required to balance the pressures increases as well and the cut-off frequency ($0.5*S_0$) is shifted to lower values. With $V_2 = 2$ cm^3, it amounts to about 2.04 Hz compared to 5.67 Hz for 0.5 cm^3. Table 5.2 summarizes the conductance of the slit C (cm^3/s) and the sensitivity at high frequency S_0 (mV/Pa) obtained by fitting equation (5.21) on experimental curves.

Table 5.2: Conductance and sensitivity of cantilever acoustic sensor, slit = 5 μm

Damping vol. V_2 (cm^3)	Sensitivity S_0 (mV/Pa)	Conductance C (cm^3/s)	Calculated cut-off freq.(Hz)	Corr. factor (-)
2	162 ± 1	25.6 ± 1	2.04	0.97
1	159 ± 2	18.9 ± 0.9	3	0.97
0.5	147 ± 2	17.8 ± 1.5	5.67	0.98

It can be seen on Figure 5.15 that the width of the trench defined by the bottom electrode is smaller (4.4 ± 0.2 μm) than the designed dimension (5 μm). This is due to photoresist instability during dry etching processes (PZT/Pt/SiO_2). Taking the cantilever silicon thickness measured by means of the resonance frequency in vacuum (17 ± 1 μm) into the equation of Holland (5.13) gives a conductance of about 14 cm^3/s, which match well the measured values (approximately 18 cm^3/s).

B) Cantilever sensor with 3 μm slit

With 3 μm slits, the frequency response becomes more flat as the air leak flowing through the slit is reduced by a lower conductance. Figure 5.23 shows the sensitivity of sensor C3-8 as a function of excitation frequency. Maximal sensitivity of 94 mV/Pa has been measured. Theoretical value calculated with 15 μm thick silicon structure gives 430 mV/Pa (10 pF charge amplifier). Table 5.3 summarizes fitted conductance values as well as cut-off frequencies and maximal sensitivity as a function of the damping volume.

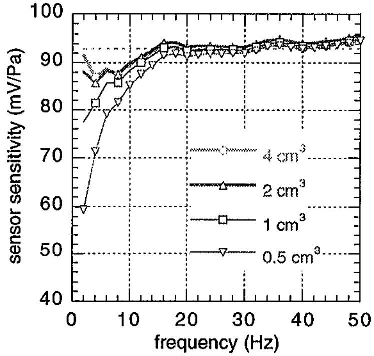

Figure 5.23: Frequency response of 2x2 mm^2 cantilever with 3 μm slit (real dimension = 2 μm) and fit using equation (5.21). Cantilever thickness is 15 ± 1 μm

Table 5.3: Conductance and sensitivity of cantilever acoustic sensor, slit = 3 μm

Damping vol. V_2 (cm^3)	Sensitivity S_0 (mV/Pa)	Conductance C (cm^3/s)	Calculated cut-off freq.(Hz)	Corr. factor (-)
4	set 93	N/A	N/A	N/A
2	set 93	N/A	N/A	N/A
1	92.6 ± 0.5	6.3 ± 0.5	1	0.84
0.5	92 ± 0.7	5.4 ± 0.3	1.72	0.93

In this case, the fitting of equation (5.21) is more difficult due to the rapid change of the sensitivity at low frequency (< 5 Hz). However, it was possible to extract the slit conductance C from the curves measured with V_2 = 0.5 and 1 cm^3. 5.4 and 6.3 cm^3/s have been obtained respectively. These values are well in accordance with the calculated one: 5 cm^3/s using a slit width of 3 μm by 15 μm thick. Even with a small damping volume of about 0.5 cm^3 (close to the real packaging), about 90% of the maximal sensitivity S_0 is already achieved at 10 Hz. Microstructuration of 3 μm slits around PZT/Si cantilever is thus necessary to make sensitive acoustic sensor for integration into photoacoustic gas detector.

C) Cantilever acoustic sensor with 10 μm slit

Finally, the frequency response of a device with 10 μm slit (C10-9) is showed in Figure 5.24. The sensitivity at high frequency tends to about 250 mV/Pa and a slit conductance of about

100 cm^3/s has been measured (see Table 5.4).

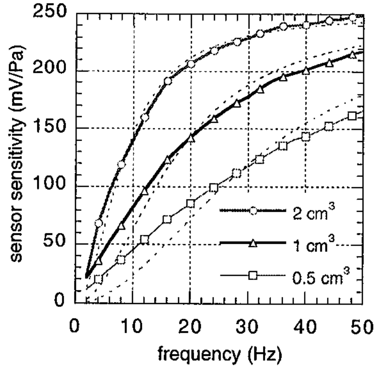

Figure 5.24: Frequency response of 2x2 mm^2 cantilever with 10 μm slit (real = 9.2 μm) and fit using equation (5.21). Cantilever thickness is 12 ± 1 μm

Table 5.4: Conductance and sensitivity of cantilever acoustic sensor, slit = 10 μm

Damping vol. V_2 (cm^3)	Sensitivity S_0 (mV/Pa)	Conductance C (cm^3/s)	Calculated cut-off freq.(Hz)	Corr. factor (-)
2	set 250	106.5 ± 2.3	8.5	0.99
1	set 250	108.2 ± 3.1	17.2	0.98
0.5	set 250	98.2 ± 2.8	31.3	0.95

Using silicon thickness of 12 ± 1 μm and real slit dimension of about 8 μm, a slit conductance of 118 cm^3/s can be calculated. Here again, the measured value is close to the calculated one. With respect to frequency response, cantilever with 10 μm slit exhibits too high air conductance to be used below 20 Hz.

5.4.3 Sensitivity and frequency response of bridge acoustic sensors

A) Bridge acoustic sensor with 5 μm slit

Similar results than with cantilevers have been obtained with bridge acoustic sensors. Figure 5.25 shows the frequency response of 2.5 x 2 mm bridge with nominal 5 μm slit. The conductance of the slit amounted to 7.4 cm^3/s. The calculation according to Holland, taking h_{Si}

= 9.6 μm and a = 4.4 μm yields C = 21 cm^3/s. As for the cantilever C5-3, this calculated value is close to the experimental ones (29 - 36 cm^3/s).

The maximal sensitivity of the bridge is 50.8 mV/Pa. Calculation of the theoretical value according to equation (5.8) yields 225 mV/Pa (with 10 pF charge amplifier), about four times higher than the measured response. Table 5.5 shows the conductance of the slit C (cm^3/s) and the sensitivity at high frequency S_0 (mV/Pa) calculated by fitting equation (5.21) on the experimental data.

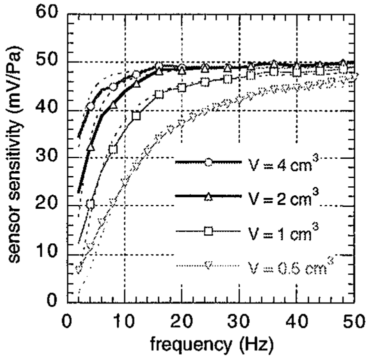

Figure 5.25: Frequency response of 2.5 mm bridge B5-13 with 5 μm slit (real = 4.4 μm). Bridge thickness is 9.6 μm

Table 5.5: Conductance and sensitivity of bridge acoustic sensor B5-13, slit = 5 μm

Damping vol. V_2 (cm^3)	Sensitivity S_0 (mV/Pa)	Conductance C (cm^3/s)	Calculated cut-off freq.(Hz)	Corr. factor (-)
4	49 ± 0.2	36 ± 0.4	1.43	0.95
2	49.2 ± 0.4	33.3 ± 1.5	2.65	0.97
1	48.3 ± 0.4	32.8 ± 1.4	5.22	0.99
0.5	46.7 ± 0.6	29 ± 1.1	9.24	0.99

B) Bridge acoustic sensor with 3 μm slit

Bridge acoustic sensor with 3 μm slit has been characterized as well. The frequency response is given in Figure 5.26. This device has about the same silicon thickness than the previous bridge B5-13. 11 μm has been measured by means of the resonance frequency and similar maximal sensitivity is also observed. However, in this, case, one has reach a limit in conductance where, for damping volumes ranging from 0.5 to 4 cm^3, the frequency response above 2 Hz is flat. In case of cantilevers, this very interesting feature was only approached with large damping volume ($V_2 > 4$ cm^3).

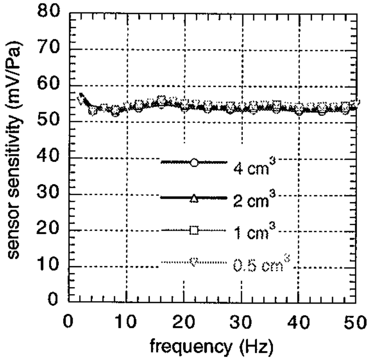

Figure 5.26: Frequency response of 2.5 mm bridge with 3 μm slit (real = 2 μm). Bridge thickness is 11 μm

According to Holland, the theoretical conductance is about 1.7 cm^3/s. For the smallest damping volume (0.5 cm^3), this would yield a cut-off frequency ($0.5*S_0$) of only 0.5 Hz.

5.4.4 Concluding remarks on device sensitivity and slit conductance

With respect to the maximal sensitivity, it was difficult to stress a trend explaining the difference (usually more than 30%) between theoretical and measured values. Indeed, many parameters as the cantilever thickness uniformity, the dimension of the slit (air damping) or even dust particles within the slit (friction points) may play an important role.

The equation (5.13) giving the slit conductance as of function of geometrical parameters of the trench can be modified as $(C*t/b) = (P/12*\eta) * a^3$. If the air conductance through the rectangular microslit follows this law, a linear behavior should be obtained. The results are shown in Figure 5.27 where the product ($C*t/b$) is expressed as a function of real a^3 for all devices previously presented (cantilevers and bridge)

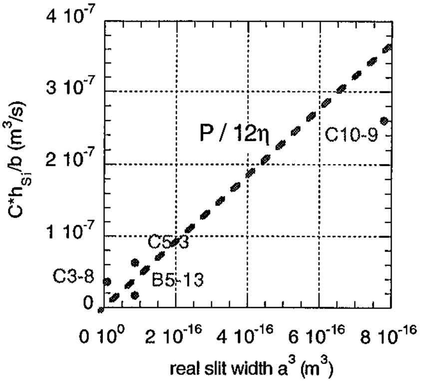

Figure 5.27: Measured C^*h_{Si}/b factor as a function of real slit width a^3 compared to nominal value $P/12\eta$ given by equation (5.13).

Apart the point related to device C10-9 with a conductance lower than expected, the experimental values fit well with the theoretical slope defined by $P/12\eta$ (using $P = 100000$ Pa and $\eta = 1.8*10^{-5}$ Nm). This shows that the calculation of the slit conductance using Holland's model was appropriate. However, better prediction and better matching with theoretical values remains difficult to achieve as the real conductance depends strongly on many experimental factors such as the real internal slit geometry, the wall roughness, the walls convergence, non-uniformities in silicon thickness and even, on eventual residual silicon particles within the slit.

Partially unclamped microphones with 3 and 5 μm slits have found to be very useful as acoustic sensors for low frequency applications. In particular, 3 μm slits yields almost flat frequency response above 2-3 Hz, which is excellent with respect to the target application (photoacoustic gas detector with working frequency of 10-20 Hz). Compared to cantilevers, bridge acoustic sensors yields absolute in-plane structures. The residual bending is lower and thus, the air conductance is easier to control. Finally, to obtain better precision and correspondence with the modelization, silicon structures with very well defined geometry should be fabricated using SOI substrates.

5.5 INTEGRATION OF PIEZOELECTRIC CANTILEVER MICROPHONE INTO MINIATURE PHOTOACOUSTIC CO_2 GAS DETECTOR

5.5.1 Experimental methods - miniature photoacoustic gas cell

The cantilever acoustic sensor has been packaged on a small PCB charge amplifier (see section 5.3.3) and fixed on a photoacoustic cell in aluminum (ø 8 x 15 mm, $V_l = 0.7$ cm^3). The gas feed is realized through a semi-permeable Gore-Tex^{TM} membrane. The IR emission is generated by a miniaturized IR source from M. Weber (IMS-EPFL) made out of Pt thin film meander deposited on micromachined membrane [8]. The selection of the absorption wavelength is assumed by an interference IR filter, at 4.25 µm for CO_2.

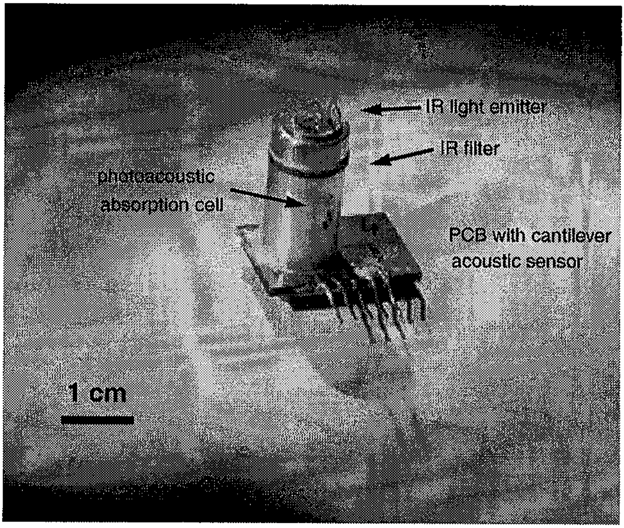

Figure 5.28: Picture of miniature photoacoustic gas detector with cantilever acoustic sensor integrated on PCB charge amplifier.

The IR source is modulated at 20 Hz with a 0-5 V_{pp} square waveform. The acoustic signal is detected by a spectrum analyzer from Stanford Research (i760) with a measuring range of 0 - 97.5 Hz and a sampling frequency of 0.244 Hz. The output is recorded in V_{pp}. Various CO_2 concentrations have been obtained by dilution of pure CO_2 in air. The following concentrations have been prepared: pure nitrogen N_2 (0 ppm), air (330 ppm), 1000 ppm, 2000 ppm, 5000 ppm, 10000 ppm, 20000 ppm and 50000 ppm of CO_2.

5.5.2 Photoacoustic signal detected by piezoelectric cantilever microphone

Figure 5.29 shows the frequency spectrum of the photoacoustic signal of 2000 ppm CO_2 detected by the piezoelectric cantilever acoustic sensor C5-7. The photoacoustic peak is clearly visible at 20 Hz out of the noise background. For 2000 ppm, a photoacoustic signal of 540 μV has been measured. The noise level is estimated to 180 μV.

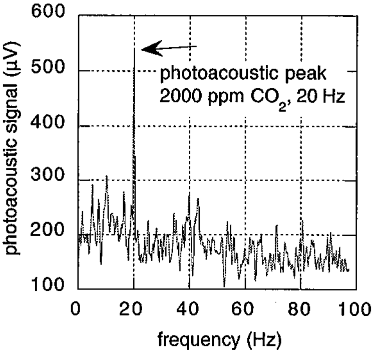

Figure 5.29: Frequency spectrum of the photoacoustic signal generated by 2000 ppm of CO_2 and measured by piezoelectric cantilever acoustic sensor C5-7.

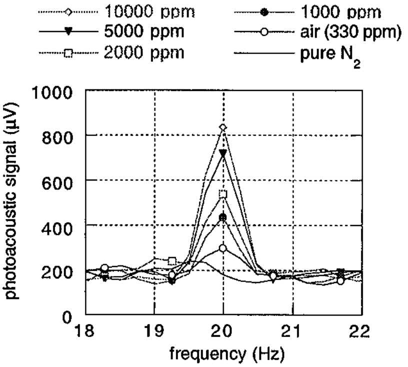

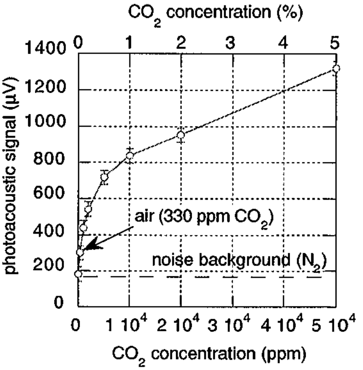

Figure 5.30: 20 Hz peak of the photoacoustic signal as a function of CO_2 concentration.

Figure 5.31: Magnitude of the photoacoustic signal measured at 20 Hz as a function of CO_2 concentration.

Figure 5.30 shows the 20 Hz photoacoustic CO_2 peaks (pressure signal) detected by the piezoelectric cantilever microphone for different CO_2 concentrations. Even in air (330 ppm CO_2), the CO_2 peak can be detected out of the noise background. The magnitude of the photoacoustic peak as a function of CO_2 concentration is summarized in Figure 5.31. Knowing the sensitivity of the piezoelectric cantilever microphone (ref C5-7, S = 46 mV/Pa @ 20 Hz), the measured pressure signal corresponds to pressure amplitude of about 10 - 30 mPa.

5.5.3 Noise level of piezoelectric acoustic sensors

The noise level of piezoelectric acoustic sensors is of a primary importance, as it gives the resolution and the minimal pressure and gas concentration that can be detected. The noise of the piezoelectric cantilever microphone may originate either from dielectric (capacitor), piezoelectric (parasitic vibrations), pyroelectric (variation of the temperature), mechanical-thermal [20] sources or from the charge amplifier itself. First, the dielectric noise (current density) of the piezoelectric thin film can be expressed by:

$$j_{n,\,diel} = \sqrt{4k_BT \cdot \omega C \cdot \tan\delta} \qquad pA/Hz^{0.5} \qquad (5.27)$$

where k_B = 1.38e-23 J/K, T = temperature (°K), $\omega = 2\pi f$ (s^{-1}) = modulation frequency, C = device capacitance (F) and tan δ, the dielectric loss (-). By dividing equation (5.27) by ω, one obtain the dielectric noise expressed in charge density $q_{n,diel}$.

$$q_{n,\,diel} = \frac{j_{n,\,diel}}{\omega} \qquad pC/Hz^{0.5} \qquad (5.28)$$

After charge amplification (with feedback capacitance C_f), the resulting noise (in voltage density) is given by:

$$u_{n,\,diel,\,q} = \frac{q_n}{C_f} \qquad \mu V/Hz^{0.5} \qquad (5.29)$$

If voltage detection is used to measure the sensor response, the dielectric noise is thus directly given by:

$$u_{n,\,diel,\,v} = Z \cdot j_{n,\,diel} = \frac{1}{\omega C} \cdot j_{n,\,diel} \qquad \mu V/Hz^{0.5} \qquad (5.30)$$

where $\omega = 2\pi f$, is the modulation frequency and C = capacitance of the sensor (≈ 20 nF).

The equivalent noise level (voltage density) is then calculated using the device sensitivity S:

$$p_n = \frac{u_{n,\,diel}}{S(\omega)} \tag{5.31}$$

where S(f) is the microphone sensitivity (mV/Pa) at the frequency $f = \omega/2\pi$. For the microphone used here, S = 46 mV/Pa at 20 Hz.

Second, the noise generated by thermally excited (k_BT) oscillations of the cantilever can be estimated using the derivation of Gabrielson [20]. The equality between the mechanical energy stored in the oscillator and the thermal energy is:

$$\frac{1}{2}k\langle x^2\rangle = \frac{1}{2}k_BT \tag{5.32}$$

where k is the spring constant of the device (N/m) given by equation (5.33), T, the temperature and x, the displacement around the equilibrium position.

$$k = \frac{Eh_{Si}^3 w}{4(1-v^2)L^3} \qquad \text{(N/m)} \tag{5.33}$$

The equivalent noise pressure is then calculated by:

$$p_{n,\,mech} = \sqrt{\langle p^2\rangle} = \frac{2k}{wL}\sqrt{\langle x^2\rangle} = \frac{2}{wL}\sqrt{k \cdot k_BT} \qquad \text{(Pa)} \tag{5.34}$$

Finally, the noise from the charge amplifier itself has to be considered. Its contribution to the total noise has been measured by connecting the input of the amplifier to a small resistance of 100 Ω (intrinsic noise of the amplifier) or a capacitance of similar magnitude (20 nF) than the piezoelectric sensor (noise due to the device capacitance).

Table 5.6 summarizes the measured and calculated values for the cantilever C5-7 as well as the noise of the charge amplifier at 20 Hz.

Table 5.6: Measured and calculated noise contributions for cantilever microphone C5-7

	Calculated noise, pp value ($\mu V/Hz^{0.5}$)	Measured noise, pp value ($\mu V/Hz^{0.5}$)	Equivalent pressure level calc. / meas. ($mPa/Hz^{0.5}$)
Charge amplifier, 100 Ω	-	65	- / 1.4
Charge amplifier, 20 nF	-	306	- / 6.7
PZT dielectric noise	36	374*	0.8 / 8.1
Thermal-mechanical noise	5	-	1 / -

* after 10 pF charge amplifier

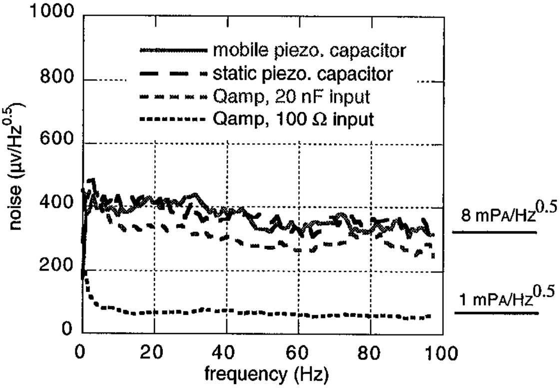

Figure 5.32: Noise spectrum of charge amplifier (100 Ω or 20 nF input) and static and deflecting (cantilever) piezoelectric capacitors.

The noise level of the charge amplifier (65 $\mu V/Hz^{0.5}$) is larger than the calculated dielectric and thermomechanical contributions (41 $\mu V/Hz^{0.5}$). When the piezoelectric capacitor is connected to the charge amplifier, the noise level increases dramatically up to 370 $\mu V/Hz^{0.5}$. Similar value was obtained by connecting a 20 nF foil capacitor ($\tan \delta < 0.9\%$) at the input of the charge amplifier. It turns out that due to the high feedback loop (10 pF and 10 GΩ), the charge amplifier was almost saturated with respect to its frequency*gain product. The noise increased thus dramatically, up to nine times the expected dielectric noise contribution. Redesign of the charge amplifier with FET transistor right on the sensor and multi stage amplification would help achieving simultaneously high gain and much lower noise level.

5.6 SUMMARY

Piezoelectric cantilever and bridge acoustic sensors have been successfully fabricated using the micromachining process flow presented in chapter 4. To address the air leakage at low frequency, very narrow slits (3 - 5 μm) have been patterned around the structures. It was thus possible to take advantage of the high sensitivity of cantilever structures to design acoustic sensors working at low frequencies (10 - 30 Hz). The results of the frequency response have found to follow very well the model developed is this chapter. With 3 μm slit, almost flat frequency response has been measured above 1-2 Hz. The calculation of the air conductance of the slit has been successfully approached using the model of Holland for a rectangular slit in viscous and laminar regime. Fine predictions remain however difficult as the slit conductance depends on many experimental factors such as its exact geometry, the surface roughness within of the walls or the presence of microfabrication residues.

With 10 μm thick structures, device sensitivities larger than 100 mV/Pa have been obtained using 10 pF charge amplifier. The noise level was found to lie around 8 $mPa/Hz^{0.5}$, about nine times higher than the noise expected from dielectric and thermomechanical contributions. It was found that the capacitance of the device and saturated op amp were responsible of such high noise level. The integration of cantilever microphone into the photoacoustic gas detector has been demonstrated. Concentration of CO_2 down to 330 ppm (air) has been detected using miniaturized photoacoustic gas detector. The limit of detection and the detector resolution would be improved after redesign of the charge amplifier.

In this chapter, it has been succesfully demonstrated that piezoelectric cantilever or bridge acoustic sensors offer interesting opportunities in the miniaturization of photoacoustic detectors. To produce reliable acoustic sensors, a very thin bridge with 3 μm slit is probably a promising solution as this structure is less sensitive to residual bending and more stable than a cantilever but still offer an excellent sensitivity at low frequency.

5.7 REFERENCES

1. Bell, A.G., *On the production and reproduction of sound by light.* American Journal of Sciences, 1880. XX(118): p. 305-324.

2. Röntgen, W.C., Philos. Mag., 1881. **11**: p. 308.
3. Tyndall, J. Proc. R. Soc. London, 1881. **31**: p. 307.
4. Pfund, A.H., Science, 1939. **90**: p. 326.
5. Kreuzer, L.B., *Ultralow gas concentration infrared absorption spectroscopy.* J. Appl. Phys., 1971. **42**(7): p. 2934-2943.
6. Oehler, O., et al., *Apparatus for the photoacoustic detection of gases.* 1988, US Patent #4740086: US.
7. Oehler, O., D. Marek, and D. Fries, *A simple photoacoustic gas-detection system.* Helv. Phys. Acta, 1991. **54**: p. 631-636.
8. Weber, M., *Miniature Photoacoustic gas sensor*, in *Microengineering.* 1999, EPFL Thesis n°2075: Lausanne.
9. Kühnel, W. and G. Hess, *Micromachined subminiature condenser microphone in silicon.* Sensors and Actuators A, 1992. **32**: p. 560-564.
10. Ried, R.P., et al. *Residual-stress compensation in clamped-clamped micromachined plates.* in *Micromech. Syst., ASME Winter Annu. Meeting.* 1992. Anaheim (CA).
11. Baborowski, J., et al., *Fabrication and Characterization of Micromachined Accelerometers based on PZT thin films.* Ferroelectrics, 1999. **224**: p. 283-290.
12. Lee, S.S., R.P. Ried, and R.M. White, *Piezoelectric cantilever microphone and microspeaker.* Journal of Microelectromechanical Systems, 1996. **5**(4): p. 238-242.
13. Lee, C., T. Itoh, and T. Suga, *Self-excited piezoelectric PZT microcantilevers for dynamic SFM - with inherent sensing and actuating capabilities.* Sensors and Actuators A, 1999. **72**: p. 179-188.
14. Timoshenko, S. and S. Woinowsky-Kriger, *Theory of plates and shells.* 1959, New-York: McGraw-Hill.
15. Heinze, W., *Einführung in die Vakuumtechnik.* 1955, Berlin: Verlag Technik.
16. Holland, L., W. Steckelmacher, and J. Yarwood, *Vacuum Manual.* 1974, London.
17. French, P.J., *Integration of MEMS devices.* Proc. SPIE, 1999. **3891**: p. 39-48.
18. Karki, J., *Signal conditioning piezoelectric sensors - application report.* Texas Instruments - SLOA033A, 2000. **September**: p. 1-6.
19. Panasonic, *Technical Information for Electret Microphone WM-034DBU.* 1996, Matsushita Communication Industrial Co., Ltd.
20. Gabrielson, B., *Mechanical-Thermal Noise in Micromachined Acoustic and Vibration Sensors.* IEEE Transactions on Electron Devices, 1993. **40**(5): p. 903-909.

CHAPTER 6

FUNDAMENTAL PROPERTIES OF PIEZOELECTRIC MICROMACHINED ULTRASONIC TRANSDUCERS (PMUT'S)

6.1 INTRODUCTION

An ultrasonic transducer is an electronic device that can emit and receive ultrasonic waves. It has numerous applications in underwater sonar detectors, medical ultrasound imaging and non-destructive testing. Since a few years, Micromachined Ultrasonic Transducers (MUT) are investigated for phased arrays in high frequency acoustic imaging to overcome resolution and frequency limits of reticulated bulk $Pb(Zr_xTi_{1-x})O_3$ (PZT) transducers applied today. The basic element consists of a micromachined membrane that is driven by either capacitive (cMUT's) [1] or piezoelectric actuation [2], [3], [4] (pMUT's). The goal of this chapter is to investigate pMUT's with respect to major evaluation criteria's. These are:

- bandwidth
- sensitivity
- achievable pixel density

In bulk ultrasonic transducers, the longitudinal effect (d_{33}) is used and the elements are operated at the $\lambda/2$ thickness resonance (bulk acoustic wave). In micromachined devices, the transverse piezoelectric effect is used to deflect a membrane as well as to sense its deformation. The relevant coefficient is the effective transverse piezoelectric coefficient $e_{31,f}$ defined in chapter 2. As compared to bulk devices, pMUT's exhibit distinct differences:

- The transverse coefficient is 2 times lower than the longitudinal are. This reduce the coupling coefficient k^2, and thus also the bandwidth by a factor 4.
- The pMUT membrane structure is softer than bulk PZT. There is thus a better matching with acoustic impedance of water. Bulk transducers loose a factor 2 in power due to matching problems. Without considering further details, this implies a bandwidth that is a quarter as in bulk PZT transducers, i.e. $k^2 = 15\ \%$ instead of 60%.
- An interesting point is the fact that thin films exhibit much higher breakdown field than bulk material. The smaller amount of piezoelectric material in pMUTs compared to bulk devices can be partially compensated by higher operating field.

One see, there are a number of questions about dimensions, design and operating conditions of such devices.

The pressure created by a deflecting membrane depends on the force of the piezoelectric layer to bend the mechanical structure. This force is proportional to $e_{31,f} * E_3 * t_p = e_{31,f} * V_3$. Considering a limitation in E_3, it is obvious that thicker films (larger t_p) allow for more power. The emitted power can be defined as:

$$P = k^2 \cdot \omega C \cdot U_{rms}^2 = k^2 \cdot \omega C \cdot t_p^2 \cdot E_{rms}^2 \propto k^2 \cdot t_p \cdot E_{rms}^2 \qquad (6.1)$$

which again leads to the conclusion that a thicker film is advantageous if k does not decrease with increasing t_p. On the other hand, frequency and diameter definition limit the usable range of film thickness.

The microfabrication of pMUT's requires a special attention on three major issues:
- Integration of high quality and relatively thick piezoelectric films
- Micromachining of all materials
- Precision to achieve a high density of elements

In chapter 3, we found that {100}-textured PZT 53/47 thin films exhibited the best effective transverse piezoelectric coefficient ($e_{31,f} = -12\ C/m^2$). The ability of the sol-gel process to achieve films up to 4 μm thick is thought to be sufficient to fabricate pMUT's working at higher frequency as compared to the standard 3 MHz.

Apart the piezoelectric thin film integration, the design of basic pMUT's structure has to be considered as well. In particular, the ratio between the PZT film thickness and the silicon structure, the shape of the top electrodes (round, square, ...), the parasitic capacitance due to the static part of the device plays a role in the electromechanical coupling. Part of the work is to find the optimal parameters in order to obtain as high as possible coupling factor and thus high average displacement and available force of the device.

The frequency precision is mainly based on tolerances in lithography and etching. Design rules with PZT wet etching and the use of dry etching of platinum are needed to address the small dimensions of the devices (< 300 μm). In arrays, a special attention is paid to the membrane thickness uniformity, as it will influence the resonance frequencies of the device.

The aim of this chapter is to present the fundamental properties of piezoelectric micromachined ultrasonic transducers (p-MUT's) by addressing all major issues described previously. It will result in a first database of parameters (materials, design, processing) and experiences that can serve later for design optimization.

6.2 DEVICE PHYSICS AND DESIGN OF BASIC PMUT'S STRUCTURES

6.2.1 Device physics of resonant multilayer membranes

PZT/Silicon membranes are basics structures for a number of applications such as micromotors [5], micropumps [6] or microphones [7].

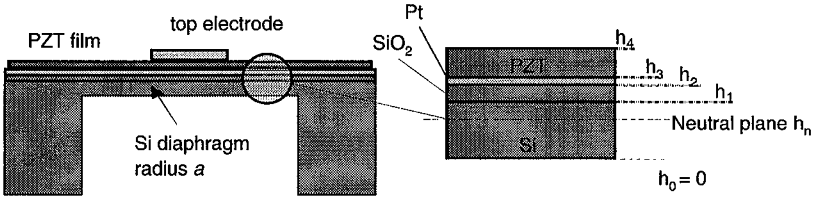

Figure 6.1: Schematic of PZT/Si membrane used for basic pMUT's structures.

A theory of actuation by piezoelectric membranes has been derived by Muralt in refs [8], [5] for the case of thin clamped disk. In what follow, only the most important aspects related to basic pMUT's structures will be recalled. For not too small silicon thickness, the membranes are well approximated by the model of a thin clamped circular disks and exact values of the resonance frequencies can be calculated [9]. The deflection of the diaphragm out of the wafer plane is described by $w(r, t) = F(r)\sin\omega t$ where r is the distance from the center of the diaphragm and ω the excitation frequency. It is also assumed that non-linear effects are neglected (small deflection compared to diaphragm thickness). If the diaphragm is rather thick and the stress can be neglected, we can assume the situation of a thin clamped disk. The elastic energy of a plate as a function of the radial deflection function w(r) can be found in the literature [10].

$$U_D = \frac{1}{2}D\int_0^a 2\pi r dr\left[\left(\frac{d^2w}{dr^2}+\frac{1}{r}\frac{dw}{dr}\right)^2 - 2\cdot(1-\nu)\cdot\frac{1}{r}\cdot\frac{dw}{dr}\cdot\frac{d^2w}{dr^2}\right] \tag{6.2}$$

$$D = \frac{Eh^3}{12(1-\nu^2)} \tag{6.3}$$

where D is the rigidity of the disc of thickness h, E is the Young's modulus and ν the Poisson coefficient. For ultrasonic transducers, only the first fundamental mode B_{00} is of interest. The solutions of equation (6.2) are known [9] and are given by the sum of two Bessel functions (see Figure 6.2). For the fundamental mode, we have:

$$F_1\left(\frac{r}{a}\right) = c_1J_0\left(\lambda_1\frac{r}{a}\right)+c_2J_0\left(i\lambda_1\frac{r}{a}\right) \tag{6.4}$$

where $\lambda_1 = 3.19$ for the fundamental mode B_{00} and c_1, c_2 are given by the following boundary conditions:

$$F(r=a)=0 \qquad F(r=0)=1 \tag{6.5}$$

$$\left.\frac{d}{dr}F(r)\right|_{r=a} = 0 \qquad \left.\frac{d}{dr}F(r)\right|_{r=0} = 0 \tag{6.6}$$

which yields $c_1 = 0.9473$ and $c_2 = 0.0528$; $c_2/c_1 = 0.0557162$

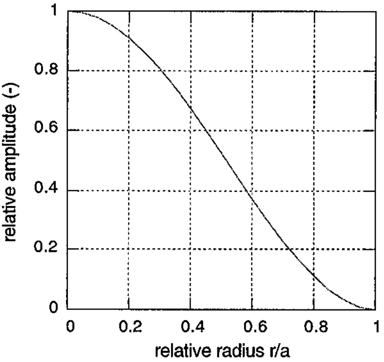

Figure 6.2: Normalized lateral deflection of a vibrating circular membrane according to equation (6.4). Membrane radius is a.

An inflection point is found at r/a = 0.5286. For piezoelectric devices, the top electrode has to be placed in order to collect charges of identical sign.

The deflection of the vibrating membrane is then given by:

$$w(r) = A \cdot f(r/a) \cdot \sin(\omega t) \tag{6.7}$$

where $f(r/a)$ is the normalized function given before as equation (6.4),

The elastic energy of a circular vibrating diaphragm as a function of the relative radius ($x = r/a$) is given by inserting equation (6.7) into equation (6.2):

$$U_D = \pi \cdot D \cdot \frac{A^2}{a^2} \cdot I_D \qquad U_D \propto h^3 \cdot \frac{A^2}{a^2} \tag{6.8}$$

where

$$I_D = \int_0^1 \left[\left(\frac{d^2 f}{dx^2} + \frac{1}{x}\frac{df}{dx} \right)^2 - 2 \cdot (1 - \nu) \cdot \frac{1}{x} \cdot \frac{df}{dx} \cdot \frac{d^2 f}{dx^2} \right] x\,dx \tag{6.9}$$

which amounts to $I_D = 9.4314$. The first resonance frequency is given by:

$$\omega_1^2 = \frac{\lambda_1^4}{a^4} \cdot \left[\frac{D}{\mu}\right] \tag{6.10}$$

where μ is the effective density per unit area of diaphragm defined by $\mu = \rho h$ and $\lambda_1 = 3.19$. In case of 4 layers composite diaphragm (PZT/Pt/SiO$_2$/Si) of individual thickness t_i, i = 1...4), D and μ are replaced by D* and μ* defined in chapter 4.

For a composite PZT/Pt/SiO$_2$/Si diaphragm, the following materials properties have been used:

Table 6.1: Materials properties of the multilayer PZT/Si diaphragm

layer	h (µm)	stress (MPa)	s_{11} (Pa $^{-12}$)	ν -	ρ (kg/m^3)	μ (kg/m^2)
PZT	2	78	12.4	0.295	7900	0.0158
Pt	0.1	550	7.35	0.42	20000	0.002
SiO$_2$	1	-300	14.2	0.3	2220	0.00222
Si	5	0	7.66	0.278	2330	0.0115

Taking a 300 µm diaphragm with a silicon thickness of 5 µm, the resonance frequency of the first mode B_{00} is found at 5 MHz. Taking into account the multilayer (D* = 3.703*10^{-6}, h_n = 3.628 µm and μ* = 0.03152), the resonance frequency is slightly shifted to 4.9 MHz.

The electromechanical coupling (piezoelectric part) has been derived by Dubois [5]. The coupling energy per unit of volume is the work done by the in-plane strains against the piezoelectric stress. It is given by:

$$U = 2\pi \cdot A \cdot M_p \cdot I_p \tag{6.11}$$

where:

$$I_p = \int_{\text{electrode}} \left(x \cdot \frac{d^2 f}{dx^2} + \frac{df}{dx}\right) dx \tag{6.12}$$

$$M_p = \sigma_p t_p \cdot \left(t_{Si} + t_{SiO_2} + t_{Pt} + \frac{t_p}{2} - h_{neutral}\right) \qquad M_p \propto t_p^2 \tag{6.13}$$

$$\sigma_p = -e_{31,f} \cdot E_3 \tag{6.14}$$

For optimal actuation, the top electrode is deposited where the curvature of the membrane is of constant sign, i.e. in [0; 0.528] or in [0.528; 1]. I_p amounts to -0.816 and 0.803 respectively.

The total mechanical energy is then given by the sum of $U_D + U_p$. At the equilibrium, the system minimize this energy, i.e. $dU_{mech}/dA = 0$. The amplitude A is then given by:

$$A = -a^2 \cdot \frac{M_p I_p}{D I_D} \tag{6.15}$$

The mechanical energy is then given by:

$$U_{mech} = -\pi a^2 \cdot \frac{(M_p I_p)^2}{D I_D} \tag{6.16}$$

The electrical energy is given by the electrostatic energy of the capacitor defined by the top electrode:

$$U_{elec} = \frac{1}{2}\pi a^2 \cdot \gamma \cdot \varepsilon\varepsilon_0 \cdot t_p \cdot E_3^2 \tag{6.17}$$

where γ is the relative electrode area (S electrode / S diaphragm).

Finally, the coupling factor k^2, which is defined as the ratio between the mechanical energy (equation (6.2)) and the piezoelectric energy is given by:

$$k^2 = \left|\frac{U_{mech}}{U_{elec}}\right| = \frac{2t_p \cdot (e_{31,f} \cdot (t_{Si} + t_{SiO_2} + t_{Pt} + t_p/2 - h_n) I_p)^2}{D^* \cdot I_D \cdot \gamma \cdot \varepsilon\varepsilon_0} \tag{6.18}$$

To better understand the influence of PZT film and silicon thickness, simulations have been carried out with the following parameters: circular membrane, radius $a = 150$ µm, $e_{31,f} = -12.5$ C/m^2, $\varepsilon = 1100$ (PZT 53/47 {100}-textured), $I_D = 9.4314$, and $\gamma = 0.279$ (top electrode in [0; r/a = 0.582], in the center of the diaphragm).

Figure 6.3 shows the simulation of the coupling factor k as a function of silicon thickness for a diaphragm coated with 1, 2, 3 and 4 µm PZT films. As the PZT film thickness increases, the maximum of the coupling factor is shifted to thicker silicon thicknesses. For comparison, the calculation without the Pt/SiO$_2$ layers is given as well. It turns out that the latter layer softens the membrane, reducing the coupling factor by about 20%. With Pt/SiO$_2$, the curve is also more flat and the optimal silicon thickness is larger. Both phenomenon's are advantageous regarding to microfabrication (more tolerance with respect to the position of the maximum and better mechanical stability of the structure).

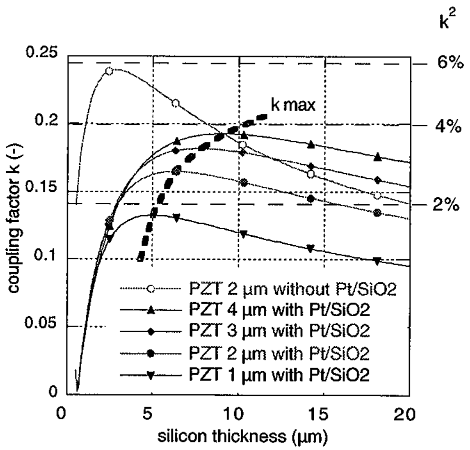

Figure 6.3: Simulation of the coupling factor k of mode B_{00} of a circular membrane (radius a = 150 µm) as a function of silicon and PZT thicknesses. For comparison, the curve for 2 µm PZT film but without taking into account the Pt/SiO_2 layers is given as well.

Figure 6.4 shows the optimal silicon thickness of the diaphragm to obtain a maximal coupling factor *k* as a function of the PZT film thickness.

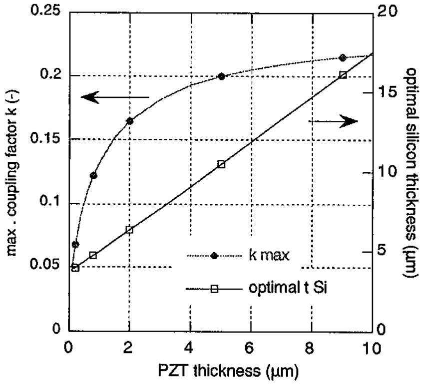

Figure 6.4: Simulation of the optimal silicon thickness to obtain a maximal coupling factor k as a function of the PZT film thickness. Pt/SiO_2 layers have been taken into account as well. Membrane radius is 150 µm.

The coupling factor saturates above a PZT thickness of 5 μm. For 2 μm PZT film, the optimal silicon thickness is 6.33 μm and $k = 0.164$. Using Equations (6.10) and (6.15), Figure 6.5 shows the amplitude of the deflection of the B_{00} mode and the resonance frequency (MHz) as a function of the diaphragm silicon thickness. PZT film thickness of 2 μm is assumed.

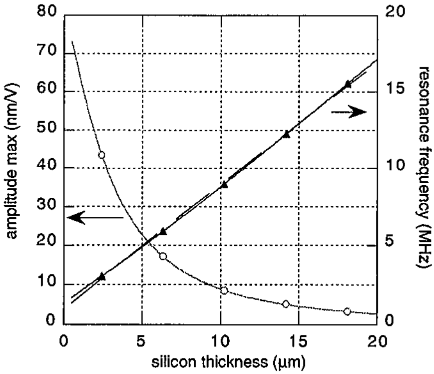

Figure 6.5: Simulation of the amplitude and B_{00} resonance frequency as a function of silicon thickness. PZT film is 2 μm thick and membrane radius is 150 μm.

The resonance frequency is increasing almost linearly with the silicon thickness except at low value where the influence of the other layers is more sensitive.

Similar calculations can be made taking into account the residual stress within the structure. But, it has been assumed that due to the stress compensation with 1 μm SiO_2, the residual stress was too small with respect to the diaphragm thickness. According to Figure 6.5, the optimal silicon thickness for 2 and 4 μm of PZT amounts to 6.5 and 9 μm respectively.

6.2.2 Design of pMUT's test vehicles

To address working frequencies in the range of 1-5 MHz and 100 kHz, 300 μm and 1 mm diameter membranes have been designed respectively. Basic shapes such as discs, squares, hexagons or octagons have been used with different top electrode geometries (covering all the surface or ring-like) and clamping conditions: fully clamped membranes (see Figure 6.6-a), membranes suspended by 4 small bridges (Figure 6.6-b) and membranes with clamping slightly reduced by 20x20 μm grooves (Figure 6.6-c).

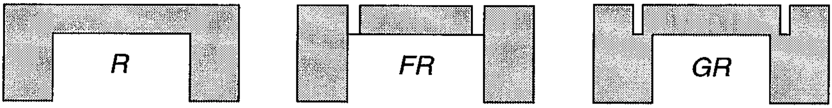

Figure 6.6: Border conditions of pMUT's basics structures; a) clamped R, b) suspended FR, c) grooved GR.

6.3 EXPERIMENTAL METHODS

6.3.1 Microfabrication

The process flow used for the fabrication of piezoelectric micromachined ultrasonic transducers (pMUT's) is very similar to the one depicted in chapter 4 for microcantilevers. Standard and silicon-on-insulator (SOI) wafers have been used. The latter was an excellent solution to obtain thin (5 μm) and uniform silicon diaphragm by stopping the deep silicon etching on the internal buried oxide (see Figure 6.7).

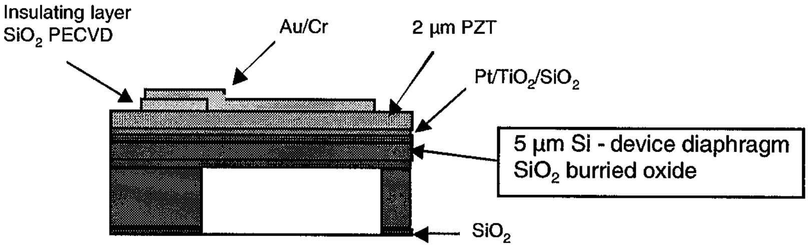

Figure 6.7: SOI substrate with SiO_2 anti-parasitic layer between PZT and top electrode on static part of pMUT's devices.

The microfabrication process runs as follow. First, Pt/TiO_2 platinum bottom electrode has been deposited by PVD. Then, 2 μm sol-gel {100}-textured PZT 53/47 thin film was grown on a {100}-textured $PbTiO_3$ seed layer. To minimize the parasitic capacitance, the top electrode on the static parts (contact pads and connecting lines) has been insulated from the PZT film by 50 nm PECVD SiO_2 thin film (see Figure 6.7). The PZT film was then wet etched in diluted HCl:HF solution and the platinum bottom electrode was patterned by ICP dry etching and served as masking layer to etch grooves and trenches through SiO_2/Si by deep reactive ion etching.

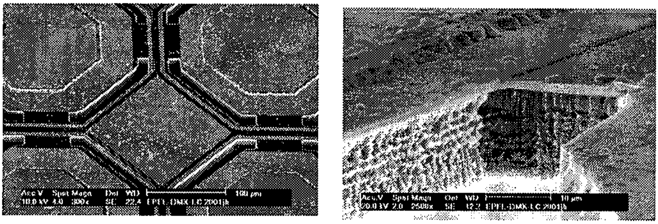

Figure 6.8: Details of 20 µm thick silicon diaphragms held by four small bridges (design suspended).

Finally, the membranes are released by deep silicon dry etching from the backside of the wafer. With standard substrate, non-uniform membranes are formed as shown by Figure 6.9 where the thermal oxide SiO_2 of the front side appears in the middle of the membrane. This limitation is due to the non-uniformity of the dry etching process (± 3%) and very few improvements are possible. With SOI wafers, 4 ± 0.5 µm thick and uniform silicon membranes have been produced. Much better uniformity in resonance frequencies can be thus achieved with devices made out of SOI substrates.

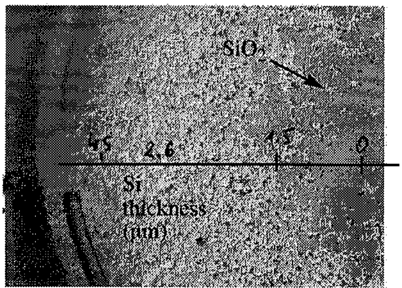

Figure 6.9: Non-uniformity in silicon thickness diaphragm on standard Si wafer.

6.3.2 Characterization of the resonance

Basic pMUT's structures have been characterized by means of optical deflection and admittance measurements. Membrane shape and vertical displacements at the resonance frequency have been measured optically by stroboscopic interferometric microscope [11] at the University of Paris-Orsay. In parallel, admittance curves have been recorded using an LCR-meter HP-4194 from Hewlett-Packard and analyzed by means of the resonator model depicted in Figure 6.10.

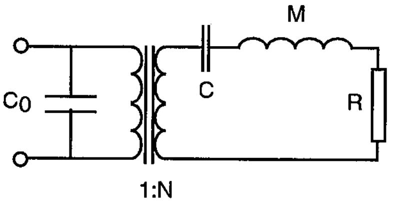

Figure 6.10: Resonator model used for the analysis of basic pMUT's.

where C, M and R represent the equivalent circuit of a piezoelectric transducers and C_0 takes into account the capacitance of the device.

The frequency dependence of the impedance Y = G+iB is given by:

$$Y = G + iB = 2\pi i f\left[C_0 + C \cdot \frac{f}{1 - \left(\frac{f}{f_0}\right)^2 + i \cdot \frac{1}{Q_m}\left(\frac{f}{f_0}\right)}\right] \tag{6.19}$$

where C_0 is the capacitance of the device. The mechanical quality factor Q_m, the resonance frequency ω_R and the coupling coefficient k^2 are obtained as:

$$Q_m = \frac{1}{\omega_R RC} \tag{6.20}$$

$$\omega_R = (MC)^{-1/2} \tag{6.21}$$

$$k^2 = \frac{C}{C + \mathrm{Re}(C_0)} \tag{6.22}$$

However, in real devices, conductor lines and contact pads outside the active membrane increase the parallel capacitor C_0 by a value C_{para}. The coupling factor is thus reduced consequently. This problem can be avoided decoupling the bottom electrode (patterning) before PZT deposition [12] or by introducing a thin SiO_2 decoupling layer between PZT and static parts of the top electrode. For the evaluation of the performance, one can subtract the parasitic part from C_0.

$$k^2 = \frac{C}{C + \mathrm{Re}(C_0) - C_{para}} \tag{6.23}$$

6.3.3 Transmission of ultrasonic wave in air and in liquid

The acoustic wave propagation between two single micromachined ultrasonic transducers in air or in liquid has been measured to evaluate the potential of p-MUTs in proximity sensors and non-destructive testing probes (see Figure 6.11). A train of 5 oscillations (10 V ac, offset = + 5 V) is generated by a function generator from Hewlett-Packard, HP33120. The signal detected by the vibration of the receiver is amplified (C_f = 10 pF) through a Kistler charge amplifier (max working frequency = 200 kHz) and measured on an oscilloscope (Tektronix TDS220).

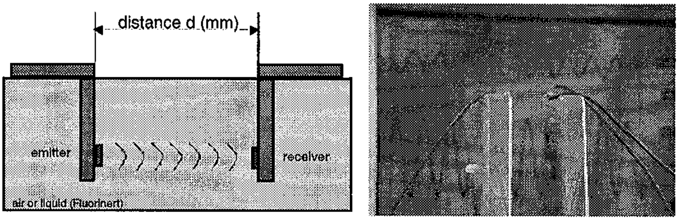

Figure 6.11: Schematic of the experimental setup used for the measurement of acoustic wave propagation in air or in liquids.

6.4 BASIC PROPERTIES OF SIMPLE P-MUT'S STRUCTURES

6.4.1 Low frequency transducers - 450 μm

Low frequency transducers (450 μm in diameter) have been characterized with respect to the shape of the top electrodes (full or ring), clamping conditions (suspended, clamped, grooved) and structure (disc, square, hexagon, octagon). Figure 6.12 shows three examples of 450 μm pitch devices with various top electrode shape and clamping conditions. Typical fundamental resonance frequency of these devices is about 100 kHz.

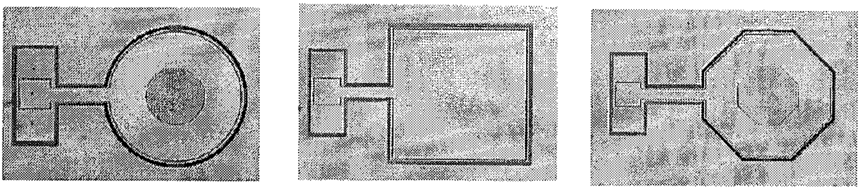

450 μm disc transducer,
suspended FR
top electrode: ring

450 μm square transducer
clamped R
top electrode: full

450 μm octagon transducer
suspended FR
top electrode: ring

Figure 6.12: 450 μm pitch (1 mm^2) transducer with various top electrode and clamping conditions

Figure 6.13 compares the conductance curves (G) of two 450 μm disc structures with full and ring top electrodes. Both devices exhibit identical silicon thickness, (7 ± 2 μm in the center) and suspended clamping conditions. The surface of the top electrode is 1 mm^2 and 0.8 mm^2 in case of full or ring top electrode respectively.

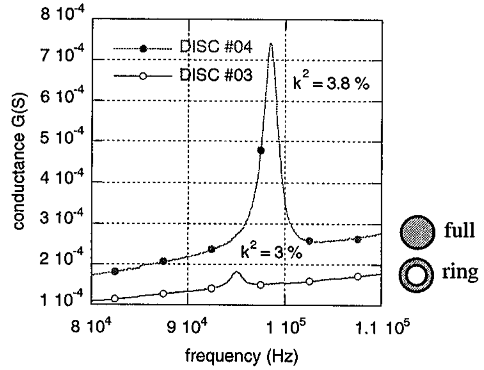

Figure 6.13: Conductance curves of circular diaphragm with disc and ring shape top electrode.

Better coupling coefficient ($k^2 = 3.8$ % vs 3 %) was achieved with top electrode covering the whole diaphragm surface (full). This can be explained by the increase of the active piezoelectric surface (+20%) and change in curvature. In the theoretical part, we assumed that, depending of the position on the membrane, the electrical charges of same sign should be detected or provided separately, i.e. that the top electrode should not cross any inflexion point in the deformation curvature. As this consideration is valid for the fundamental resonance of a simple clamped membrane, the deformation of a membrane clamped with four small bridges behaves differently as shown in Figure 6.15. In that case the curvature of the deformation and thus the piezoelectric effect tends to be maximal in the center of the device. Top electrode with ring shape is thus less favorable than an electrode covering the entire surface of the diaphragm. Similar results were obtained with other shapes (octagons, hexagons or squares).

Another interesting feature of membranes with suspended design (i.e. with the most flexible clamping conditions) is the tunability of the resonance frequency by means of dc bias. In structures with fully clamped conditions, this bias dependence of the resonance was found to be very weak. But, in suspended and thus more flexible diaphragms, a strong dependence of the resonance frequency (mode 1), from 97 to 120 kHz (+ 20%), as a function of increasing dc bias (from 0 to 150 kV/cm) has been measured (see Figure 6.14).

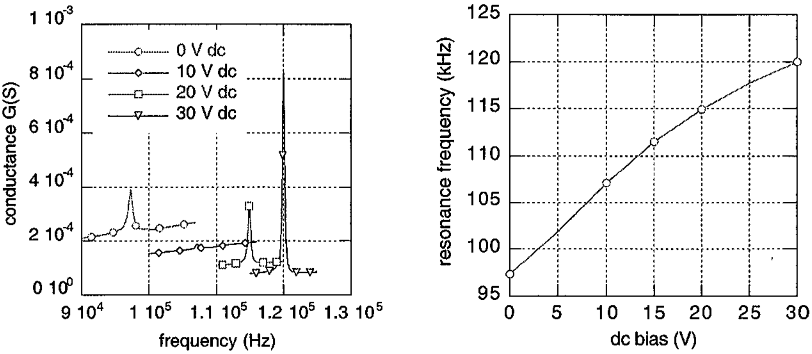

Figure 6.14: Resonance frequency (mode 1) of a disc 450 μm suspended membrane (#13) as a function of applied dc bias. At 10 V, the stress induced by the dc bias reduces the vibrating amplitude.

The large membranes (450 μm) showed also a strong dependence of the resonance frequency upon the dc-bias. The smaller membranes (disks) (300 μm) hardly showed this phenomenon. The bias indeed increases tensile stress that may translate into forces that stretch the membrane, and thus increase the frequency. The frequency shift is proportional to $(\text{diameter})^2/(\text{thickness})^3$ [8] indicating that the shift is much stronger for large membranes that are, at the same time, also thinner (effect of deep silicon etching).

Finally, 3D stroboscopic interferometric microscope has been used to measure the maximal deflection of the membrane at the resonance. Figure 6.15 shows the shape as well as the magnitude of the vertical deflection of a circular suspended diaphragm (450 μm pitch) as a function of resonance mode. At the first resonance, a maximal vertical deflection of about 650 nm/V has been measured. In ultrasonic transducers for non-destructive testing, a piston movement is necessary to achieve optimal coupling between the diaphragm and the surrounding medium (water, impedance matching gel or air). At higher mode, the complex shape of the resonance disturbs the wave generation (the diaphragm is flat on average) and most of the energy is dissipated and not transmitted.

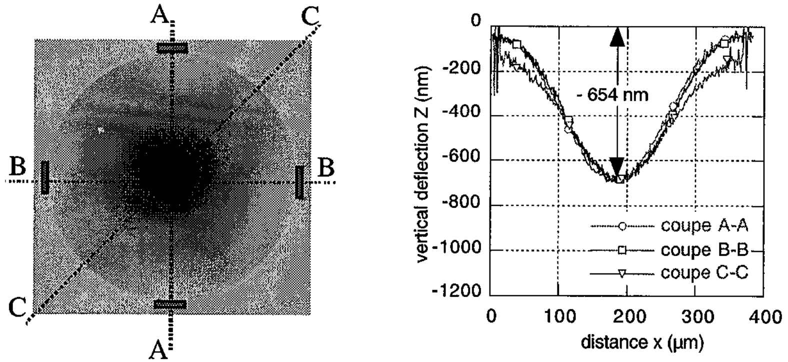

Device #13 - disc suspended, mode 1 @ 60 kHz

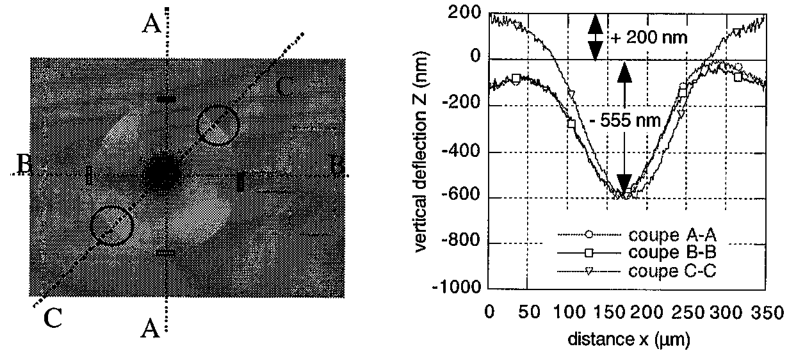

Device #13 - disc suspended, mode 2 @ 106 kHz

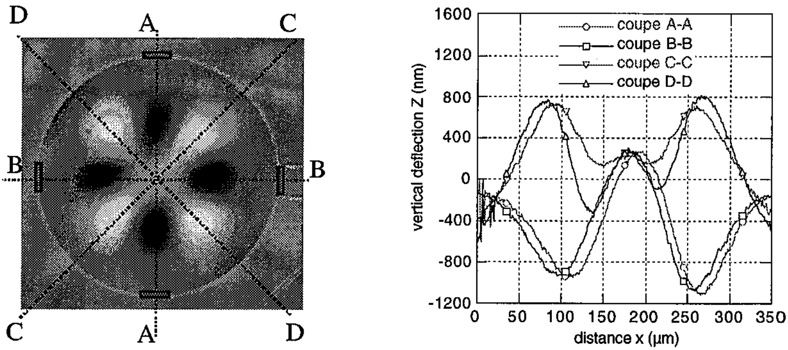

Device #13 - disc suspended, mode 3 @ 309 kHz

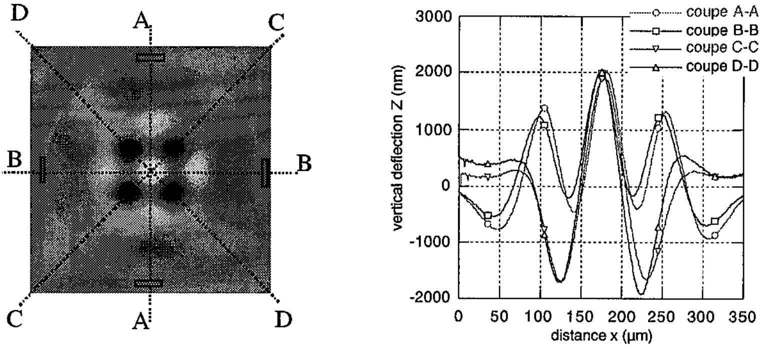

Device #13 - disc suspended, mode 4 @ 477 kHz

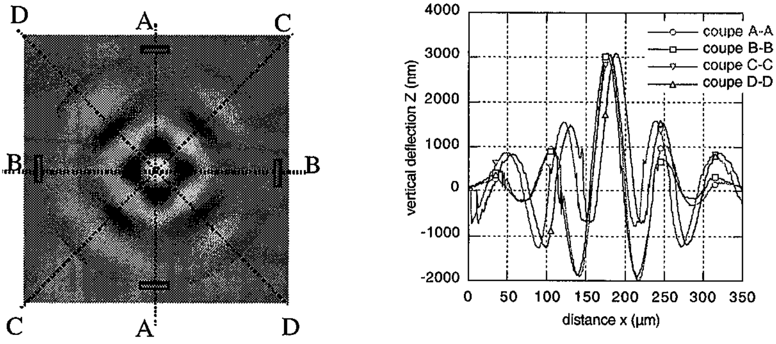

Device #13 - disc suspended - mode 5 @ 759 kHz

Figure 6.15: Mode shape and vertical deflection of resonance #1 to #5 of 450 µm pitch disc ultrasonic transducer (ref. #13).

6.4.2 High frequency transducers - 300 μm

High frequency transducers (1 - 5 MHz) are required to generate and propagate ultrasonic waves in liquids. Smaller devices (300 μm in diameter) have been produced using the same micromachining sequence. For so small devices, the surface of the active top electrode is similar to the one of the contact pads. The parasitic capacitance is thus not negligible. To avoid this problem, the passive part of the top electrode has been electrically insulated from the PZT film by means of a thin SiO_2 film deposited by PVD. Reproducible and uniform silicon thickness of the vibrating structures has been obtained using SOI substrates with 4 μm thick device silicon layer. The deep silicon etching is thus stopped on the internal buried oxide to form 4 μm thick silicon diaphragms. Figure 6.16 shows an example of 300 μm pitch ultrasonic devices made out of SOI wafer.

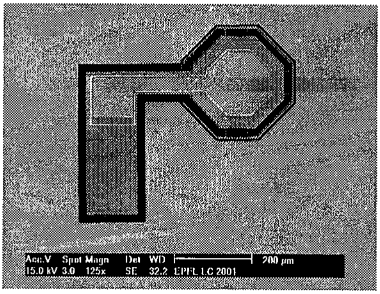

Figure 6.16: 300 μm pitch high frequency ultrasonic transducers (1 - 5 MHz). Design: suspended diaphragm held by four small bridges.

A typical result as obtained with disc, 300 μm wide, 4 μm thick silicon diaphragm, 2 μm thick PZT 53/47 film is presented in Figure 6.17. Fitting equation (6.19) and (6.23), a quality factor of 135 and a coupling factors $k = 23\%$ ($k^2 = 5.3$ %) have been calculated. Thanks to the electrical insulation of the contacting pads with 50 nm of SiO_2, the remaining parasitic capacitance was found to be negligible (0 pF).

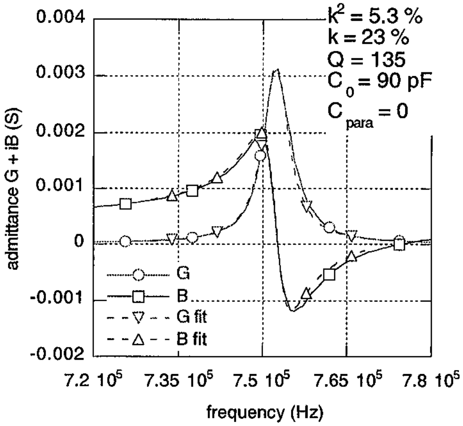

Figure 6.17: Admittance curves of 300 μm disc suspended transducer. Membrane is 4 μm thick (SOI substrate), PZT 53/47 {100} 2 μm. The measured values (full lines) are compared with the analytical model (dash lines). dc bias = 20 volts.

To improve the coupling factor, it is advantageous to superimpose a dc field. This increases the polarization of the PZT film and thus the piezoelectric coefficient, especially below the coercive field (50 kV/cm) (see Figure 6.18).

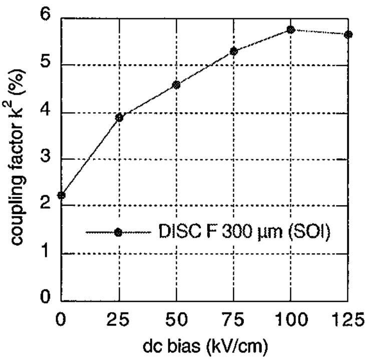

Figure 6.18: Coupling factor k^2 as a function of superimposed dc bias of the same 300 μm SOI transducers showing the improvement of the piezoelectric properties due to the increase of the polarization.

Above 75 kV/cm, coupling factors k^2 of more than 5% have been measured. The corresponding $e_{31,f}$ is larger than the directly measured value obtained at zero fields. The maximal $e_{31,f}$ is estimated to be in the range of 15 to 20 C/m^2.

6.5 ACOUSTIC WAVE PROPAGATION

One of the most interesting features of piezoelectric micromachined ultrasonic transducers (p-MUTs) is that the same device can be used either as emitter or as receiver. It is thus possible to imagine applications in proximity sensors or non-destructive testing probes. The goal here is to evaluate the performance of micromachined ultrasonic devices with respect to the transmission of an ultrasonic wave in air or in liquid.

6.5.1 Transmission in air

Two single p-MUTs devices based on free membrane (hold only by four small bridges, DISC F design) have been selected with respect to the difference between their fundamental resonance frequencies. To obtain optimal coupling, this difference should be as low as possible. The resonance frequency in air of the emitter (DISC F 3.1) and the receiver (DISC F 1.1) are 103 and 98 kHz respectively (difference ≈ 5%). Both devices have been poled at 150°C for 10 min under 150 kV/cm. The emitter is driven at the resonance frequency of the receiver (98 kHz).

Figure 6.19 shows the waveform of the emitted train of oscillations and the detected signal on the receiver as a function of the distance between the two devices.

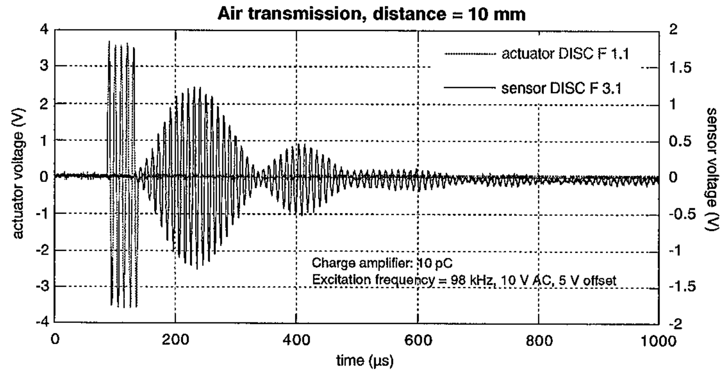

Air transmission, distance = 20 mm

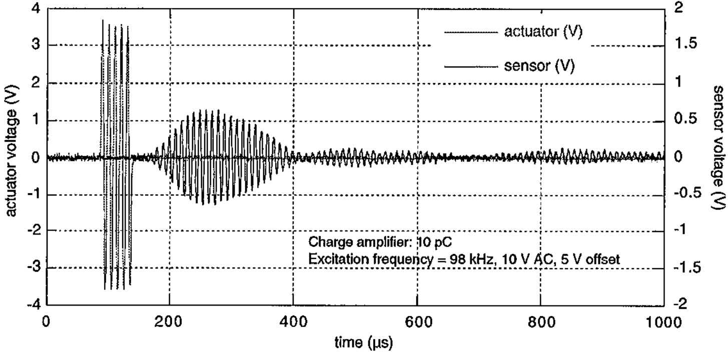

Air transmission, distance = 50 mm

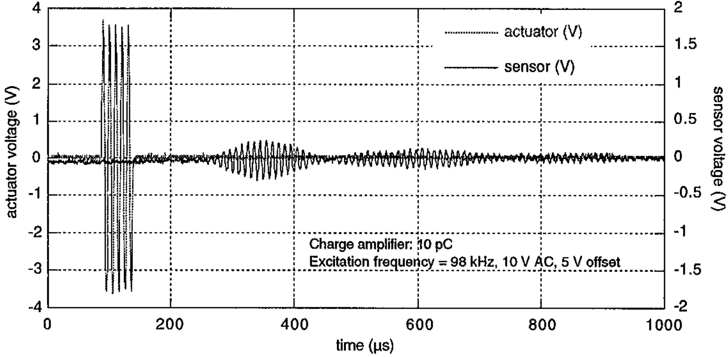

Air transmission, distance = 200 mm

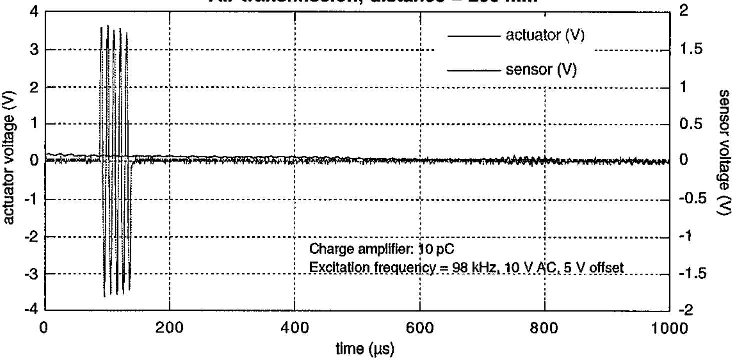

Figure 6.19: Waveform of emitted and received ultrasonic signal as a function of the distance (10, 20, 50 and 200 mm) between the devices.

With the simple detection technique used in this experiment, transmission of ultrasonic waves has been achieved up to 200 mm. Figure 6.20 gives the maximal amplitude of the signal detected on the receiver as a function of the transmission distance. A 1/d decay of the amplitude is observed.

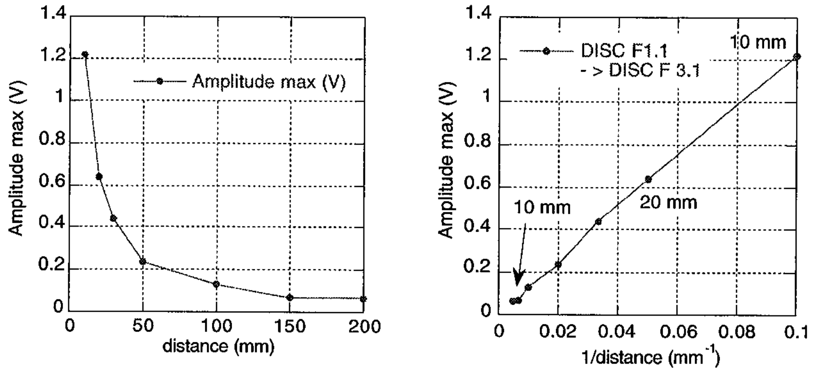

Figure 6.20: Maximal receiver amplitude as a function of transmission distance d and 1/d.

By measuring the time difference between the emission and the detection of the first oscillation on the receiver, on can retrieve the speed of sound as shown by Figure 6.21. For a low emitter-receiver distance, the difference in the air speed calculation originates from the difficulty to detect the very first oscillation on the receiver and thus on the lack of precision on the corresponding time measurement.

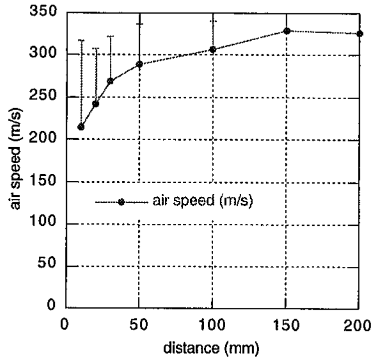

Figure 6.21: Speed of sound in air measured by the transmission time of a 5 pulse ultrasonic wave.

Usually, the second or the third oscillation is observed as they take advantage of superposition of the successive modulations (5 pulses). In general, the detected time is thus overestimated by 1 or 2 periods and the calculated air speed is lower. At 98 kHz, two periods are about 20.4 μs, which is large compared to the acoustic wave flying time through 10 mm (46 μs).

6.5.2 Ringing effect

The residual vibration of the emitter after the emission of a train of pulses is a critical factor that can reduce the timescale sensitivity of the device. In the ideal case, after the emission of a well-defined ultrasonic wave (a train of 5 pulses for instance), the emitter should stop vibrating. However, in the real world, it happens differently if the device exhibits too high quality factor Q. After the excitation, the emitter is still resonating at its resonance frequency during a certain amount of time. This effect is called ringing. To obtain clear transmission and thus clear signal detection, such effect has to be minimized (i.e. low Q devices are required). By increasing the time resolution, the ringing effect of the emitter used previously has been recorded. An acoustic wave (5 pulses) is emitted at 98 kHz. This frequency corresponds to the resonance frequency of the receiver. On Figure 6.22, it can be observed that after the emission of 5 pulses, a small ringing effect (± 0.01 V out of a ± 3 V excitation) is observed. The ringing frequency is not at 98 kHz but, obviously, at the resonance frequency of the emitter (103 kHz).

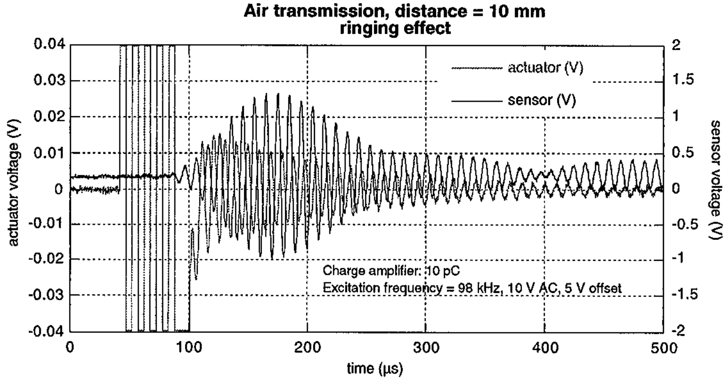

Figure 6.22: Ringing effect of the emitter after the propagation of 5 pulses.

6.5.3 Acoustic wave transmission in liquids

The characterization of ultrasonic wave emission and reception in liquids is an essential step to approach and simulate the acoustic wave propagation into the human body. It is thus possible to evaluate the potential of piezoelectric micromachined ultrasonic transducers for application in medical imaging. To avoid any electrical short-circuit in the liquid, water has been replaced by Fluorinert from 3M. Figure 6.23 shows first results of emitted and detected acoustic waveform for 10 and 25 mm transmission distance.

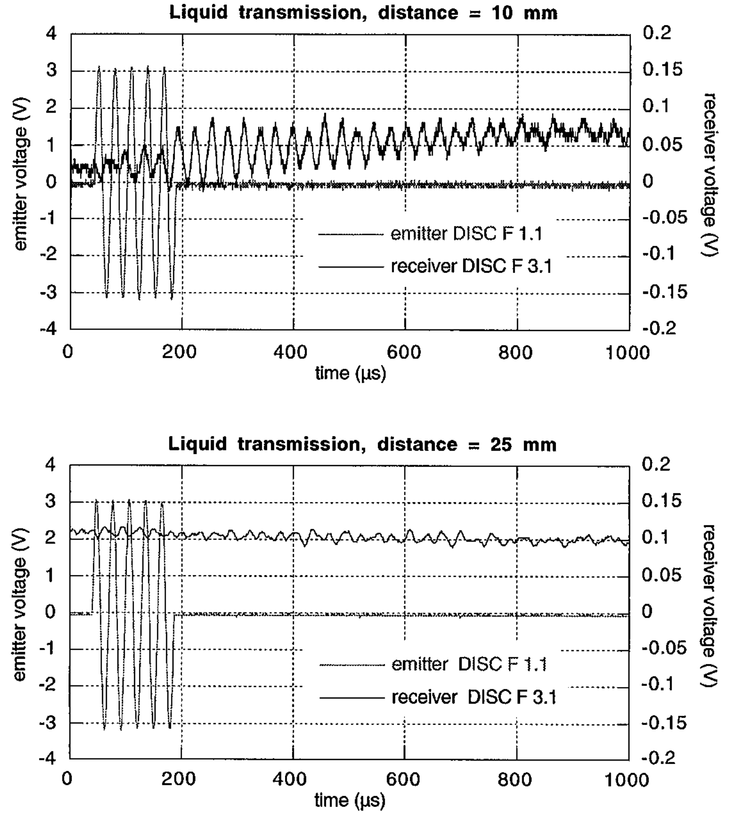

Figure 6.23: Waveform of emitted and received ultrasonic signal as a function of the distance (10 and 25 mm) in Fluorinert (3M). Damped resonance frequency of receiver is 34kHz. Excitation frequency is 34 kHz.

The damping of the vibration by the liquid changes the resonance frequency of the receiver DISC F 3 from 98 kHz down to 34 kHz. In a first approximation, the resonance frequency of the emitter is divided by a factor three and the amplitude of the signal detected by the receiver is divided by a factor ten.

6.6 SUMMARY

In this chapter, the microfabrication and the characterization of basic properties of micromachined ultrasonic transducers (pMUT's) have been presented. The integration of 2 μm thick PZT 53/47 {100}-textured on silicon-on-insulator (SOI) substrates has been realized. It turned out that SOI wafers are mandatory to achieve reproducible membranes in term of thickness and thus to obtain uniform resonance frequencies. To achieve micron resolution patterns, dry etching methods have been employed. They have been presented in detail in chapter 4.

Devices of two different sizes have been fabricated. First, 450 μm diaphragms have been used to study the influence of the clamping conditions and the shape of the top electrode. A top electrode covering the entire surface was found to be optimal with respect to the coupling coefficient. Resonance frequencies of large membranes (450 μm) with soft clamping conditions were found to be very sensitive to superposition of dc bias. This has been explained by the induced stress in the structure.

Second, 300 μm devices have been fabricated to achieve resonance frequencies in the MHz range. In that case, the influence of the dc bias on the resonance frequency was hardly seen but a strong influence on the coupling factors k^2 has been measured. Values as high as 5% have been calculated with dc bias larger than 75 kV/cm.

Finally, ultrasonic wave transmission experiment in air and in liquid between two 300 μm devices has been realized. The most important point is the uniformity in resonance frequencies between the emitter and the receiver. SOI substrates are thus mandatory to obtain as small as possible frequency dispersion. In air, the detection of ultrasonic waves up to a distance of 200 mm has been obtained using very simple detection method (charge amplifier and oscilloscope).

The feasibility of piezoelectric micromachined ultrasonic transducers has been demonstrated and fundamental properties on simple structures have shown promising results in view of the realization of proximity sensors and non-destructive testing probes. The next steps would be the realization of multi-pixel pMUT's (arrays) and the realization of a dedicated electronic interface and interconnections for the emitter and for the receiver.

6.7 REFERENCES

1. Ladabaum, I., *Silicon micromachined ultrasonic immersion transducers.* Appl. Phys. Lett., 1998. **69**: p. 3674-3676.
2. Bernstein, J.J., et al., *Micromachined high frequency ferroelectric sonar transducers.* IEEE Tran. UFFC, 1997. **44**(5): p. 960-969.
3. Perçin, G., *Micromachined two-dimensional array piezoelectrically actuated transducers.* Appl. Phys. Lett., 1998. **72**: p. 1397-1399.
4. Muralt, P., et al. *Study of PZT coated membrane structures for micromachined ultrasonic transducers.* in *IEEE Ultrasonic Symposium.* 2001. Atlanta.
5. Dubois, M.-A. and P. Muralt, *PZT Thin Film Actuated Elastic Fin Micromotor.* IEEE Transactions on Ultrasonics, Ferroelectrics, and Frequency Control., 1998. **45**(5): p. 1169-1177.
6. Luginbuhl, P., *Microfabricated Lamb wave device based on PZT sol-gel thin film for mechanical transport of solid particles and liquids.* J. Micromech. Syst., 1997. **6**(4): p. 337-346.
7. Kühnel, W. and G. Hess, *Micromachined subminiature condenser microphone in silicon.* Sensors and Actuators A, 1992. **32**: p. 560-564.
8. Muralt, P., et al., *Piezoelectric actuation of PZT thin-film diaphragms at static and resonant conditions.* Sensors and Actuators A, 1996. **53**: p. 398-404.
9. Szabo, I., *Höhere Technische Mechanik.* 1956, Berlin: Springer.
10. Timoshenko, S. and S. Woinowsky-Kriger, *Theory of plates and shells.* 1959, New-York: McGraw-Hill.
11. Petitgrand, S., *3D measurement of micromechanical devices vibration mode shapes with stroboscopic interferometric microscope.* Optics and Lasers in Eng., 2001. **36**: p. 77-101.
12. Gaucher, P., et al., *Piezoelectric bimorph cantilever for actuating and sensing applications.* J.Phys. 4, 1998. **8**: p. Pr9-235.

CHAPTER 7

CONCLUSION AND OUTLOOKS

This thesis dealt with the establishment of a reproducible and industrially exploitable fabrication technology for piezoelectric MEMS based on PZT thin films. Basic properties of cantilever and membrane structures have been evaluated for dc, acoustic and ultrasonic applications. Two applications have been successfully demonstrated. First, a cantilever microphone was tested as acoustic sensor in a photoacoustic gas detector, achieving a detection threshold of 200 ppm. Second, piezoelectric micromachined ultrasonic transducers (pMUT's, 0.8 mm^2 partially clamped membrane structures) were used for ultrasonic emission-receive experiments over a distance of 20 cm in air and 2 cm in liquid.

The piezoelectric material investigated in this work was $Pb(Zr,Ti)O_3$ in the form of textured, 1 to 4 μm thick films grown by sol-gel technique. The films were deposited on (111)-textured Pt bottom electrodes applying sputter deposited seed layers of {100}-textured $PbTiO_3$ or titania for {100} and {111} texture respectively. It was shown that {100}-textured films of morphotropic phase boundary composition are the most suited ones for MEMS applications where a strong transverse $e_{31,f}$ coefficient is required. Dense films of such composition and texture could be grown up to a thickness of 4 μm without any cracks. Complete device wafers have been processed with 2 μm thick films. The residual mechanical stress was reproducibly obtained within the range of 30 to 160 MPa (depending on thickness and poling), which allowed for a precise account of the stress in the design of the device. The transverse piezoelectric coefficient $e_{31,f}$ stayed at 11.5 to 12.5 C/m^2 throughout the investigated thickness range, whereas the longitudinal $d_{33,f}$ coefficient increased from 80 to 130 pm/V with increasing thickness. These values are excellent when compared to previously published thin films values and also to pure PZT ceramics. However, the $e_{31,f}$ is a factor 2 lower as compared to optimized, modern bulk PZT ceramics. These are doped with a number of ions such as La^{3+}, Nb^{5+}, etc... One can thus expect that doping will yield an enhancement of the properties, including the remanence, also in the case of thin films. In the present films, applying a dc-bias enhanced the piezoelectric properties. Coupling factor k up to 40% were obtained in this way with ultrasound resonators. The reduction of backswitching could also reduce the dielectric losses that are directly related to poling-depoling phenomena. It is not clear whether the dielectric loss is sufficiently small for operating transducers at very high ac fields of 100 kV/cm peak-to-peak amplitudes. Further experiments are required to understand the difference in thickness dependence observed in transverse and longitudinal piezoelectric coefficients. In addition, the influence of the observed concentration gradients in the film on piezoelectric properties are not assessed. As a conclusion one can say that a very good PZT film quality was achieved - as judged with respect to the current state-of-the-art - that, however, still some way has to be done to achieve a performance similar to the best ceramics used today.

PZT MEMS requires some special microfabrication processes. These are notably the micron scale patterning of noble metal electrodes and of the PZT film itself. For Pt, satisfying results have been obtained by dry etching in an ICP reactor with an Ar/Cl_2 gas mixture, allowing for the use of standard photoresist masks. Dry and wet etching was applied for PZT. Excellent results were achieved with dry etching in an ECR/RF low-pressure reactor. However, above 1 μm thickness this process became unpractical due to insufficient selectivity with respect to photoresist. The wet etching used for thicker films is compatible with the other fabrication steps, however, the lateral resolution is limited (design rule: 5 x thickness). So there is still a need to develop a hard mask approach with dry etching. The chosen process flow was such that all layers up the top electrode were first deposited, and then sequentially patterned. In this way the PZT interfaces were always protected and the functional properties completely maintained. The process flow related to PZT was successfully combined with deep silicon etching techniques to produce free standing structures. The platinum bottom electrode proved to be a valuable hard mask for deep silicon etching. Uniform thickness of the silicon structures was only achieved with SOI substrates. A further improvement would be a better definition of the corners between vertical walls and the membranes defined by the buried oxide.

The applicability of the processes and the usefulness of the piezoelectric properties of the PZT films have been verified and demonstrated by means of two piezoelectric micro-electro-mechanical devices. First, an acoustic sensor for low frequency applications (< 50 Hz) in the form of a cantilever has been developed for integration in photoacoustic gas detectors. The main problems solved here were the stress compensation in the structure and the accurate dry etching methods applied to achieve micrometer wide slits around the cantilevers. A high device sensitivity of up to 150 mV/Pa has been obtained. The noise level corresponded to a few mPa but was mainly due to the preamplifier and not to the intrinsic noise of the sensor. The latter would be as low as 0.1 mPa. Even the actual state is sufficient for competing with current CO_2 sensors. Further improvements would require the use of silicon-on-insulator substrates to obtain better uniformity in silicon structure thickness and the design of a preamplifier that better matches the capacitance of the device with its own input impedance.

The second device was based on a silicon/PZT diaphragm with various clamping conditions. The aim was to produce a vibrating structure in view of fabricating ultrasonic transducers for position sensors and non-destructive testing probes. Here, thicker (100}-textured PZT films were successfully integrated on thin and uniform silicon diaphragm (using silicon-on-insulator, SOI technology). The study of the basic properties of such structures has shown excellent results as coupling factors k^2 up to 5% for PZT 2 μm / Si 4 μm SOI membranes held with four small bridges. Ultrasonic wave transmission between two devices has been achieved up to a distance of 200 mm that demonstrates interesting opportunities in position sensors. In this domain, further improvement would require multiple pixel devices (linear and 2D array) to address the field of probes for medical imaging.

APPENDIX A

FIGURES OF MERITS AND PROPERTIES OF PIEZOELECTRIC MATERIALS

For **sensors** applications, there are three important figures of merit (FOM) depending upon the detection criteria [1].

Charge detection: $\mathrm{FOM} = e_{31,f}$ $(\mathrm{C/m^2})$ (A.1)

Voltage detection: $\mathrm{FOM} = e_{31,f}/\varepsilon_0\varepsilon_{33,f}$ $(\mathrm{GV/m})$ (A.2)

AC Signal to Noise: $S/N = \dfrac{|e_{31,f}|}{\sqrt{\varepsilon_0\varepsilon_{33,f}\cdot\tan\delta}}$ $10^5\ \mathrm{Pa}^{0.5}$ (A.3)

In **actuators** or **transducers**, the figure of merit is given for three criteria: force, coupling coefficient (material part only) or power efficiency.

Force: $\mathrm{FOM} = e_{31,f}$ (A.4)

Coupling factor: $(k_{p,f})^2 = \dfrac{2(e_{31,f})^2}{\varepsilon_0\varepsilon_{33,f}}\cdot\left(\dfrac{1-\nu}{Y}\right)_{Si}$ (A.5)

Power efficiency: $\mathrm{FOM} = \dfrac{(k_{p,f})^2}{\tan\delta} = \dfrac{2(e_{31,f})^2}{\varepsilon_0\varepsilon_{33,f}}\cdot\left(\dfrac{1-\nu}{Y}\right)_{Si}\cdot\dfrac{1}{\tan\delta}$ (A.6)

The coupling coefficient $(k_{p,f})^2$ is given here for a thin clamped disk [1]. Y and ν are the silicon Young modulus (130 GPa) and Poisson coefficient (0.278) respectively.

Elastic, piezoelectric and dielectric constants and Figure of Merit of PZT, AlN and ZnO in the form of thin films, single crystals or bulk ceramics are listed in Table 1.

Table A.1: *Summary of properties of piezoelectric thin films, single crystals and bulk ceramics*

Properties	(111) PZT 45/55film, 1 µm [2]	AlN film [2]	ZnO film [3]	bulk PZT Motorola 3203HD [4]	bulk undoped PZT 52/48 [5]	AlN epitaxial film [6]	s.c. ZnO [7]
ρ [kgm^{-3}]				7850	7390	3260	5680
Elastic compliance							
s^E_{11} [10^{-12} m^2/N]				15.6	13.8	3.53	7.858
s^E_{33} [10^{-12} m^2/N]				18.9	17.1	2.99	6.94
s^E_{12} [10^{-12} m^2/N]				-4.2	-4.07	-1.02	-3.432
s^E_{13} [10^{-12} m^2/N]				-8.2	-5.80	-0.76	-2.206
s^E_{44} [10^{-12} m^2/N]					48.2	8.47	23.57
Elastic stiffness							
c^E_{11} [GPa]					114	345	209.7
c^E_{33} [GPa]				141	98.2	395	210.9
c^E_{12} [GPa]					58.3	125	121.1
c^E_{13} [GPa]				101	58.5	120	105.1
c^E_{44} [GPa]					20.7	118	42.47
Piezoelectric							
e_{31} [C/m^2]				-12.2	-3.08	-0.58	-0.573
e_{33} [C/m^2]				19.3	10.95	1.55	1.32
e_{15} [C/m^2]					10.25	-0.48	-0.48
d_{31} [pm/V]				-295	-93.5	-2	-5.43
d_{33} [pm/V]				564	223	5	11.67
d_{15} [pm/V]				560	494	-4.07	-11.34
$d_{33,f}$ [pm/V]	**50**	**3.4**	**10-12**	**139.6***	**111.5***	**3.40***	**6.26***
$e_{31,f}$ [C/m^2]	**-8.28**	**-1.02**	**-0.8**	**-25.9***	**-9.6***	**-1.05***	**-1.23***
Permittivity @ 1 kHz							
ε^T_{11} [-]				2417	1180		9.16
ε^T_{33} [-]				3332	730		12.64
ε^S_{11} [-]					612	8.0	8.55
ε^S_{33} [-]				1197	399	9.5	10.2

Table A.1: *Summary of properties of piezoelectric thin films, single crystals and bulk ceramics*

Properties	(111) PZT 45/55film, 1 μm [2]	AlN film [2]	ZnO film [3]	bulk PZT Motorola 3203HD [4]	bulk undoped PZT 52/48 [5]	AlN epitaxial film [6]	s.c. ZnO [7]
$e_{33,f}$ [-]	**1100**	**10.5**	**10.9**	**1606***	**527***	**9.14***	**11.1***
tan δ	0.03	0.002	0.01 - 0.1	0.028	0.0027	N/A	**
Figures of merits							
Force and curent resp. (C/m^2)	**-8.28**	**-1.02**	**-0.83**	**-25.9**	**-9.6**	**-1.05**	**-1.23**
Voltage resp. (GV/m)	**-0.85**	**-10.9**	**-8.3**	**-1.82**	**-2.06**	**-12.96**	**-12.5**
Signal to Noise 10^5 Pa$^{0.5}$	**4.8**	**23.7**	**2.5 - 8**	**3.86**	**8.04**		
Coupling coeff.	**0.08**	**0.12**	**0.023**	**0.52**	**0.22**	**0.15**	**0.17**
Power efficiency	**2.61**	**62**	**0.23 - 2.3**	**18.7**	**81.25**		

,f Effective properties of thin films

* "Equivalent" effective value calculated with equations 1.5, 1.6 and 1.7.

REFERENCES:

1. Muralt, P., *Piezoelectric thin films for MEMS.* Integrated Ferroelectrics, 1997. **17**: p. 297-307.
2. Dubois, M.-A., *Aluminium nitride and lead zirconate-titanate thin film for ultrasonic applications: integration, properties and devices.*, in *Thesis n°2086.* 1999, Ecole Polytechnique Fédérale de Lausanne: Lausanne.
3. Gardeniers, J.G.E., Z.M. Ritmersma, and G.J. Burger, *Preferred orientation and piezoelectricity in sputtered ZnO films.* J. Appl. Phys., 1998. **83**: p. 7844-7854.
4. Sherrit, S., H.D. Wiederick, and B.K. Mukherjee, *A complete characterization of the piezoelectric, dielectric and elastic properties of Motorola PZT 3203 HD including losses and dispersion.* Proc. SPIE, 1997. **3037**: p. 158-169.
5. Berlincourt, D.A., C. Cmolik, and H. Jaffe. *Piezoelectric properties of polycrystalline lead titanate zirconate compositions.* in *Proceedings of IRE48.* 1960. New-York.
6. Tsubouchi, K. and N. Mikoshiba, *Zero-Temperature-Coefficient SAW Devices on AlN Epitaxial Films.* IEEE Tran. UFFC, 1985. **SU-32**(5): p. 634-644.
7. Auld, B.A., *Acoustic Field and Waves in Solids.* Vol. 1. 1973, New-York: Wiley Interscience.

PUBLICATIONS AND PATENT

1. Muralt, P., M.-A. Dubois, A. Seifert, D.V. Taylor, N. Ledermann, and S. Hiboux, *In-plane Piezoelectric coefficient of PZT Thin Films as a Function of Composition.* Ferroelectrics, 1999. 224: p. 235-242.
2. Ledermann, N., P. Muralt, and A. Dommann. *Accurate Microscopic method to investigate the aging of PZT/Silicon heteromorphs cantilevers.* in 2nd International Conference on Integrated Micro/Nanotechnology for Space Applicaions - MNT'99. 1999. Pasadena (USA).
3. Ledermann, N., J. Baborowski, P. Muralt, N. Xantopoulos, and J.-M. Tellenbach, *Sputtered silicon carbide thin films as protective coating for MEMS applications.* Surface and Coatings Technology, 2000. 125: p. 246-250.
4. Baborowski, J., P. Muralt, N. Ledermann, and S. Hiboux, *Etching of* RuO_2 *and Pt thin films with ECR/RF reactor.* Vacuum, 2000. 56: p. 51-56.
5. Baborowski, J., P. Muralt, and N. Ledermann, *Etching of platinum thin films with dual frequency ECR/RF reactor.* Integrated Ferroelectrics, 1999. 27: p. 243-256.
6. Seifert, A., N. Ledermann, S. Hiboux, and P. Muralt, *Study of the transverse piezoelectric coefficient of PZT thin films as a function of the texture and composition.* Mater. Res. Soc. Proc., 2000. 596: p. 535-540.
7. Baborowski, J., P. Muralt, N. Ledermann, E. Colla, A. Seifert, S. Gentil, and N. Setter, *Mechanisms of* $Pb(Zr_{0.53}Ti_{0.47})O_3$ *Thin Film Etching with ECR/RF Reactor.* Integrated Ferroelectrics, 2000. 31: p. 261-271.
8. Ledermann, N., J. Baborowski, A. Seifert, B. Willing, S. Hiboux, P. Muralt, and N. Setter, *Piezoelectric cantilever microphone for photoacoustic gas detector.* Integrated Ferroelectrics, 2001. 35(1-4): p. 177-184.

9. Seifert, A., N. Ledermann, S. Hiboux, J. Baborowski, P. Muralt, and N. Setter, *Processing Optimization of Solution Derived* $PbZr_{1-x}Ti_xO_3$ *thin films for piezoelectric applications.* Integrated Ferroelectrics, 2001. 35(1-4): p. 159-166.

10. Baborowski, J., N. Ledermann, S. Gentil, and P. Muralt. *Micromachining of Piezoelectric MEMS.* in Transducers 2001. 2001. Munich.

11. Polien, A., N. Ledermann, J. Baborowski, and P. Muralt. *New material for thin film filament of micromachined hot-plate.* in Transducers'01. 2001. Munich.

12. Ledermann, N., J. Baborowski, S. Gentil, and P. Muralt. *PZT thin film acoustic sensor with partially unclamped membranes.* in IMEMS'01. 2001. Singapore.

13. Muralt, P., N. Ledermann, J. Baborowski, and A. Polien. *New materials for thin film filament microheater.* in IMEMS'01. 2001. Singapore.

14. Baborowski, J., N. Ledermann, and P. Muralt. *Micromachining of piezoelectric MEMS.* in IMEMS'01. 2001. Singapore.

15. Muralt, P., D. Schmitt, N. Ledermann, J. Baborowski, P.K. Weber, W. Steichen, S. Petigrand, A. Bosseboeuf, and N. Setter. *Study of PZT coated membrane structures for micromachined ultrasonic transducers.* in IEEE Ultrasonic Symposium. 2001. Atlanta.

16. Muralt, P., N. Ledermann, J. Baborowski, and S. Gentil, *Integration of Piezoelectric* $Pb(Zr_xTi_{1-x})O_3$ *(PZT) thin films into micromachined sensors and acuators*, in Materials and Process Integration for MEMS, P.F.E.H. Tay, Editor. 2002, Kluwer Academic Publishers, The Netherlands.

17. Muralt, P., N. Ledermann, and J. Baborowski, *Piezoelectric micro-electro-mechanical systems with PZT thin films: Integration and application issues*, in Piezoelectric Materials for the End-User, N. Setter, Editor. 2002: Lausanne.

18. Ledermann, N., P. Muralt, J. Baborowski, S. Gentil, M. Cantoni, K. Mukati, A. Seifert, and N. Setter, *{100}-textured PZT thin film for MEMS: deposition, integration and properties.* Sensors and Actuators A, 2003. accepted.

Patent:

19. Pollien, A., N. Ledermann, J. Baborowski and P. Muralt, High temperature micro-hotplate, patent WO 02/080620 A1

CURRICULUM VITAE

Nicolas G. Ledermann
Born April 23rd 1972
Swiss citizen
EPFL Engineer in Material Science and Technology

2002 -	Research Engineer at Orbisphere Laboratories, Geneva.
1997-2002	Research assistant at the Ceramics Laboratory, Swiss Federal Institute of Technology, Lausanne (EPFL). PhD thesis on Piezoelectric acoustic sensors and ultrasonic transducers based on textured PZT thin films.
1992-1997	Studies in material science at the Swiss Federal Institute of Technology in Lausanne (EPFL). Diploma thesis on the sputter deposition of oxides electrodes for ferroelectric memories.
1987-1992	Studies in chemical engineering at the University of Applied Science, Geneva (EIG/HES), Diploma thesis on the recycling of mercury in water.